

Computational studies of passive vortex generators for flow control

by

Florian von Stillfried

December 2009
Technical Reports from
Royal Institute of Technology Stockholm
Linné Flow Centre
Department of Mechanics
SE - 100 44 Stockholm, Sweden

Typsatt i $\mathcal{A}\mathcal{M}\mathcal{S}$ - $\mathcal{L}\mathcal{A}\mathcal{T}\mathcal{E}\mathcal{X}$

Akademisk avhandling som med tillstånd av Kungliga Tekniska högskolan i Stockholm framlägges till offentlig granskning för avläggande av teknologie licentiatexamen onsdagen den 16 december 2009 kl 10.15 i E3, Huvudbyggnaden, Kungliga Tekniska högskolan, Osquars Backe 14, Stockholm.

©Florian von Stillfried 2009

Universitetsservice US-AB, Stockholm 2009

Computational studies of passive vortex generators for flow control

Florian von Stillfried

Linné Flow Centre, Dept. of Mechanics, Royal Institute of Technology
SE-100 44 Stockholm, Sweden

Abstract

Many flow cases in fluid dynamics face undesirable flow separation due to rising static pressure on wall boundaries. This occurs e.g. due to geometry as in a highly curved turbine inlet duct or e.g. on flow control surfaces such as wing trailing edge flaps within a certain angle of attack range. Here, flow control devices are often used in order to enhance the flow and delay or even totally eliminate flow separation. Flow control can e.g. be achieved by using passive or active vortex generators (VG) that enable momentum mixing in such flows. This thesis focusses on passive VGs, represented by VG vanes that are mounted upright on the surface in wall-bounded flows. They typically have an angle of incidence to the mean flow and, by that, generate vortex structures that in turn allow for the desired momentum mixing in order to prevent flow separation. A statistical VG model approach, developed by KTH Stockholm and FOI, the Swedish Defence Research Agency, has been evaluated computationally. Such a statistical VG model approach removes the need to build fully resolved three-dimensional geometries of VGs in a computational fluid dynamics mesh. Usually, the generation of these fully resolved geometries is rather costly in terms of preprocessing and computations. By applying this VG model, the costs reduce to computations without VG effects included. Nevertheless, the VG model needs to be set up in order to define the modelled VG geometry in an easy and fast preprocessing step. The presented model has shown sensitivity for parameter variations such as the modelled VG geometry and the VG model location in wall-bounded zero pressure gradient and adverse pressure gradient flows on a flat plate, in a diffuser, and on an airfoil with its high-lift system extracted. It could be proven that the VG model qualitatively describes correct trends and tendencies for these different applications.

Descriptors: passive flow control, vortex generator, statistical modelling, turbulence, separation prevention, flat plate, diffuser, high-lift design, airfoil

Preface

This work investigates the application, evaluation, and calibration of a statistical vortex generator model, originally proposed by Törnblom & Johansson (2007). In the first part, the theory, the basic concepts, the methods for the statistical modelling of passive vortex generators, and a short discussion of chosen results are presented. The second part of this thesis contains two papers:

Paper 1. VON STILLFRIED F., WALLIN S. AND JOHANSSON A. V., 2009
“A Vortex Generator Model Applied in Zero and Adverse Pressure Gradient Flow”, Submitted to AIAA Journal.

Paper 2. VON STILLFRIED F., WALLIN S. AND JOHANSSON A. V., 2009
“Evaluation of a Vortex Generator Model in Adverse Pressure Gradient Boundary Layers”, Submitted to AIAA Journal.

Division of work between authors

The research project was originally initiated by Ardeshir Hanifi, Stefan Wallin (SW) and Arne Johansson (AJ). SW and AJ acted as supervisors. Moreover, SW, AJ and Florian von Stillfried (FS) have continuously discussed the progress of the project.

Paper 1

The computations of the ZPG flat plate and the HELIX airfoil cases were carried out by FS with feedback from SW. SW provided results for the diffuser study. The paper was written by FS with inputs from SW and AJ.

Paper 2

The computations of the APG flat plate case were carried out by FS with input from SW. The paper was written by FS with input from SW and AJ.

Happiness is nothing more than good health and a bad memory.

Albert Schweitzer (1875 – 1965)

Contents

Abstract	iii
Preface	iv
Part I. Overview and summary	
Chapter 1. Introduction	1
Chapter 2. Theoretical background	6
2.1. Governing equations	6
2.2. A short introduction to turbulence modelling	7
Chapter 3. Statistical modelling of passive vortex generators	12
3.1. Passive vortex generators for flow control	12
3.2. Analytical methods	12
3.3. Numerical methods	15
Chapter 4. Results and discussion	22
4.1. Flat plate in zero pressure gradient flow	22
4.2. Flat plate in adverse pressure gradient flow	28
4.3. Internal diffuser flow	31
Chapter 5. Summary of Papers	33
5.1. Paper 1	33
5.2. Paper 2	33
Concluding remarks and outlook	35
Acknowledgements	38
References	39

Part II. Papers

Paper 1. A Vortex Generator Model Applied in Zero and Adverse Pressure Gradient Flow	45
Paper 2. Evaluation of a Vortex Generator Model in Adverse Pressure Gradient Boundary Layers	85

Part I

Overview and summary

CHAPTER 1

Introduction

The demand to design more cost effective high-lift configurations for future aircrafts that in turn comes along with better low-speed behaviour during take-off and landing, increased safety, and less environmental impact is becoming more and more important for the aircraft industry and its manufacturers. At the same time, reduction of the complexity of existing high-lift systems is not only a trend but a need in order to e.g. advance flight safety, reduce overall weight, lower fuel emissions, increase the operating distance, just to mention a few. In total, it can be stated that the high-lift system has a meaningful impact on the total performance of the aircraft, economically as well as ecologically.

But not only aircraft industry faces such challenges, all other industries that are dealing with fluid dynamical processes are constantly in the need to improve their products in order to either be and remain competitive on the market and/or to fulfil legal issues like certification processes due to changing laws and being present on different markets throughout the world.

Flow control is a very effective way for improving existing fluid dynamical systems and can be a powerful tool in the conceptual design process step from the very beginning of the development cycle. The term "flow control" in fluid dynamics is generally used when a flow of some liquid or gas is changed by so-called flow control devices (such as vortex generators, VGs) in a beneficial way that the overall efficiency of the system is increased. In borderline cases, it might even occur that a fluid dynamical system would not work properly without such flow control devices applied.

Where flow control is needed, equipping surfaces with passive vane VGs is a common procedure, see also the examples of aircraft wings in figures 1.1 and 1.2. Such passive VGs mix the fluid near surfaces and force higher momentum fluid from the free stream towards the wall and vice versa. This increases the near-wall velocity as well as the momentum and consequently the stability of the flow in terms of separation delay and prevention. During the development phase when an increasing amount of computational simulations is used nowadays, VGs generally create the disadvantage of rather being computationally costly and time-consuming when included in a detailed analysis. Computational grids often fully resolve such flow control devices, leading to an enormous amount of additional nodes in their vicinity. In turn, this causes high computational costs. Therefore, flow control devices are often neglected in computations. But later during an experimental evaluation these devices are then often included

in e.g. wind or water tunnel investigations where the impact can be studied more easily. This is of course a disadvantage for the product design process that would generally benefit from a more detailed performance investigation even from the beginning of the development cycle.



FIGURE 1.1. *Extracted flaps and spoilers uncover vortex generators on the B767-300ER flap during touch-down.*

Different techniques to include VGs in computations are used: fully resolved, partly resolved/modelled, and fully modelled approaches exist. Fully resolved VGs are completely embedded in the three-dimensional (3D) computational mesh, leading to very fine mesh sizes in their vicinity. Partly resolved/modelled approaches model the VGs by e.g. volume forces that are in turn added to the governing equations. Still, the generated structures need to be resolved and a higher mesh density is needed downstream of the VGs. Fully modelled approaches, like the one described in this thesis, also model the generated structures or the influence of the modelled VGs. This approach further reduces the mesh size compared to the partly resolved/modelled approach.

For a long time, passive VGs have been used in order to control flows. Pearcey (1961) suggested certain design criteria for successful boundary layer flow control. His studies contained many different unsuccessful and successful designs as e.g. co-rotating and counter-rotating VGs, multiple row systems, and vane-type VGs of different geometries, see also figure 1.3. In particular,



FIGURE 1.2. *Vortex generators on the main wing of a B737-800 during cruise flight.*

he found out that it was practical to set the VG height to wing chord ratio to $h_{VG}/c = 0.01$ when using counter-rotating set-ups on wings. In addition, other parameters like the distance between VG pairs, the length of the VG chord, the VG angle of incidence, and the distance between two VG blades were investigated.

Experimental studies of vortex pairs within a turbulent boundary layer, see e.g. Pauley & Eaton (1988), have shown that certain VG settings have advantages compared to others. A conclusion by this work is that counter-rotating VG pairs should be arranged in such a way that they produce "common flow down" vortex structures between neighbouring VG blades, i.e. having diverging blade angles in the streamwise direction, see figure 1.4 a). Counter-rotating systems generating "common flow up" vortex structures as shown in figure 1.4 b) have less effect on flow separation control since the vortices tend to travel away from the wall and strongly interact with each other. Furthermore, co-rotating VG arrangements, see figure 1.4 c), should provide certain minimum distances between neighbouring VG blades because the vortex velocities tend to cancel out each other if VGs are placed too closely. A possible arrangement of multiple-row VGs is given in 1.4 d), though it was not investigated by Pauley & Eaton (1988).

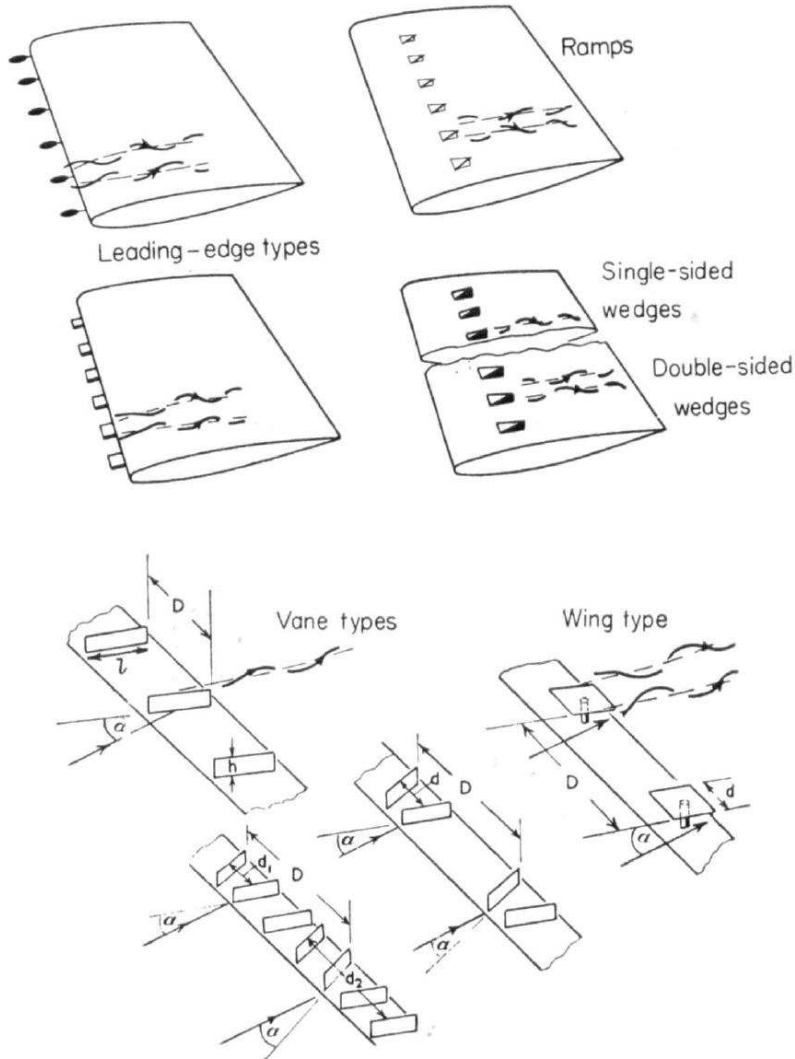


FIGURE 1.3. *Types and notation of Pearcey's vortex generators, taken from Pearcey (1961).*

More recent studies (Lin 2002; Yao *et al.* 2002) have shown that so-called sub-boundary layer VGs (SBVGs) have major advantages compared to the bigger standard vane VGs that have heights in the order of the local boundary layer thickness δ_{99} , i.e. $h_{VG}/\delta_{99} \approx 1$. SBVGs have a typical device height of $0.1 \leq h_{VG}/\delta_{99} \leq 0.5$, thus mixing the flow and its momentum only within the boundary layer. This has shown to be very efficient, even compared to conventional VGs. However, the additional benefit of using passive flow control

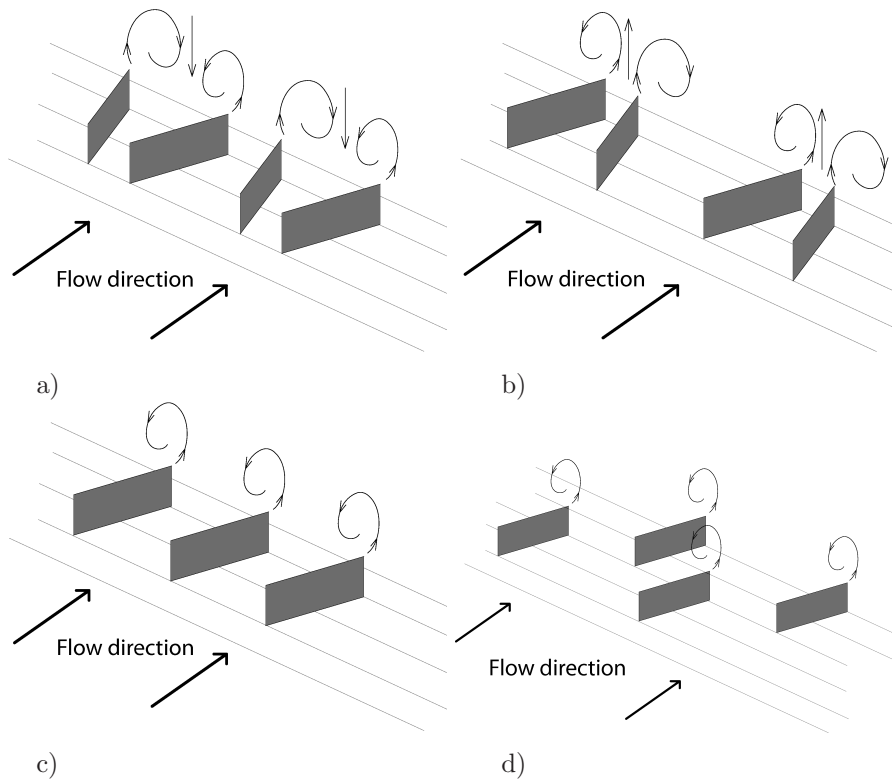


FIGURE 1.4. Vortex generators in a) counter-rotating "common flow down", b) counter-rotating "common flow up", c) co-rotating, and d) multiple-row set-ups.

devices generally comes along with a somewhat increased drag, especially if the VGs cannot be hidden when they are not needed. A way to avoid this drag penalty is to install VGs e.g. on surfaces that can be retracted if not needed, as can be seen in figure 1.1. This is a trade-off situation and it is not easy to predict the penalties and the disadvantages beforehand.

This thesis includes the application and the evaluation of a statistical method that may be used for simulating such VGs during the early design process. A considerable advantage of this method is that it removes the actual need to design VG geometries in a computational mesh that normally leads to a significant higher number of nodes and thus, longer preprocessing and computation time. Instead, the actual physical influences of the vortices in terms of additional stresses are simulated and then added to the mean governing equations. This results in negligible additional computational costs compared with computations without the statistical VG model but to tremendous savings when compared to computations with fully resolved VGs.

Theoretical background

2.1. Governing equations

Turbulent boundary layer flow of a viscous incompressible fluid with a free stream velocity U_∞ close to wall boundaries is studied in this thesis. The flow is generally regarded to be fully developed, statistically stationary, and two dimensional with respect to the z-axis in a statistical sense. Therefore, the turbulent flow is supposed to be governed by the continuity equation and the Navier-Stokes equations that read

$$\frac{\partial u_i}{\partial x_i} = 0, \quad (2.1)$$

$$\frac{\partial u_i}{\partial t} + u_j \frac{\partial u_i}{\partial x_j} = -\frac{1}{\rho} \frac{\partial p}{\partial x_i} + \frac{\partial}{\partial x_j} (2\nu s_{ij}), \quad (2.2)$$

with u_i and p as the instantaneous velocity and pressure fields, ρ and ν as the constant density and kinematic viscosity, respectively. The instantaneous strain rate tensor is denoted as $s_{ij} \equiv (u_{i,j} + u_{j,i})/2$. The strength of these equations is that they take all turbulence effects into account, from the smallest Kolmogorov scales until the largest geometric scales of the flow case. A numerical solution of equations 2.1 and 2.2 normally leads to an enormous amount of computational effort (e.g. for direct numerical simulations) and, thus, costs. Research is then mostly restricted to simpler geometries and considerably low or moderate Reynolds numbers and thus cuts back most of the engineering applications where turbulence occurs. Therefore, statistical approaches are commonly used and flow field variables are decomposed into a mean and a fluctuating part. The mean part is usually defined as the ensemble average over a large range of repetitions and the fluctuating part as the property for which the averaged value vanishes. According to this decomposition, see e.g. Pope (2000), the instantaneous velocity and pressure from equations 2.1 and 2.2 become

$$u_i = U_i + u'_i, \quad (2.3)$$

$$p = P + p', \quad (2.4)$$

denoting capital letter quantities as mean and small letter quantities with primes as fluctuating parts. From the above definition of the decomposition, it follows that the averaged equations 2.3 and 2.4 read

$$\bar{u}_i \equiv U_i, \quad \overline{u'_i} = 0, \quad (2.5)$$

and

$$\bar{p} \equiv P, \quad \overline{p'} = 0. \quad (2.6)$$

The decomposition of flow variables into a mean and a fluctuating part in equations 2.3 and 2.4 is commonly known as "Reynolds decomposition". Applying the Reynolds decomposition, plugging it in into equations 2.1 and 2.2 and ensemble averaging yields the Reynolds averaged Navier Stokes (RANS) equations for the mean flow:

$$\frac{\partial U_i}{\partial x_i} = 0, \quad (2.7)$$

$$\rho \frac{\partial U_i}{\partial t} + \rho U_j \frac{\partial U_i}{\partial x_j} = -\frac{\partial P}{\partial x_i} + \rho \frac{\partial}{\partial x_j} (2\nu S_{ij} - \overline{u'_i u'_j}), \quad (2.8)$$

where $S_{ij} \equiv (U_{i,j} + U_{j,i})/2$ is the mean strain rate tensor. By applying the Reynolds decomposition and multiplying equation 2.2 with the density ρ , the mean flow field momentum equation in equation 2.8 gains an additional stress term $-\rho \overline{u'_i u'_j}$ on the right-hand side, known as the Reynolds stress tensor. It represents the additional internal turbulence stresses that emerge due to velocity fluctuations and that act on the turbulent mean flow.

An expression for the Reynolds stress tensor $-\rho \overline{u'_i u'_j}$ can be derived from the Navier-Stokes equations but the problem lies in the generation of even higher order moments like $\overline{u'_i u'_j u'_k}$ which, in turn, contain even higher moments. This is commonly called the closure problem of turbulence. Here, turbulence modelling is the art of finding additional equations for this Reynolds stress term in order to close the system of equations and make it solvable. The aim is therefore to design a closed system of equations for the one-point quantities U_i , P and $\overline{u'_i u'_j}$. It is unclosed since the additional Reynolds stresses $-\rho \overline{u'_i u'_j}$ are not known as a function of U_i . Therefore, the Reynolds stress term in the system of equations 2.7-2.8 needs to be modelled, containing only known quantities.

2.2. A short introduction to turbulence modelling

As can be seen on the right-hand side in equation 2.8, the averaging of the nonlinear term generates an additional stress term $-\rho \overline{u'_i u'_j}$, called Reynolds stress tensor. This term is not negligible, it can have significant effects on the flow. This is the step where turbulence modelling starts, as mentioned in the previous chapter. An expression for this stress tensor is needed in order to close equation 2.8 together with U_i and P . Commonly, the Reynolds stress tensor is rewritten in a symmetric tensor form as the Reynolds stress anisotropy tensor

$$a_{ij} \equiv \frac{\overline{u'_i u'_j}}{K} - \frac{2}{3} \delta_{ij}, \quad (2.9)$$

where K is the mean turbulence kinetic energy defined as $\overline{u'_i u'_i}/2$. Turbulence modelling is needed to find an expression for $\overline{u'_i u'_j}$, or equivalently for a_{ij} , so that the system of equations 2.7-2.8 can be closed.

Different concepts exist and there are simpler and more complex closure proposals for a huge variety of different flow cases as well as computational resources. Some models are very resource-demanding whereas others are faster, yet often simpler and less complete than the more complex ones. A brief introduction into the different model approaches is given in this chapter, but the interested reader is referred to established literature in this field.

The simplest concept for the Reynolds stress anisotropy was suggested by Boussinesq (1877) and is given by a linear relation between the anisotropy tensor and the mean strain field S_{ij} and reads

$$a_{ij} = -2 \frac{\nu_T}{K} S_{ij}, \quad (2.10)$$

where ν_T is the so-called turbulent, or eddy viscosity.

Algebraic models form the simplest set of turbulence models, using the Boussinesq hypothesis as a starting point. Here, the turbulent eddy viscosity is usually derived from an initialised mixing length of the specific flow case, as suggested by Prandtl (1925). This means in turn that these algebraic models are incomplete, being dependent on a calibration of some coefficient within the model, e.g. through established experimental data. Depending on the specific flow case, the model needs to be calibrated so that no generality is given here. Other algebraic models are, according to Wilcox (1993), the two-layer Cebeci & Smith (1974) and Baldwin & Lomax (1978) models. There, two different turbulent eddy viscosity values are used for an inner and an outer layer when near wall flows are present.

Algebraic models work well when equilibrium turbulent flow is present, i.e. when the turbulent quantities vary slowly. Moreover, they are easy to implement and usually do not cause any numerical problems.

Another set of simple turbulence models based on the Boussinesq hypothesis complement equation 2.10 with one turbulent transport equation are called one-equation models. These models are incomplete though, since they typically assign the turbulence length scale to a characteristic dimension of the flow case. Different approaches exist, the Prandtl (1945) model e.g. solves for the turbulence kinetic energy whereas the model by Spalart & Allmaras (1992) considers a transport equation for the turbulence eddy viscosity ν_T . These models have the lack of not being very suitable for various types of flows and are therefore quite limited in their application. However, especially the Spalart-Allmaras model is still widely used, particularly in aircraft business.

One step further and more advanced than one-equation models are two-equation turbulence models. These models are complete, i.e. no information about the turbulent flow needs to be known a-priori. Consequently, they are suitable for a broader range of applications and the eddy viscosity ν_T is typically modelled by a combination of the characteristic velocity and length scales of the largest turbulent eddies. For that, two-equation models include a transport equation for determining the mean kinetic energy K and another transport equation for the length scale. Usual choices for the length scale determining quantity are the dissipation rate ϵ (Chou 1945; Launder & Spalding 1972), the turbulence time scale τ (Speziale *et al.* 1990), or the inverse turbulence time scale ω (Kolmogorov 1942; Wilcox 1988; Saffman 1970). All these models use a certain basis of set of equations that read (Hallbäck *et al.* 1995)

$$\frac{DK}{Dt} = 2\nu_T S_{ij} S_{ij} - \epsilon + \frac{\partial}{\partial x_i} \left[\left(\nu + \frac{\nu_T}{\sigma_k} \right) \frac{\partial K}{\partial x_i} \right], \quad (2.11)$$

$$\frac{DZ}{Dt} = C_{Z1} \frac{Z}{K} \mathcal{P} - C_{Z2} \frac{Z}{K} \epsilon + \left[\frac{\nu_T}{\sigma_Z} \frac{\partial Z}{\partial x_i} \right] + \text{Source}, \quad (2.12)$$

where Z denotes the length determining quantity, e.g. ϵ , τ , or ω . $\frac{D}{Dt}$ is the total rate of change, or material derivative, whereas σ_k and σ_Z are the Schmidt numbers. The form of the source term in equation 2.12 depends on the specific choice of Z as stated above. The eddy viscosity approach is with the help of dimensional analysis linked to the two transport equations 2.11 and 2.12 via the relation

$$\nu_T \propto K^m Z^n, \quad (2.13)$$

with different values for the coefficients m and n , depending on the specific quantity Z . By that, a closed form of equations is found and the system of equations 2.7 - 2.13 can be solved, containing the continuity equation, the momentum equation, the Boussinesq hypothesis, the platform equations, and the relation for the turbulence eddy viscosity. Moreover, each turbulence model includes closure coefficients that need to be calibrated in order to comply with turbulence properties. Nevertheless, and as Wilcox (1993) states, since the two-equations models are based on a dimensional analysis for the turbulence eddy-viscosity, they are not expected to be universally applicable, i.e. accurate.

One drawback of the Boussinesq hypothesis is that it solely relates the turbulence anisotropy tensor a_{ij} linearly to the mean strain rate tensor S_{ij} , as given in equation 2.10. Rotational effects are not included and thus, this approach is by nature limited from its beginning. One step further is rather to model transport equations for the Reynolds stresses than introducing some hypothesis with obvious deficits. This approach is generally known as differential Reynolds stress modelling (DRSM). Here, six additional equations for each Reynolds stress component add to the RANS equations 2.7 and 2.8. In order to close this set, a length determining quantity is again needed and therefore

DRSM modelling is often combined with existing or specially calibrated two-equation models replacing the equation for K , yet not using the Boussinesq hypothesis.

The Reynolds stress tensor $\overline{\rho u'_i u'_j}$, or for incompressible flows simply $\overline{u'_i u'_j}$ is derived from the Navier-Stokes equations by subtracting equation 2.8 for the mean velocity U_i from the momentum equation 2.2 for the instantaneous velocity $u_i = U_i + u'_i$. The resulting equation for u'_i is then combined into

$$\frac{D\overline{u'_i u'_j}}{Dt} = \mathcal{P}_{ij} - \epsilon_{ij} + \Pi_{ij} + \mathcal{D}_{ij}, \quad (2.14)$$

or, in terms of the anisotropy tensor a_{ij} ,

$$\frac{Da_{ij}}{Dt} = \mathcal{P}_{ij}^{(a)} + \frac{1}{K}\Pi_{ij} - \frac{\epsilon}{K}(e_{ij} - a_{ij}) + \mathcal{D}_{ij}^{(a)}, \quad (2.15)$$

where e_{ij} is the anisotropy of the dissipation rate tensor ϵ_{ij} reading

$$e_{ij} \equiv \frac{\epsilon_{ij}}{\epsilon} - \frac{2}{3}\delta_{ij}, \quad (2.16)$$

where the four terms on the right-hand side of equation 2.14 represent the production tensor, the dissipation rate tensor, the pressure-strain rate tensor, and the diffusion term of the Reynolds stresses, respectively. Turbulence modelling is needed for the three last terms, whereas the production tensor \mathcal{P}_{ij} is explicitly given if $\overline{u'_i u'_j}$ is known:

$$\mathcal{P}_{ij} \equiv -\overline{u'_i u'_k} \frac{\partial U_j}{\partial x_k} - \overline{u'_j u'_k} \frac{\partial U_i}{\partial x_k}. \quad (2.17)$$

As stated, the rest of the terms on the right hand side in equation 2.14 needs to be modelled whereas the major modelling challenge lies on the redistributive pressure-strain tensor Π_{ij} , leading to many different DRSM models in literature. Rotational mean flow effects enter equation 2.14 naturally, providing a major advantage over the eddy-viscosity models.

So-called algebraic Reynolds stress models (ARSM) form an alternative to the simpler linear eddy-viscosity two-equation models and the DRSM that may account for rather complex flow phenomena as e.g. system rotation and streamline curvature. Here, the Boussinesq hypothesis from equation 2.10 is completely replaced by an implicit algebraic relation for the Reynolds stress anisotropy tensor a_{ij} . This means that ARSMs are in turn also two-equation models, yet including some of the behaviour of the corresponding RST model as e.g. rotational and history effects. The general way to the ARSM follows the method proposed by Rodi (1976). Here, the starting point is the transport equation for $\overline{u'_i u'_j}$, or a_{ij} from the DRSM, compare with equation 2.9. Rodi's idea was to assume the convection and diffusion of a_{ij} to be very small in comparison with the other terms in equation 2.15. This can also be expressed by setting

$$\frac{Da_{ij}}{Dt} - \mathcal{D}_{ij}^{(a)} = 0, \quad (2.18)$$

assuming that the anisotropy a_{ij} is constant along mean streamlines, giving only slow changes in the flow field. The result is the implicit algebraic equation for a_{ij} :

$$0 = \mathcal{P}_{ij}^{(a)} - \frac{\epsilon}{K} (e_{ij} - a_{ij}) + \frac{1}{K} \Pi_{ij}. \quad (2.19)$$

Furthermore, this equation can be expressed by means of the mean strain rate tensor S_{ij} and the mean rotation rate tensor Ω_{ij} . Here, only the dissipation ϵ and the pressure-strain rate Π_{ij} need to be modelled.

Numerical problems, a lack of stability, and slow convergence are the main drawbacks when an implicit ARSM approach is used. This may even lead to higher computational effort than for the DRSM approach so that one might question the need for simplifying the DRSM approach then. Due to that, researchers have thought about simplified solution strategies, and especially explicit algebraic Reynolds stress models (EARSM) have made it possible to maintain the algebraic two-equation modelling that also includes the important features of the DRSM while removing the cumbersome numerical problems of the ARSM approach. The core of the EARSM is that the anisotropy tensor a_{ij} is expressed by a purely algebraic expression $a_{ij} = f(S_{kl}, \Omega_{kl})$ that relates the anisotropy to the mean strain rate and rotation tensors, respectively.

Different descriptions for EARSM modelling exist in literature (Gatski & Speziale 1993; Wallin & Johansson 2000) due to the reason of different modelling assumptions that enter through equation 2.19 and the algebraic relation $a_{ij} = f(S_{ij}, \Omega_{ij})$.

In this thesis and in the included papers, the DRSM approach was used for the application of the VG model since the VG model describes the different additional vortex stress components that are in turn added to the corresponding Reynolds stress tensor components in the DRSM description. For the case of the fully 3D resolved computations, the EARSM was applied since the fully resolved approach did not include the statistical description of the vortices but instead resolved for the VG devices and the vortex structures in a 3D mesh.

Statistical modelling of passive vortex generators

3.1. Passive vortex generators for flow control

Flow control devices like passive vane VGs have been found in many engineering applications for quite some time now. Probably the most famous example is the application on aircraft wings, leading to enhanced flow for different flight conditions. VG vanes are found in many different configurations that generate co-rotating as well as counter-rotating vortices originating from "common flow down" and "common flow up" VG pair configurations but also multiple-row systems are possible, compare with figure 1.4.

Rectangular, triangular/delta, trapezoid shaped, but also wedges and other forms occur in many research papers, see e.g. figure 3.1. Typically, VGs are mounted perpendicularly on the surface, with an angle of incidence towards the mean flow direction (except e.g. wedges as shown in figure 3.1 a)). Physically, these devices all have in common that they generate certain vortex structures downstream in the flow. These vortex structures in turn mix the flow by means of their radial velocity component and, by that, give rise to higher streamwise velocities close to the wall and reduced streamwise velocity further away from it. This phenomena is a result of the generation of stresses and their transport in the flow that on the other hand have an impact on the mean velocities. In conclusion it can be said that the boundary layer velocity profile becomes fuller downstream of such flow control devices where high momentum flow is pushed down and vice versa where it is pushed away. Nevertheless, the overall momentum transfer down to the wall and the VG efficiency is different for different configurations. In total, VGs maintain the flow to be more stable by boundary layer mixing processes, resulting in delayed or even prevented boundary layer separation.

3.2. Analytical methods

As mentioned previously, the main object of this thesis was to evaluate a statistical VG model, previously described by Törnblom & Johansson (2007). For that, some basic analytical methods are needed which in turn are then implemented numerically. Here, the physical influences of the VGs in terms of additional vortex stresses will be added to the mean governing equations. The

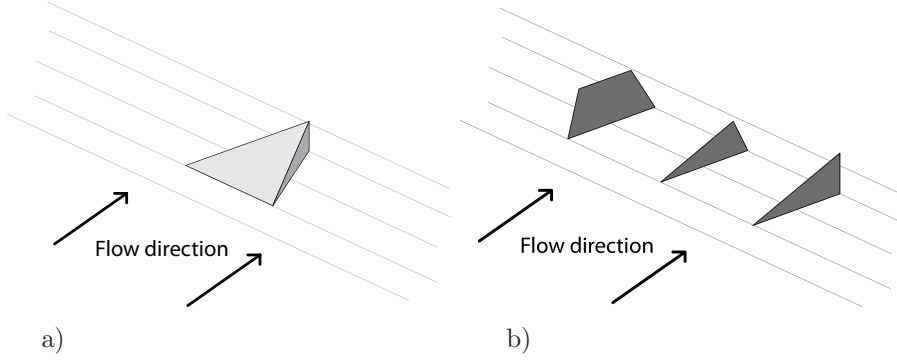


FIGURE 3.1. Vortex generator systems: a) wedge, and b) trapezoid/delta set-ups.

required analytical methods are presented in this section and the following section uses these theories in order to set-up a numerical VG model that builds on the analytical methods.

3.2.1. Lifting line theory

Each VG vane is considered to be a small wing mounted on the wall surface, see also figures 1.1 and 3.2. Such a vane is then analysed by using the lifting line theory (Glauert 1926, LLT) in order to determine the maximum value Γ_{max} that is in turn later used in chapter 3.2.2 for calculating the azimuthal vortex velocity field and the additional vortex stresses for the VG model. The circulation distribution over a wing according to the LLT is therefore given by

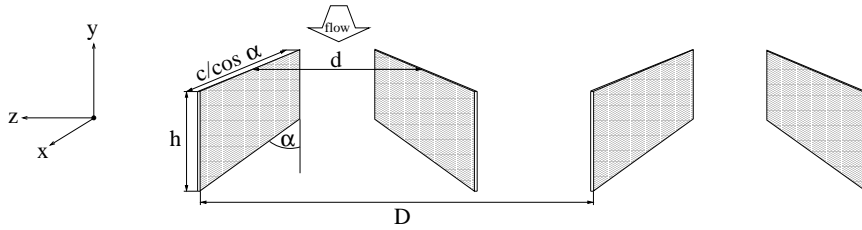


FIGURE 3.2. Vortex generator pairs in a counter-rotating setting and their notation.

$$\Gamma(y) = \frac{K}{2} U(y) c(y) \left[\alpha(y) - \frac{w(y)}{U(y)} \right], \quad (3.1)$$

where $U(y)$ is the incoming flow velocity distribution across the wing, $c(y)$ the chord distribution, K the lift slope at zero angle of attack and $w(y)$ the

downwash velocity distribution

$$w(y) = \frac{1}{4\pi} \int_{-h}^h \frac{d\Gamma}{dy'} \frac{1}{y' - y'_0} dy'. \quad (3.2)$$

The term in square brackets in equation 3.1 specifies the effective angle of attack

$$\alpha_{eff}(y) = \alpha(y) - \frac{w(y)}{U(y)}, \quad (3.3)$$

that develops due to the finite blade aspect ratio \mathcal{R} , introducing a spanwise varying induced angle of attack

$$\alpha_{ind}(y) = \tan\left(\frac{w(y)}{U(y)}\right) \approx \frac{w(y)}{U(y)}, \quad (3.4)$$

for small angles α_{ind} which is the case here.

Nevertheless, the LLT only holds for high aspect ratio (\mathcal{R}) wings in free flight conditions for small angles of attack α far away from obstacles in inviscid flow. By modelling VGs that are mounted on a wall in a boundary layer flow by means of the LLT, some of its assumptions are not valid anymore as a result of:

1. a boundary layer velocity profile $U(y)$ in viscous wall-bounded flow instead of a constant free stream velocity U_∞ in inviscid flow,
2. VGs being wings with very low \mathcal{R} ,
3. possible side effects due to the proximity of neighbouring VG blades, i.e. neighbouring vortices,
4. a reasonable high angle of incidence α (corresponding to the angle of attack α for free flight in the LLT) of the VG blades.

Therefore, the LLT should be considered as an approximation to estimate the circulation distribution $\Gamma(y)$ across one single VG blade. In turn, the circulation distribution $\Gamma(y)$ quantitatively describes the generated lift, the induced drag and the vortex strength that is in turn needed as an input for the VG modelling. The vortices are then represented by a 2D Lamb-Oseen vortex model with the azimuthal velocity distribution which is described in chapter 3.3.2.

3.2.2. Solution method for the lifting line theory

In a next step, it is necessary to solve equation 3.1 numerically by means of a Fourier sine series. A suitable transformation for the y -coordinate of one VG vane and its mirror image is

$$y(\theta) = -h_{VG} \cos(\theta), \quad (3.5)$$

with $0 \leq \theta \leq \pi$ as the new y -coordinate limits. The Fourier series ansatz to solve equation 3.1 is (Glauert 1926):

$$\Gamma(\theta) = 4h_{VG}U_{ref} \sum_{n=1}^{\infty} A_n \sin(n\theta). \quad (3.6)$$

The induced downwash $w(\theta)$ for a certain spanwise position θ is then given by

$$\begin{aligned} \frac{w(\theta)}{U_{ref}} &= \frac{1}{4\pi} \int_0^\pi \frac{d\Gamma(\theta')}{d\theta'} \frac{d\theta'}{\cos \theta' - \cos \theta} \\ &= \frac{1}{\pi} \int_0^\pi \frac{\sum_{n=1}^\infty n A_n \cos(n\theta')}{\cos \theta' - \cos \theta} d\theta' \\ &= \sum_{n=1}^\infty n A_n \frac{\sin(n\theta)}{\sin \theta}, \end{aligned} \quad (3.7)$$

where the standard integral

$$\int_0^\pi \frac{\cos(n\theta') d\theta'}{\cos \theta' - \cos \theta} = \frac{\pi \sin(n\theta)}{\sin \theta} \quad (3.8)$$

is used. Equations 3.6 and 3.7 are plugged into equation 3.1, leading to the system of equations

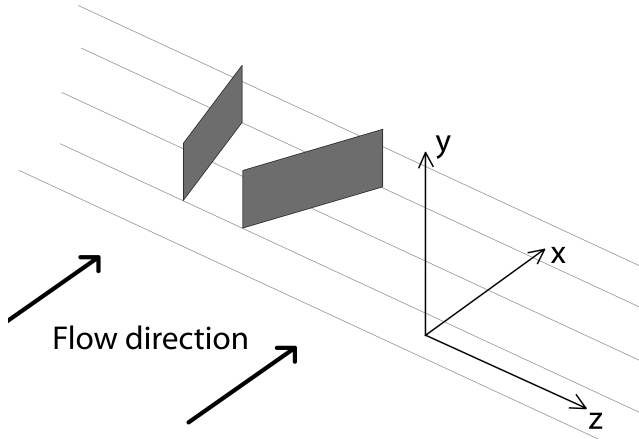
$$\sum_{n=1}^\infty A_n \sin(n\theta)(\mu(\theta)n + \sin \theta) = \mu(\theta) \frac{U(\theta)}{U_{ref}} \alpha(\theta) \sin \theta, \quad (3.9)$$

where $\mu(\theta) = Kc(\theta)/8h_{VG}$. This system of equations can be solved by a truncation of the series for $n = N$ VG pairs and solving at $M = (N - 1)/2$ collocation points for the half-wing VG vane in boundary layer flow, i.e. $0 \leq y \leq h_{VG}$ and $\frac{\pi}{2} \leq \theta \leq \pi$, respectively. The solution for A_n is then used for solving for the circulation distribution $\Gamma(y)$ across one VG blade which is in turn used for computing the additional vortex velocity field in the next chapter.

3.3. Numerical methods

3.3.1. Vortex generator modelling

As the core of this statistical approach, the additional physical effects of the vortices will be statistically modelled in order to reduce setup and calculation time. This is done by adding the additional stress contributions from the vortices to the turbulence stresses in the flow. Therefore, the VG model must be able to mimic the vortex effects in the flow. Here, a 2D Lamb-Oseen vortex model, giving additional azimuthal vortex velocities was used for the modelling, according to Törnblom (2006) and Törnblom & Johansson (2007). The resulting additional vortex stresses are supposed to be applicable also in 2D flows. As the model is a 2D vortex model, acting in a yz -forcing plane (see also figure 3.3) perpendicular to the streamwise x -direction, the additional vortex stresses need to be spanwise averaged in the z -direction in order to add the y -dependent additional vortex stress contributions to the mean flow equations. This procedure leads to the additional spanwise averaged second-order statistics $\Delta \overline{v'v'}(y)$ and $\Delta \overline{w'w'}(y)$. It must be stated that the 2D Lamb-Oseen vortex model does not account for a streamwise velocity component $u'(y, z)$. Therefore, the additional stresses $\Delta \overline{u'u'}(y)$ and $\Delta \overline{u'v'}(y)$ cannot be taken into account and are therefore not forced. Furthermore, the additional stresses $\Delta \overline{u'w'}(y)$ and $\Delta \overline{v'w'}(y)$ vanish when statistically spanwise averaged in the z -direction.

FIGURE 3.3. *The orientation of the coordinate system axes.*

3.3.2. Vortex model

For the computations, the VGs from the experiments were assumed to generate self-similar 2D Lamb-Oseen vortices with an azimuthal velocity field distribution

$$u_{\Phi}(r) = \frac{\Gamma_{max}}{2\pi r} \left[1 - \exp\left(\frac{-r^2}{r_0^2}\right) \right], \quad (3.10)$$

with Γ_{max} as the maximum value of the circulation distribution around the blade $\Gamma(y)$, determined from the LLT (see chapter 3.2.1) and r_0 as the vortex core radius of the vortex model. An example plot for the circulation distribution $\Gamma(y)$ around a finite wing in free flight and a VG blade attached on a wall in a boundary layer is shown in figure 3.4. It is clearly seen that the circulation distribution around a VG vane in a boundary layer flow is less compared to a corresponding wing geometry in free flight conditions. Moreover, the maximum circulation Γ_{max} for both flow cases is located at different locations, giving a maximum circulation Γ_{max} at the wing root for the free flight case. In contrast to this, the boundary layer flow case establishes a maximum circulation Γ_{max} some distance away from the VG root. The reason that $\Gamma(y)$ does not go back to zero for the boundary layer flow case, even though it is described by equation 3.1, is due to the fact that the used Fourier series ansatz, compare chapter 3.2.2, does not use collocation points directly on the wall boundary. Nevertheless, the exact distribution of $\Gamma(y)$ close to $y/h_{VG} = 0$ is not important for the VG model approach since Γ_{max} occurs for higher values y/h_{VG} .

For a first test of the model, the model input parameters r_0/h_{VG} and K were set to 0.1 and 2π , respectively. An example plot of the vortex model azimuthal velocity distribution $u_{\Phi}(r)$ is given in Fig. 3.5. After determining Γ_{max} by means of the LLT, the resulting velocity field $\mathbf{u}(y, z)$ of a VG array is identified by a superposition of all azimuthal velocity fields $u_{\Phi}(r)$ from each

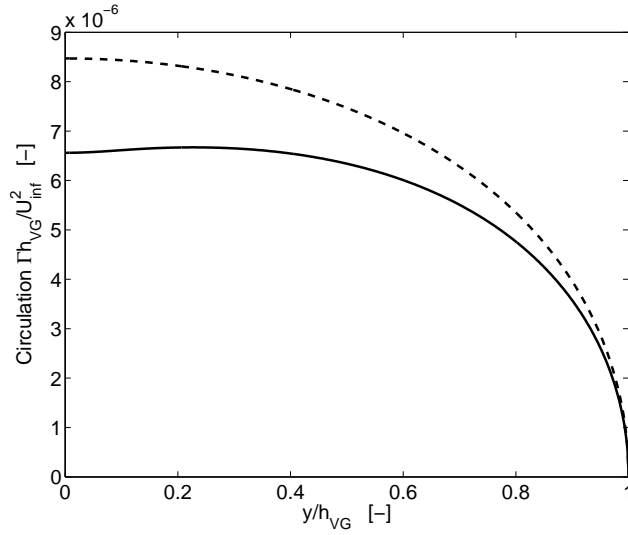


FIGURE 3.4. Circulation distribution around a modelled vortex generator in free stream (- -) and mounted in boundary layer flow (-).

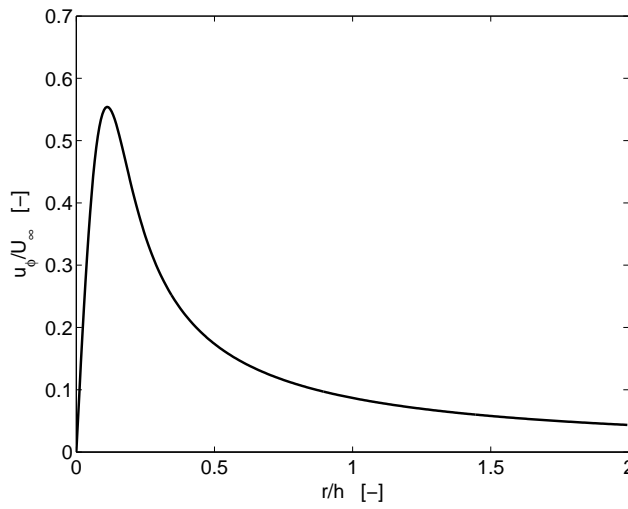


FIGURE 3.5. Azimuthal vortex velocity distribution of the 2D Lamb-Oseen vortex model, $r_0 = 0.1$.

VG and its modelled mirror image, see also figure 3.6. The resulting flow field $\mathbf{u}(y, z)$ for $n = 5$ VGs is partly shown in figure 3.7 where the effect of the mirror images can be observed, too, resulting in a modelled solid wall boundary at $y = 0$. In order to obtain the additional stresses that are caused by the vortices,

the velocity field $\mathbf{u}(y, z)$ is split into its velocity components $v(y, z)$ and $w(y, z)$ in the y - and z -direction, respectively, and according to Törnblom & Johansson (2007):

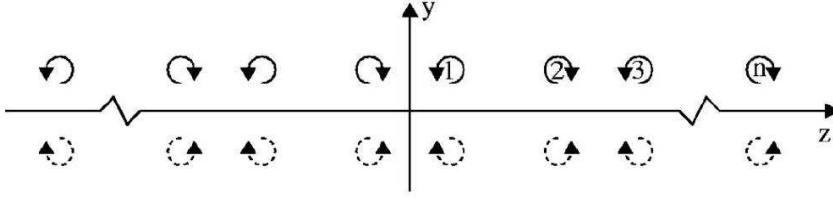


FIGURE 3.6. Vortex array with n VG pairs and their mirror images for computing the total superpositioned vortex-induced velocity field $u'_i(y, z)$ in the VG model forcing plane, taken from Törnblom & Johansson (2007).

$$[v, w] = \sum_{n=1}^{\infty} (-1)^{n+1} \sum_{m=1}^4 (-1)^{m+1} \frac{u_{\Phi}(r_m)}{r_m} [\Delta z_m, -\Delta y_m], \quad (3.11)$$

where

$$r_m = \sqrt{\Delta y_m^2 + \Delta z_m^2}, \quad (3.12)$$

and

$$\Delta y_1 = y - h, \quad \Delta z_1 = z - z_n, \quad (3.13)$$

$$\Delta y_2 = y + h, \quad \Delta z_2 = z - z_n, \quad (3.14)$$

$$\Delta y_3 = y + h, \quad \Delta z_3 = z + z_n, \quad (3.15)$$

$$\Delta y_4 = y - h, \quad \Delta z_4 = z + z_n. \quad (3.16)$$

The resulting vortex velocity field is in this case only valid for a counter-rotating VG array with identical VG pairs in the absence of cross flow. In general, the vortex velocities $[v, w]$ from equation 3.11 are then assumed to act as fluctuating velocity parts $u'_i = [0, v, w]$ in the VG model forcing plane.

3.3.2.1. Reynolds stresses adding

The concept of this vortex model approach and describing its effects on the flow is to assume that the second-order statistics of the additional vortex velocity field $[v, w]$, or as assumed u'_i , from equation 3.11 act as additional turbulence stresses on the mean flow. By making this assumption, the additional spanwise averaged contributions $\Delta \overline{u'_i u'_j}(y)$ to the Reynolds stresses are

$$\Delta \overline{u'_i u'_j}(y) = \frac{1}{D} \int_{-D/2}^{D/2} u'_i(y, z) u'_j(y, z) dz. \quad (3.17)$$

It is sufficient to integrate and spanwise average the second-order statistics in equation 3.17 over one VG pair distance D only since the resulting vortex

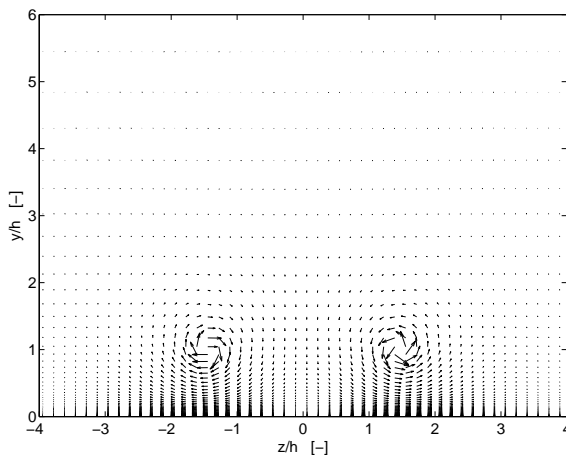


FIGURE 3.7. *Vortex velocity field in the VG model forcing plane.*

flow field is periodic. Additional contributions are only nonzero for $\Delta \overline{v'v'}$ and $\Delta \overline{w'w'}$. Moreover, a wall damping function, e.g. $(1 - \exp(-20y/h))$, needed to be introduced and applied on equation 3.17 because the vortex velocities in the spanwise direction at the wall boundary $y = 0$ will not cancel out and would result in a finite value.

In that way, a summation of the 2D boundary layer Reynolds stresses $\overline{u'_i u'_j}(y)$ (figure 3.8) with the additional spanwise averaged turbulent vortex stresses $\Delta \overline{u'_i u'_j}(y)$ (figure 3.9) from the VG model is made. This forms a new superposed distribution of the total Reynolds stresses stresses in the flow, see figure 3.10.

A DRSM turbulence model was used to properly describe the development of the total Reynolds stresses downstream of the VG plane. Furthermore and unlike simpler turbulence models, the DRSM turbulence model makes it possible to account for the energy transfer between the different components of the Reynolds stress tensor, enabling production of the $\overline{u'v'}$ Reynolds stresses through $\mathcal{P}_{12} = \overline{v'v'} \frac{\partial U}{\partial y}$.

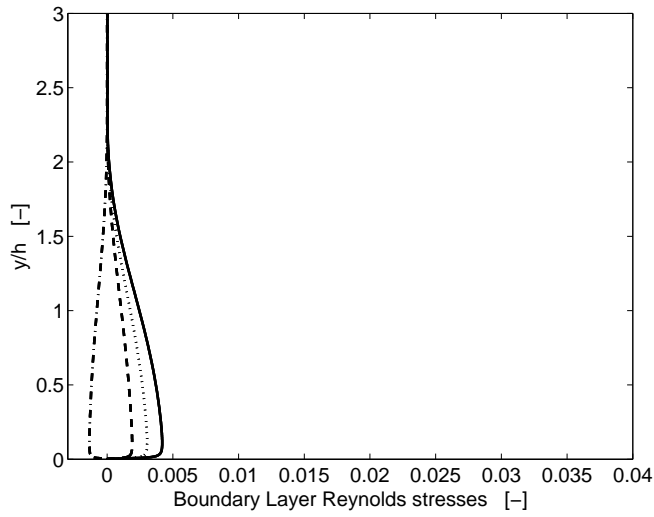


FIGURE 3.8. Incoming boundary layer Reynolds stresses $\overline{u'v'}$ ($\cdot - \cdot$), $\overline{u'u'}$ ($-$), $\overline{v'v'}$ ($- -$), and $\overline{w'w'}$ ($\cdot \cdot$) at the VG model location.

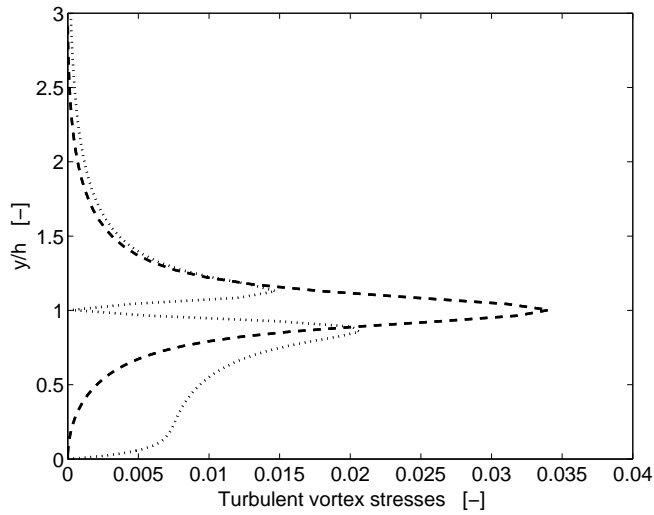


FIGURE 3.9. Additional $\Delta \overline{v'v'}$ ($- -$) and $\Delta \overline{w'w'}$ ($\cdot \cdot$) vortex stresses at the VG model location.

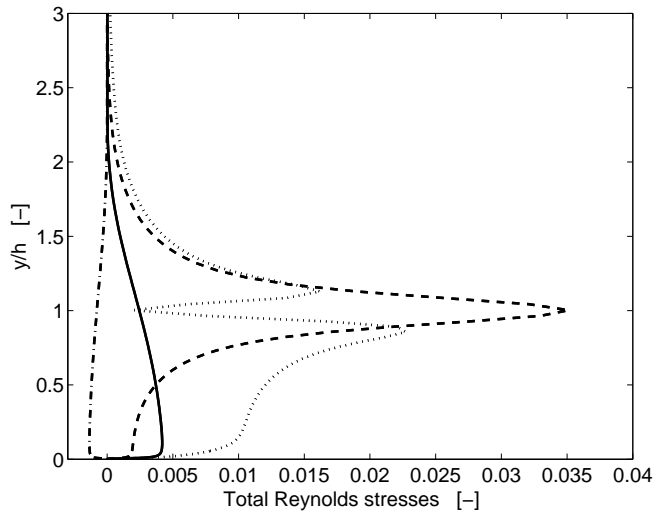


FIGURE 3.10. *Superposition of the additional vortex stresses and the boundary layer Reynolds stresses at the VG model location, $\overline{u'v'}$ ($\cdot - \cdot$), $\overline{u'u'}$ ($-$), $\overline{v'v'}$ ($- -$), and $\overline{w'w'}$ (\cdots).*

Results and discussion

4.1. Flat plate in zero pressure gradient flow

The study of the VG model and its parameters, comparable fully resolved VG computations, and experiments have generally shown that the VG model is able to capture and simulate flow separation prevention and delay for the flow cases examined.

The current model incorporates, as described in chapter 3.3.2, a 2D Lamb-Oseen vortex model that does not force the axial velocity component. Due to that, the originating vortex stresses do not include those components that need the u' -velocity fluctuation parts to be formed. The investigations of the zero pressure gradient (ZPG) flat plate flow have shown that the $\overline{u'v'}$ and $\overline{u'u'}$ vortex stresses (both of them are consequently not initially forced) are formed through the production and redistribution terms in the DRSM model. This leads to a postponed influence of the VG model on these stresses during their streamwise development as can be observed in the nearfield plots of the $\overline{u'v'}$ and $\overline{u'u'}$ Reynolds stresses in figure 4.1 a) and c). It can be seen that the $\overline{u'v'}$ Reynolds stresses catch up well with the experimental and spanwise averaged 3D fully resolved distributions, whereas the $\overline{u'u'}$ component still shows some discrepancies when compared with the experiments and 3D computations. They are not directly forced through the production term as $\overline{u'v'}$, but indirectly through slow effects described by the pressure strain rate tensor Π_{ij} , compare with equation 2.14. The differences remain for the whole nearfield and farfield region (figure 4.1 d)), indicating that the turbulence description is not capable of exactly capturing the real flow state with modelled vortices in the flow. For larger distances, compare figure 4.1 b), the $\overline{u'v'}$ stress distribution for all three cases (VG model, fully resolved, and experiments) are more similar to each other until the VG model results deviate observably again for higher streamwise positions $x/h_{VG} > 9.4$. This is due to the fact that the modelled vortices are included in the turbulent description where the diffusive and redistributive effects smear out the vortex stresses influence in the Reynolds stresses. On the other hand, the fully resolved and the experimental results resolve for the real vortex structures that, by nature, are more stable and therefore persist longer in the flow. For very large distances, the stress distributions become similar again, indicating that the vortex structures have also diffused or broken down, respectively.

Figure 4.2 shows the forced components $\overline{v'v'}$ and $\overline{w'w'}$ of the Reynolds stress tensor and its streamwise development on the flat plate. The forcing of the VG model can be easily recognised in the very left plots in 4.2 a) and c), especially when comparing with figures 3.8 and 3.9. Again, it is seen that the turbulent diffusive and redistributive effects smooth and smear out the stress distributions and the differences between the different cases grow visibly for streamwise positions $x/h_{VG} > 9.4$, compare 4.2 b) and d). Still, the distributions become similar again for very large distances for the same reason as stated previously.

Checking the influence of exact initial conditions for the vortex stresses, i.e. not from the VG model but from spanwise averaged fully resolved 3D computations, the streamwise development of the Reynolds stresses within the turbulence model can be studied in figures 4.3 and 4.4 where the far left distributions in subplots a) and c) are congruent with each other, originating from the exact imposed initial conditions. The overall conclusion from this investigation is that the nearfield development is drastically changed whereas the farfield development shows similar behaviour compared to the application of the VG model. This gives rise to the fact that the diffusive and redistributive effects dominate further away from the forcing plane so that the initial description of additional vortex stresses becomes less important here. On the other hand, nearfield effects may have some important influence, especially when it comes to real applications in APG flow with existing separated regions.

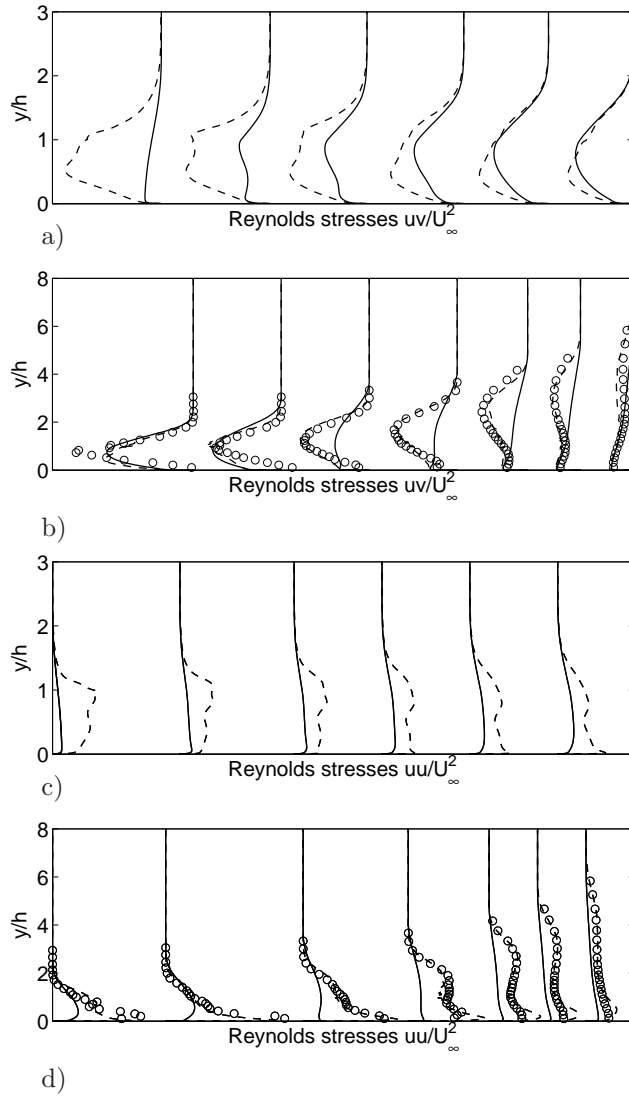


FIGURE 4.1. Vortex generator model (—), spanwise averaged fully resolved (---), and experimental (o, only b) and d)) nondimensional wall-normal $\overline{u'v'}/U_\infty^2$ and $\overline{u'u'}/U_\infty^2$ Reynolds stress distributions at streamwise positions x/h_{VG} downstream of the vortex generator plane: a) and c) nearfield $x/h_{VG} = 0.0, 0.5, 1.1, 1.7, 2.2,$ and 2.8 ; b) and d) farfield $x/h_{VG} = 3.3, 9.4, 23, 37, 65, 93,$ and 148 (from left to right).

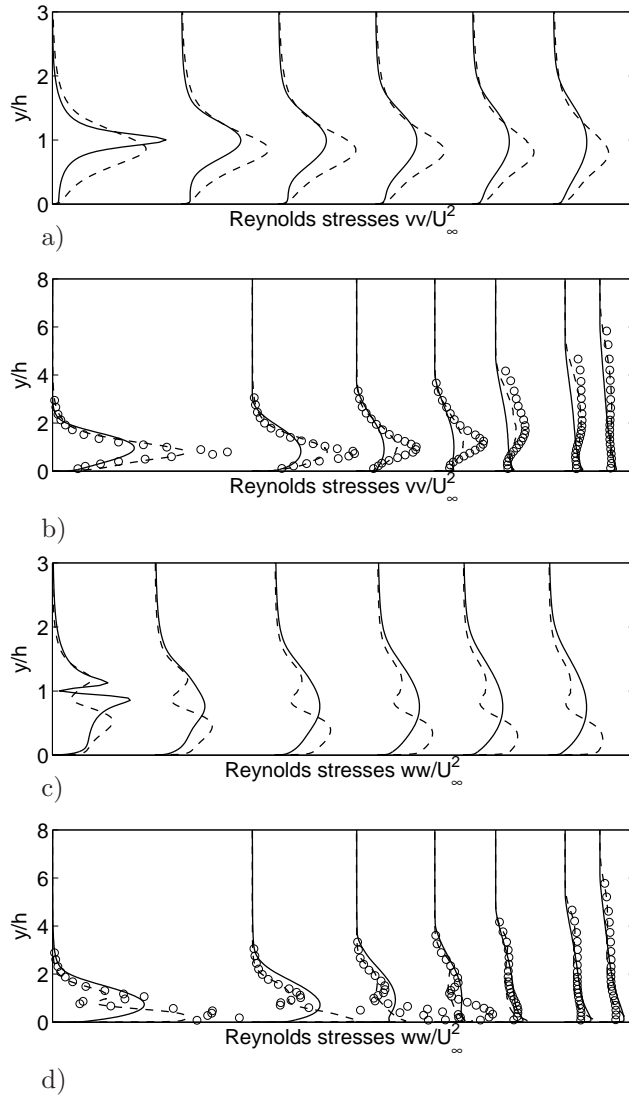


FIGURE 4.2. Vortex generator model (—), spanwise averaged fully resolved (---), and experimental (o, only b) and d)) nondimensional wall-normal $\overline{v'v'}/U_\infty^2$ and $\overline{w'w'}/U_\infty^2$ Reynolds stress distributions at streamwise positions x/h_{VG} downstream of the vortex generator plane: a) and c) nearfield $x/h_{VG} = 0.0, 0.5, 1.1, 1.7, 2.2, 2.8$; b) and d) farfield $x/h_{VG} = 3.3, 9.4, 23, 37, 65, 93, 148$ (from left to right).

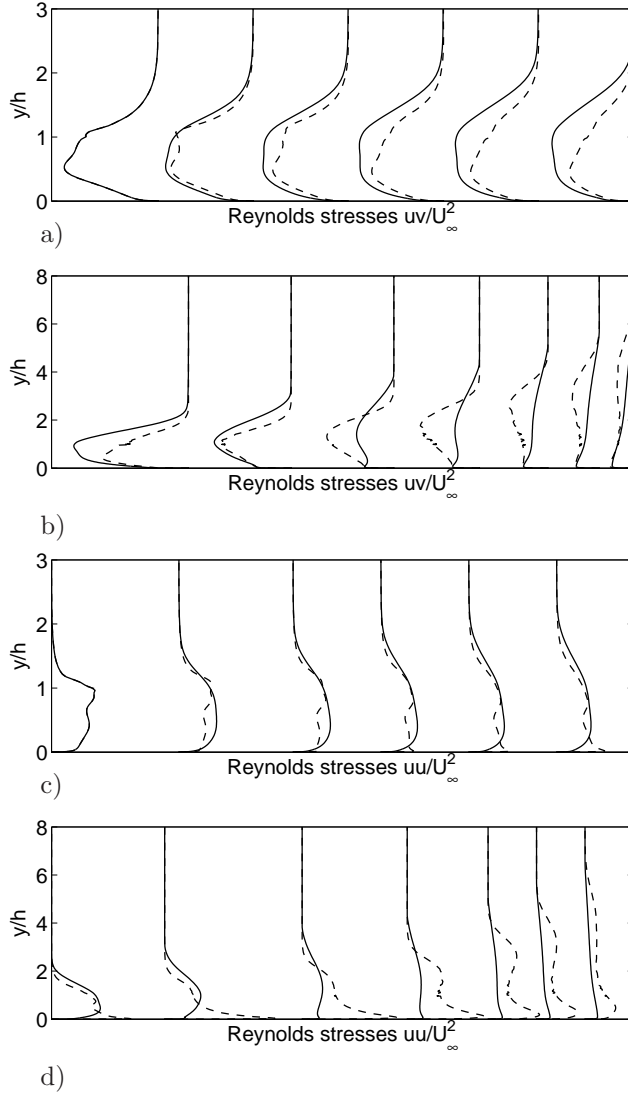


FIGURE 4.3. Computations with spanwise averaged fully resolved initial conditions (—), and spanwise averaged fully resolved (---) nondimensional wall-normal $\overline{u'v'}/U_\infty^2$ and $\overline{u'u'}/U_\infty^2$ Reynolds stress distributions at streamwise positions x/h_{VG} downstream of the vortex generator plane: a) and c) nearfield $x/h_{VG} = 0.0, 0.5, 1.1, 1.7, 2.2,$ and 2.8 ; b) and d) farfield $x/h_{VG} = 3.3, 9.4, 23, 37, 65, 93,$ and 148 (from left to right).

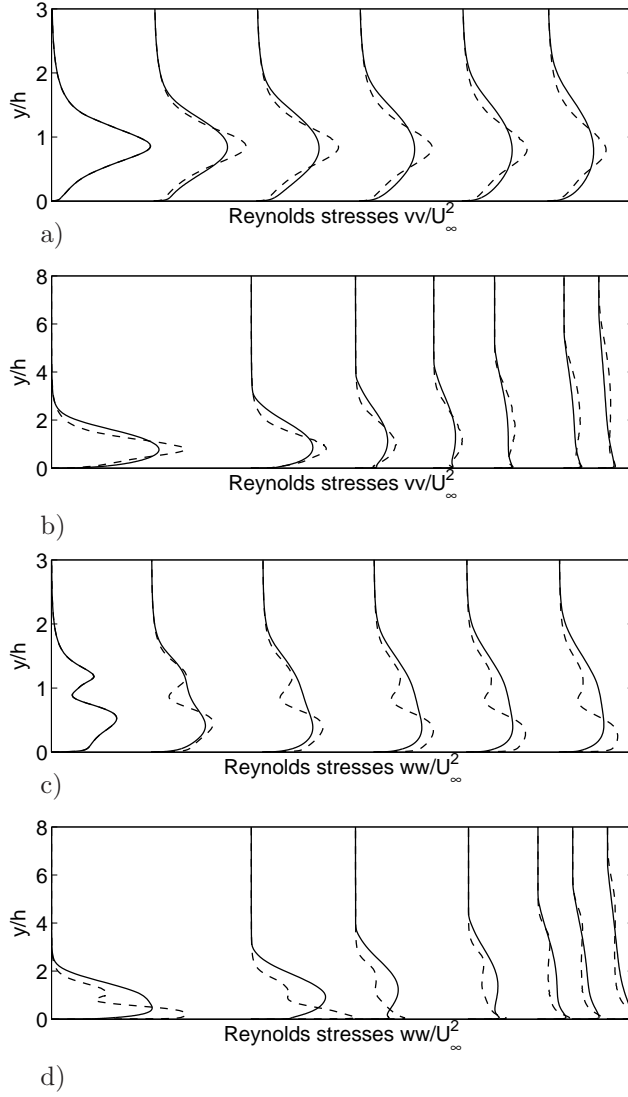


FIGURE 4.4. Computations with spanwise averaged fully resolved initial conditions (—), and spanwise averaged fully resolved (---) nondimensional wall-normal $\overline{v'v'}/U_\infty^2$ and $\overline{w'w'}/U_\infty^2$ Reynolds stress distributions at streamwise positions x/h_{VG} downstream of the vortex generator plane: a) and c) nearfield $x/h_{VG} = 0.0, 0.5, 1.1, 1.7, 2.2,$ and 2.8 ; b) and d) farfield $x/h_{VG} = 3.3, 9.4, 23, 37, 65, 93,$ and 148 (from left to right).

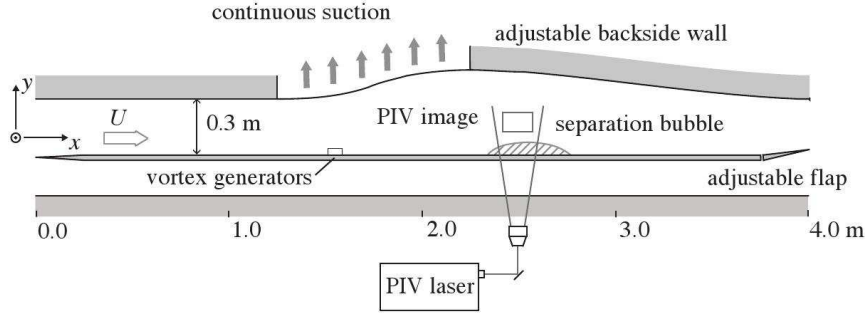


FIGURE 4.5. Sketch of the boundary layer wind tunnel test section used in experiments, taken from Lögberg *et al.* (2009).

4.2. Flat plate in adverse pressure gradient flow

The behaviour of the VG model was also investigated in adverse pressure gradient (APG) flat plate flow according to the experiments carried out by Lögberg *et al.* (2009). Here, the VGs were placed within the suction and diverging section of the BL wind tunnel at KTH, see also figure 4.5. Due to the APG, a separation region was formed some distance downstream of the VG position and the influence of different suction rates, hence APG rates, and VG configurations was investigated by Lögberg.

The VG model was, as a complement to the previous ZPG case, applied to this APG flow case in 2D. Nevertheless, the APG region in the computations needed to be generated without a suction system, yet with a pressure/velocity forcing on its top boundary. It is pointed out here that the boundary conditions were not completely the same as in experiments, and the separated region occurred 0.30 m more upstream than in experiments, as well as being 0.10 m shorter. Computations of a clean flat plate, with the VG model applied, and fully resolved 3D computations were also carried out.

Nevertheless and despite the limitations that the VG model showed in the previous chapter, its application in APG flow on a flat plate has proven to be sensitive enough for predicting correct trends and tendencies for flow separation prevention. Local skin friction distributions including results of the clean flat plate (FP2D), the VG model applied at the baseline position (VG2D), and spanwise averaged fully resolved 3D results are presented in figure 4.6. It can be clearly seen how the VG model predicts a flow separation prevention compared to the clean flat plate case. Still, the VG model results lie somewhat beneath the fully resolved data, indicating that its influence is under estimated.

A streamwise position variation of the VG model, similar to experiments, is presented in figure 4.7. Here, the local skin friction coefficient is shown for three chosen VG model positions (first three according to the legend) that were located some distance upstream of the separation bubble. Moreover, a VG

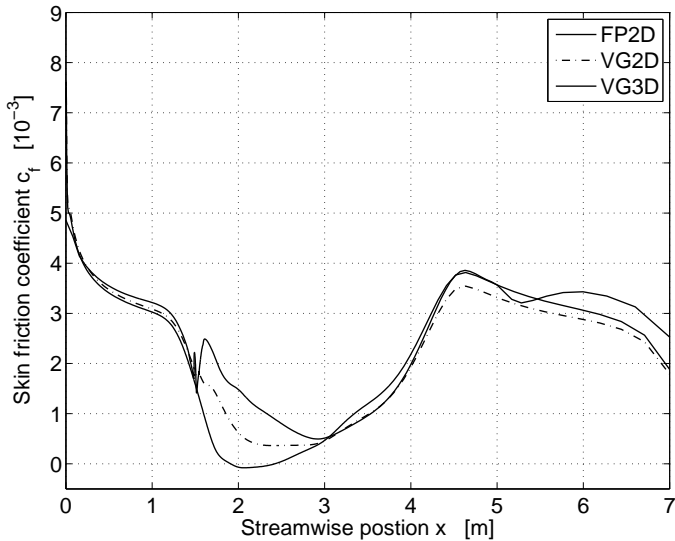


FIGURE 4.6. Local skin friction coefficient distributions for the clean flat plate (FP2D), the VG model applied (VG2D), and spanwise averaged fully resolved 3D (VG3D) computations.

height variation from 18 mm (dotted line) to 10 mm (dashed-dotted line) at $x = 1.70$ m is also included in figure 4.7. One can see that the first two graphs according to the figure legend represent VGs that are located further upstream from the separation bubble, giving an attached flow state. On the other hand, the second last graph (dotted line) is located closer to the separated region and represents a flow state close to separation, since the graph comes close the skin friction zero-line. For the VG height variation from $h_{VG} = 18$ mm to 10 mm, it can be observed that a separated flow region develops for the region around $2 \text{ m} < x < 2.5 \text{ m}$, observable by a local skin friction coefficient $c_f \leq 0$. This result is similar to what Lögdberg *et al.* (2009) observed in his experiments, see table 4.1. The parameter γ_e in figure 4.7 and table 4.1 indicates the position and height variation in experiments and is defined in Lögdberg *et al.* (2009) as

$$\gamma_e \equiv 2k \frac{h_{VG} U_{VG}}{D}, \quad (4.1)$$

where k is a coefficient that takes the VG geometry into account (k was set to 0.6 according to Lögdberg *et al.* 2009), h_{VG} the VG height, U_{VG} the VG tip velocity, and D the VG pair distance in the spanwise direction.

The results prove that global flow separation prevention in APG flows is possible with the VG model even though the ZPG flat plate results previously showed the limitations of the VG model regarding the Reynolds stresses and their streamwise development. In general, it was shown that it is beneficial to

use VGs and the VG model in order to prevent flow separation. Nevertheless, flow control devices should not be placed very close to the separated region, since they remain useless there. A decreased mean flow velocity at the modelled VG blade tips generates weaker vortex stresses through the VG model description. Despite this, it might be the case that experiments prove that VG are capable of preventing flow separation here since u' fluctuations are still present in the flow and might have a strong effect on generating vortices even in regions of very much decreased mean flow. Unfortunately, there are no experimental results available for even closer VG position relatively to the separated region. In the range investigated, the VG model proved to predict correct trends and flow states. Nevertheless, the VG model approach does not capture such u' fluctuations, probably under estimating the beneficial effects of VGs for further downstream locations.

Moreover, further parameter variations of the streamwise location of the VG model detected an optimal VG model position close to $x \approx 1.25$ m at the beginning of the APG section. Placing the VG model further downstream resulted in less efficient flow control for the reasons described in the previous section, just as when the VG model was located further upstream of that position. There, even though strong vortex stresses are generated through the VG model, these stresses are diffused much earlier and lose their beneficial effects on the mean flow separation prevention when they have travelled downstream to the separated region. Therefore, an optimal position is found, being close to $x \approx 1.25$ m.

Further VG model parameter variations were carried out and the interested reader is referred to Paper 2 of this thesis.

TABLE 4.1. The VG circulation per unit width, VG heights, the VG streamwise locations $x_{VG_{exp}}$ in the APG experiments of Lögdberg *et al.* (2009) for case II, the flow states in experiments, corresponding VG streamwise locations $x_{VG_{mod}}$ for the VG model computations, and the flow states in VG model computations; (exp. $\hat{=}$ experiment, att. $\hat{=}$ attached, sep. $\hat{=}$ separated).

γ_e [m/s]	h_{VG} [mm]	$x_{VG_{exp}}$ [m]	flow, exp.	$x_{VG_{mod}}$ [m]	flow, VG model
3.8	18	1.10	att.	0.80	att.
3.1	18	1.60	att.	1.30	att.
1.4	18	2.00	att.	1.70	att.
1.0	10	2.00	sep.	1.70	sep.

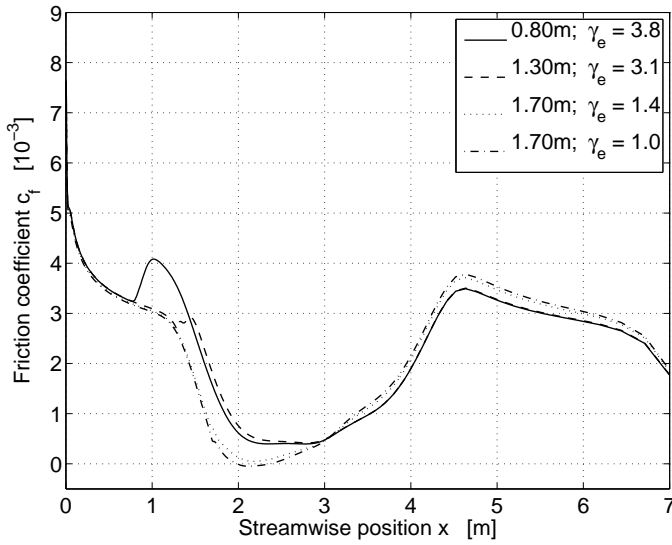


FIGURE 4.7. Local skin friction coefficient distributions for different VG model settings, corresponding to experimental settings; legend left column: streamwise position of the VG model from the flat plate leading edge, legend right column: γ_e according to Lögberg *et al.* (2009), see also table 4.1.

4.3. Internal diffuser flow

The application of the VG model in the KTH diffuser, see figure 4.8, was briefly carried out as a demonstration case for internal APG flow and chosen streamline and turbulent kinetic energy contour plots are shown in figure 4.9.

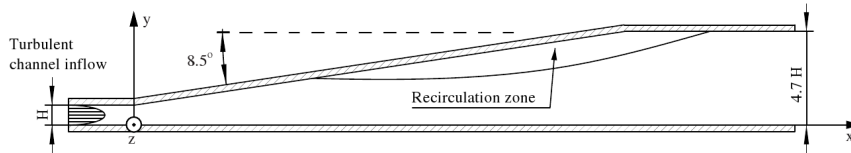


FIGURE 4.8. KTH diffuser geometry, taken from Törnblom (2006).

Chosen settings of the VG model are presented in table 4.2 and in figure 4.9. In comparison with the flow case without VG model in a), the application of the VG model in b) and c) shows a decreased separated region and attached flow, respectively. The differences lie in the streamwise location of the VG model, with VG4 in c) being more upstream located where higher VG blade tip velocities occur than for VG1 further downstream. This leads to a stronger generation of vortex stresses for VG4 and thus, to a better flow separation

control than for VG1. It has to be added that the setting in b) gave attached flow in experiments, showing that the VG model under estimates the effects of the generated vortex structure in terms of the additional vortex stresses. It is also suggested that the nearfield development of the VG model may be the cause for an under estimated effect of the modelled flow control devices as shown here. This fact needs to be further investigated by means of e.g. a more advanced vortex model within the VG model as will be discussed in the remarks and outlook chapter on page 35.

Paper 1 presents this flow case more comprehensive, including further VG model parameter variation studies. In addition, the external flow case around a 2D airfoil with a modified high-lift system is discussed in Paper 1, showing the capabilities of the VG model for such an engineering application.

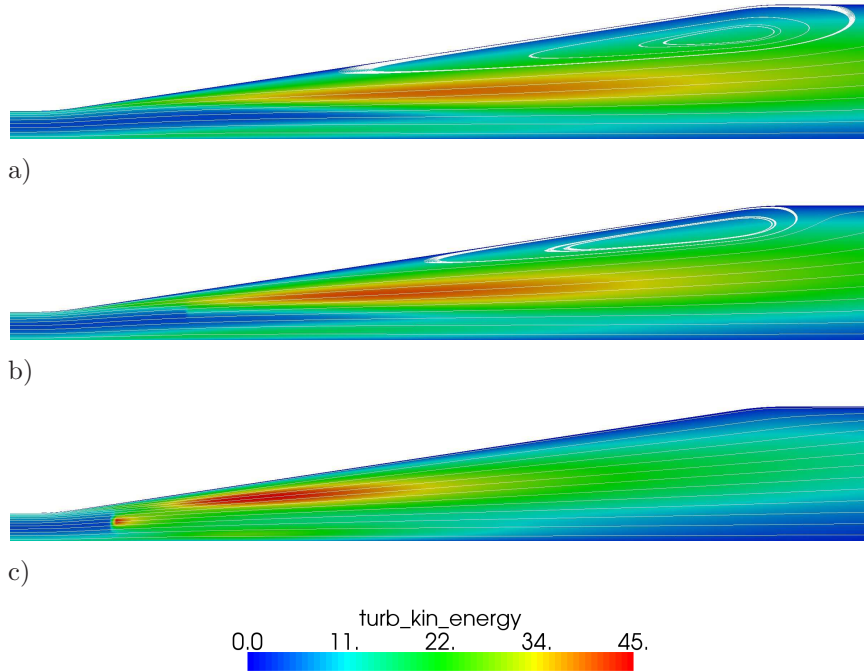


FIGURE 4.9. Turbulent kinetic energy field and streamline plots for: a) no VG model, b) VG1, and c) VG4 setting.

TABLE 4.2. Vortex generator model input variables for the KTH diffuser, $h_{VG,mod}/H = 0.6$, $r_0/h = 0.1$, and $C_\omega = 1$.

	$x_{VG,mod}/H$	K
VG1	4.7	1.8π
VG4	2.0	1.8π

Summary of Papers

5.1. Paper 1

A Vortex Generator Model Applied in Zero and Adverse Pressure Gradient Flow.

This paper presents the application of the vortex generator (VG) model described in chapter 3 for three different flow cases. First, basic studies including the calibration and evaluation of the VG model were carried out on a flat plate in zero pressure gradient flow, compare also with experiments of Lögdberg (2008). The VG model set-up was geometrically similar to the experimental set-up, and a parameter study was carried out for the remaining VG model parameters. Based on a baseline case and its parameters, the lift slope K in the lifting-line theory (LLT), the viscous core radius r_0 in the vortex model, and the turbulent specific dissipation rate ω were investigated independently. It was shown that the lift slope had a rather negligible impact on results whereas the latter two parameters can have an important influence. The limitation of the two-dimensional vortex model was tested by including a case study with spanwise averaged three-dimensional initial conditions from fully resolved computations. This study showed that the vortex model can lead to a significant change in the development of the Reynolds stresses in a defined nearfield. Second, the VG model was investigated qualitatively on the HELIX three-element airfoil short-chord flap. Here, results have shown that the VG model shows sensitivity for different streamwise positions and for shape and height modifications, yet not leading to satisfying quantitative results. In a last part, the VG model could be investigated in internal diffuser flow. Also there, the results show that the VG model under estimates the physical influences on the flow, leading to different modelled geometrical parameters and streamwise positions than in reality.

5.2. Paper 2

Evaluation of a Vortex Generator Model in Adverse Pressure Gradient Boundary Layers.

This paper presents the evaluation of the VG model on a flat plate in adverse pressure gradient (APG) flow, as previously experimentally investigated by Lögdberg (2008). Lögdberg carried out studies including three different APG cases whereas the computational investigation concentrated on the most

comprehensive studied case. The experiences and results from paper 1 concerning the calibration of the VG model were used and applied. Moreover, sensitivity studies of the VG model position upstream of a separation bubble complemented the previous research results. It could be shown by means of skin friction and wall static pressure distribution plots that the VG model shows sensitivity for the streamwise position, leading to a better separation prevention the further upstream the VG model was applied. This originated from the higher VG blade tip velocities in the boundary layer the further upstream the VG model was implemented, therefore generating stronger vortex stresses through the LLT and the vortex model. Yet, the effect of stronger vortex diffusion the further upstream the model was exerted and by that, leading to less influence on the separation region, could not be proven by this investigation. In total, this paper shows that the VG model is successful in qualitatively describing the impact of real passive VGs by means of a statistical modelling approach.

Concluding remarks and outlook

The statistical VG model has been evaluated by means of different flow cases: ZPG flat plate, APG flat plate, APG diffuser flow, and the external flow around the HELIX short-chord airfoil. It could be proven that the VG model describes the influence of such passive flow control devices qualitatively correct. Also, and even though the current vortex model lacks a reasonable component of the streamwise velocity, the VG model predicted the flow for the different cases qualitatively correct. Nevertheless, it could also be shown that the effect of the VG model was in many cases lower than expected, i.e. when compared to corresponding experiments or fully resolved results. As discussed previously in chapter 4.1, the $\overline{u'v'}$ Reynolds stresses are generated through the production term in equation 2.14 that in turn needs some time to develop. This causes also a large variation of the $\overline{u'v'}$ Reynolds stresses in the nearfield, as can be seen in figure 4.1 a). A further development of the VG model seems to be necessary in order to also include a streamwise fluctuation velocity component u' so that (the rather important) additional vortex stresses $\Delta\overline{u'u'}$ and $\Delta\overline{u'v'}$ are forced from the beginning at the VG model location. In the present VG model description, these components are produced through the redistribution and the production terms in the DRSM turbulence model. Test runs of a very simple and ad-hoc forcing of these two stress components have shown that they actually have an important influence on the correct prediction of the flow state.

Another aspect is to have a closer look on the overall mechanism of VGs in the flow, and especially what role they play in the governing equations. The Reynolds averaged boundary layer momentum equation in the streamwise direction reads

$$U_j \frac{\partial U}{\partial x_j} \approx -\frac{1}{\rho} \frac{\partial P}{\partial x} + \frac{\partial}{\partial y}(-\overline{u'v'}), \quad (5.1)$$

and it can be seen that there are two different mechanisms that drive separation. In general, separation is driven by the pressure coefficient on the right-hand side of equation 5.1 that decelerates the velocity through the advection term on the left-hand side. A more energised near-wall flow has a higher mean velocity U in the boundary layer that in turn will resist separation. On the other hand, an increased mixing in the boundary layer also increases the second term on the right hand side, $\frac{\partial}{\partial y}(-\overline{u'v'})$, that will counteract the influence of the pressure

gradient, too. This phenomena takes more time to develop than the aspect of an increased near-wall velocity. Still, it is not clear which one of these two effects is dominating and finally is driving the state of flow separation. This has to be investigated further in detail in the future.

Acknowledgements

I would like to thank my co-supervisor Dr. Stefan Wallin for his guidance, patience, and kindness during the last 2 years and 4 months that I spent working on this thesis at KTH Mechanics. Especially the constructive discussions about many different topics, either within my research field or even within off-topic areas were always very fruitful, enriching, and supporting.

Many special thanks to my main supervisor and "chief-editor" Prof. Arne V. Johansson for his distinguished general and straightforward guidance and opinions, and who always succeeded in revealing the general ideas of my research project, leading to many inspiring ideas and inputs during that time.

Moreover, I highly appreciate the helpful comments of Ola Lögdberg about his experimental work.

Many thanks to my present and past roommates Tobias, Peter, Linus, and Daniel for their talks, discussions, help, and, hopefully, understanding during all the time. I am also grateful to have met Ramis and Alexander who can always make me laugh and smile, not only when sharing a cup of coffee somewhere on the KTH campus.

Furthermore, I would also like to thank the whole research group at FOI for a friendly working atmosphere, and especially Peter Eliasson for his very helpful comments concerning the CFD code Edge and who was always willing to help me whenever I had my questions to him.

Last but not least, I do not want to forget my family who is always there for me even though I am far away from you. Danke!

References

- BALDWIN, B. S. & LOMAX, H. 1978 Thin-layer approximation and algebraic model for separated turbulent flows. *16th Aerospace Sciences Meeting, Huntsville, AL, USA* **1978-0257**.
- BOUSSINESQ, J. 1877 Théorie de l'Écoulement tourbillant. *Memoires Présentés par Divers Savants à l'Académie des Sciences, Institut de France* **23**, 46–50.
- CEBECI, T. & SMITH, A. M. O. 1974 *Analysis of Turbulent Boundary Layers*. New York, USA: Academic Press.
- CHOU, P. Y. 1945 On the velocity correlation and the solution of the equation of turbulent fluctuation. *Quarterly of Applied Mathematics* **3**.
- GATSKI, T. B. & SPEZIALE, C. G. 1993 On explicit algebraic stress models for complex turbulent flows. *Journal of Fluid Mechanics* **254**, 59 – 78.
- GLAUERT, H. 1926 *The Elements of Aerofoil and Airscrew Theory*, 1st edn. Cambridge University Press, London, UK.
- HALLBÄCK, M., JOHANSSON, A. V. & BURDEN, A. D. 1995 The Basics of Turbulence Modelling. *Ercoftac Series, Turbulence and Transition Modelling* **3**, 81 – 154.
- KOLMOGOROV, A. N. 1942 Equations of Turbulent Motion of an Incompressible Fluid. *Izvestiya Akademii Nauk Phys.* **6**, 56 – 58.
- LAUNDER, B. E. & SPALDING, D. B. 1972 Mathematical Models of Turbulence. *Journal of Sound and Vibration* **25** (4).
- LIN, J. C. 2002 Review of research on low-profile vortex generators to control boundary-layer separation. *Progress in Aerospace Sciences* **38**, 389–420.
- LÖGDBERG, O. 2008 Turbulent Boundary Layer and Separation Control. PhD thesis, Department of Mechanics, KTH Stockholm.
- LÖGDBERG, O., FRANSSON, J. H. M. & ALFREDSSON, P. H. 2009 Streamwise Evolution of Longitudinal Vortices in a Turbulent Boundary Layer. *Journal of Fluid Mechanics* **623**, 27–58.
- PAULEY, W. R. & EATON, J. K. 1988 Experimental Study of the Development of Longitudinal Vortex Pairs Embedded in a Turbulent Boundary Layer. *AIAA Journal* **26** (7), 816 – 823.
- PEARCEY, H. H. 1961 *Boundary Layer and Flow Control, its Principles and Applications*. Oxford, UK: Pergamon Press.
- POPE, S. B. 2000 *Turbulent Flows*. Cambridge, UK: Cambridge University Press.
- PRANDTL, L. 1925 Bericht über Untersuchungen zur ausgebildeten Turbulenz. *Zeitschrift für angewandte Mathematik und Mechanik* **5**, 136–139.

- PRANDTL, L. 1945 Über ein neues Formelsystem für die ausgebildete Turbulenz. *Nachrichten der Akademie der Wissenschaften in Göttingen, Math-phys. Kl.* 1945 pp. 6–19.
- RODI, W. 1976 A New Algebraic Relation for Calculating the Reynolds Stresses. *Journal of Applied Mathematics and Mechanics* **56**, T219 – T221.
- SAFFMAN, P. G. 1970 A Model for Inhomogeneous Turbulent Flow. *Proceedings of the Royal Society London A* **317** (1530), 417 – 433.
- SPALART, P. R. & ALLMARES, S. R. 1992 A one-equation turbulence model for aerodynamic flows. *30th AIAA Aerospace Sciences Meeting, Reno, NV, USA* **AIAA 1992-0439**.
- SPEZIALE, C. G., ABID, R. & ANDERSON, E. C. 1990 A Critical Evaluation of Two-Equation Models for Near Wall Turbulence. *21st Plasma Dynamics and Lasers Conference, WA, USA* **AIAA 1990-1481**.
- TÖRNBLOM, O. 2006 Experimental and Computational Studies of Turbulent Separating Internal Flows. PhD thesis, Department of Mechanics, KTH Stockholm.
- TÖRNBLOM, O. & JOHANSSON, A. V. 2007 A Reynolds stress closure description of separation control with vortex generators in a plane asymmetric diffuser. *Physics of Fluids* **19**.
- WALLIN, S. & JOHANSSON, A. V. 2000 An explicit algebraic Reynolds stress model for incompressible and compressible turbulent flows. *Journal of Fluid Mechanics* **403**, 89–132.
- WILCOX, D. C. 1988 Reassessment of the Scale Determining Equation for Advanced Turbulence Models. *AIAA journal* **26** (11), 1299 – 1310.
- WILCOX, D. C. 1993 *Turbulence Modeling for CFD*, 1st edn. DCW Industries, USA.
- YAO, C.-S., LIN, J. C. & ALLAN, B. G. 2002 Flow-Field Measurement of Device-Induced Embedded Streamwise Vortex on a Flat Plate. *1st AIAA Flow Control Conference, St. Louis, MO, USA* **AIAA 2002-3162**.

Part II

Papers

Paper 1

A Vortex Generator Model Applied in Zero and Adverse Pressure Gradient Flow

By Florian von Stillfried, Stefan Wallin, and Arne V. Johansson

Royal Institute of Technology Stockholm
Linné Flow Centre
Department of Mechanics
SE - 100 44 Stockholm, Sweden

Submitted to AIAA Journal

Modeling arrays of passive vortex generator (VG) pairs, mounted in fully turbulent zero pressure gradient (ZPG) and adverse pressure gradient (APG) boundary layers, generating streamwise counter-rotating vortex structures is investigated. Usually, a sound computational fluid dynamics (CFD) investigation requires a fully resolved grid with a corresponding large number of grid points around such VGs in order to obtain an accurate solution. An efficient way to get around this time-consuming process is to introduce a way to model these flow control devices statistically and, by that, to add their statistical physical effects to the averaged governing equations. KTH and FOI, the Swedish Defence Research Agency, have developed a computational tool for statistical VG modeling in wall-bounded flows regarding the Reynolds stresses. In this investigation, velocity and Reynolds stress profiles for fully three dimensional resolved VGs as well as experimental results are evaluated and compared to this statistical VG model approach for a two dimensional ZPG flat plate flow. Furthermore, the model is evaluated for the external flow around a wing profile as well as for internal APG flow in an asymmetric diffuser. It is moreover shown that the VG model qualitatively predicts the influence of VGs on separation in these sensitive flow cases.

1. Introduction

The operational envelope in aeronautical and other engineering designs is in many cases limited by turbulent boundary layer separation. The possibility of controlling and delaying the separation enables more efficient designs that can be used for improving the performance or for optimizing the design in order to reduce drag and weight. Turbulent boundary layers can be energized by introducing vortices by vortex generators (VGs) that increase the mixing of

momentum in the boundary layer and, by that, increase the near-wall velocity. Experimental studies as well as computations have shown the ability of controlling separation with such devices.

It was shown in an experimental study of embedded vortex pairs in a turbulent boundary layer (Pauley & Eaton 1988) how different VG configurations, i.e. co-rotating, counter-rotating ("common flow up/down"), and unequal VG settings have various effects regarding the developing boundary layer thickness, the circulation, and the vorticity downstream of the VGs. Parameter variations like the spacing between VG vanes and the VG angle of incidence α to the main flow showed that more and less optimal configurations exist for momentum mixing. It was e.g. found that common flow down VG pairs and co-rotating arrays with a certain minimum spacing between the vanes provide less decay of vorticity and circulation than common flow up VG settings.

Lin (2002) provides a review of the research activities in the field of passive sub-boundary layer vortex generators (SBVGs). Basic fluid dynamics and applied aerodynamics research of the performance enhancement of various flow cases due to SBVGs is presented. SBVGs are most efficient when flow separation is relatively fixed so that they produce "minimal near-wall protuberances" in order to overcome flow separation. The height of such SBVGs is typically around $0.1 \leq h/\delta_{99} \leq 0.5$ which in turn reduces drag compared to larger VGs but still ensures the SBVGs acting as highly effective control devices against flow separation compared to conventional larger VG designs. Lin (2002) states that the nondimensional geometrical device parameters such as the VG chord to height ratio c/h and the VG pair distance to height ratio D/h are increased substantially when the height h is reduced, leading to different geometrical properties than in classical design guidelines for conventional VGs. At the same time, angles of incidence α should be increased to ensure sufficient vortex strength when SBVGs are used for flow separation control.

A direct comparison of a SBVG with a device height of $h = 0.2 \cdot \delta_{99}$ with a conventional VG ($h \approx \delta_{99}$) at different angles of incidence lead to the conclusion that maximum vorticity increases as the angle of incidence α is increased for the SBVG. In contrast to that, the conventional VG showed reversed tendencies, probably due to stall phenomena (Yao *et al.* 2002). A higher decay of vorticity for the SBVG was also observed, presumably due to the closer proximity of the wall for this case. Nevertheless, a high rate of vorticity decay might have important effects for applications where vortices are no longer desired once the flow is controlled.

In computational fluid dynamics (CFD), the most direct way to mimic VGs is to fully resolve their geometry within the mesh. This leads to very fine mesh spacings in the vicinity of such VG structures in order to resolve the developing boundary layer on the blade surface and vortex structures in its vicinity and further downstream. Thus, fully resolved VGs lead to high computational costs.

Another way to take VGs into account is rather modeling the resulting effects of VGs in a flow field. This approach removes the need to mesh the VG

geometry. Jirásek (2005) describes two types of different models for mimicing VGs: a vortex source model, and a lifting force model. The vortex source model needs a user input such as the initial circulation of the VGs according to the Biot-Savart law. The lifting force model, developed by Bender *et al.* (1999) and generally called BAY model, rather uses the lifting force that is generated by the VGs and estimated by the lifting line theory (LLT), see e.g. Glauert (1926). The lifting force is added to the Navier-Stokes equations and therefore acts directly on the flow and, by that, forms vortices. Jirásek also presents a new so-called jBAY model that is developed from the BAY model. The jBAY model removes some of the shortcomings of the BAY model such as the lack to model the effects of multiple VGs and the difficulty to define the grid points where the model should be applied.

A statistical VG model approach was introduced by Törnblom (2006). This model approach describes the statistical effects of VGs on the flow. Here, the vortex flow field is derived by only taking the geometrical properties of VGs into account, inspired by Wendt (2001). The circulation distribution $\Gamma(y)$ across one VG vane is needed as an input for the VG modeling and is estimated by the LLT. Then, the resulting two-dimensional (2D) cross stream vortex velocity field is added indirectly by means of the second-order statistics of the generated vortex velocity field in a small region through forcing terms in a Reynolds stress transport (RST) model. Furthermore, the drag generation of the modeled VGs is considered by added volume forces in the streamwise component of the momentum equation. An advantage of this method is that no mesh refinement is needed and that the computational costs compare solely with solving the Reynolds averaged Navier-Stokes (RANS) equations, thus, enabling design and optimization of VG settings by CFD.

Lögberg carried out flat plate experiments in the MTL wind tunnel at the Department of Mechanics at KTH Stockholm with VG arrays attached to it (Lögberg 2008; Lögberg *et al.* 2009). Each of the VG pairs consisted of two streamwise diverging blades that were installed within a fully developed turbulent boundary layer flow at angles of incidence $\alpha = \pm 15^\circ$ towards the free stream direction, producing counter-rotating vortices downstream of the VGs. The experiments covered three different VG sizes, straight and yawed VG arrays, zero pressure gradient (ZPG), and adverse pressure gradient (APG) flow. The experimental setup was similar to Österlund (1999) who investigated turbulent boundary layer flow on a clean flat plate in the same wind tunnel. The experiments by Lögberg are used as a first reference and comparison case for the results of the VG model approach that is investigated. Another two evaluation studies for different flows and VG model parameter settings extend this first comprehensive investigation.

The main objective of this work was to carefully examine the VG model approach that statistically describes the effects of the mixing induced by vortices generated by comparable three-dimensional (3D) VG geometries. First, the VG model was applied in a turbulent boundary layer on a flat plate in ZPG

flow (see also von Stillfried *et al.* 2009a). There, the downstream development (up to ca. 150 VG heights) of the generated vortices are compared with detailed experiments and fully resolved RANS computations. Parameter variations of independent input parameters of the VG model were studied. Second, the VG model was investigated in adverse pressure gradient (APG) flow over a short-chord flap of a three-element airfoil. The clean three-element airfoil at takeoff configuration was investigated at a rather high angle of attack α . Next, the 2D statistical VG model was introduced at this angle of attack on the suction side of the short-chord flap. This investigation included a parameter variation study of the modeled VG geometry such as the height, chord and shape plus the location of the VG model plane. Third, the VG model was applied in APG flow in a plane asymmetric diffuser study that was previously computationally and experimentally investigated at KTH Mechanics, see also Törnblom (2006). For this case, the VG model's position and settings were changed in order to study its influence on separation prevention and delay in APG flow.

2. Analytical and numerical methods

The modeling of the VGs in this investigation follows the way suggested by Törnblom & Johansson (2007) who presented a model that requires neither mesh refinements nor 3D computations. In this model approach, the VGs are represented by a vortex source model that uses the lifting line theory (LLT, see e.g. Glauert 1926) in order to estimate the generation of circulation Γ by the VGs. The circulation distribution $\Gamma(y)$ across a wing according to the LLT is given by

$$\Gamma(y) = \frac{K}{2} U(y) c(y) \left[\alpha(y) - \frac{w(y)}{U(y)} \right], \quad (1)$$

where K is the device lift coefficient slope at $\alpha = 0^\circ$ ($K_{max} = 2\pi \text{ rad}^{-1}$ for a thin flat plate¹), $U(y)$ is the local incoming free stream velocity, $c(y)$ the local chord length of the wing, $\alpha(y)$ the local angle of attack, and $w(y)$ the local downwash due to the trailing vortex sheets. The ratio $w(y)/U(y)$ is the local induced angle of attack $\alpha_{ind}(y)$ for small angles α , and the local downwash $w(y)$ reads

$$w(y) = \frac{1}{4\pi} \int_{-h}^h \frac{d\Gamma}{dy'} \frac{1}{y' - y} dy'. \quad (2)$$

Equations (1) and (2) are solved by means of a Fourier series ansatz, see e.g. Anderson (1991). The LLT holds for high aspect ratio (\mathcal{R}) wings in free flight conditions for small angles of attack α far away from obstacles in the flow. By modeling VGs that are mounted on a wall in a boundary layer flow by means of the LLT, some of its assumptions are not valid anymore as a result of:

¹The unit rad^{-1} will generally be neglected when K is mentioned in the rest of this paper

1. a boundary layer velocity profile $U(y)$ instead of a constant free stream velocity U_∞ ,
2. VGs being wings with very low \mathcal{R} ,
3. possible side effects due to the proximity of neighbouring VG blades, i.e. neighbouring vortices,
4. a reasonable high angle of incidence α (corresponding the angle of attack α for free flight in the LLT) of the VG blades.

Therefore, the LLT should be considered as an approximation to estimate the circulation distribution $\Gamma(y)$ across a single VG blade. In turn, the circulation distribution $\Gamma(y)$ quantitatively describes the generated lift, the induced drag and the vortex strength which is again needed as an input for the vortex model. The vortices are then represented by a 2D Lamb-Oseen vortex model with the azimuthal velocity distribution

$$u_\Phi(r) = \frac{\Gamma_{max}}{2\pi r} \left[1 - \exp\left(\frac{-r^2}{r_0^2}\right) \right], \quad (3)$$

where Γ_{max} is the maximum value of the circulation distribution $\Gamma(y)$, determined from the LLT (see Eq. (1)), r_0 the vortex core radius and r the radial coordinate from the vortex center. A limitation of this 2D vortex model is that it lacks a velocity component in the streamwise direction. Besides that, Velte *et al.* (2009) investigated vortex structures experimentally and has proven that passive vortex generators within an angle of incidence range of $\beta = 20^\circ - 40^\circ$ produce vortices with helical structures. These vortex structures can be modeled, using a simplified Batchelor vortex model (Batchelor 1964) for the azimuthal and axial velocity distributions.

VG arrays consist of n VG pairs so that all VG pairs in the array influence the vortex-induced velocity field everywhere in the VG model plane². Due to that, a superposition of the n individual vortex-induced velocity fields $u_\Phi(r)$ from Eq. 3 for each VG blade in the VG model plane is carried out, resulting in the composite vortex velocity field $u'_i(y, z)$ for the complete y-z VG model plane, see Fig. 1. For the statistical approach, $n = 5$ VG pairs are a reasonable choice in order to obtain a converged velocity field around $z = 0$. Moreover, the wall boundary acts approximately as a symmetry condition for the vortices, which is simulated by introducing mirror image vortices, again see Fig. 1. By that, a zero normal velocity $v'(y = 0, z) = 0$ is ensured at the wall.

The concept of this VG model approach and describing its effects on the flow is to assume that the second-order statistics of the additional vortex velocity field act like additional Reynolds stresses on the mean flow. By making this assumption, the additional spanwise averaged contributions $\Delta \overline{u'_i u'_j}(y)$ to

²Throughout this paper, the VG model plane is assumed to be the corresponding yz-plane at the streamwise trailing edge location of the experimental VG blades.

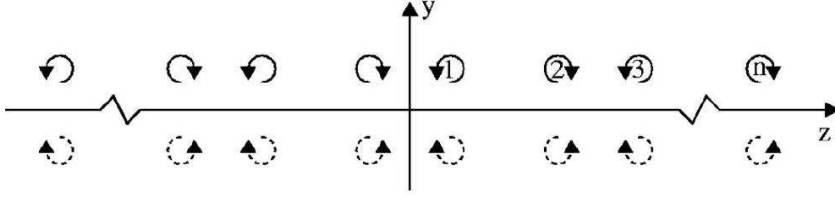


FIGURE 1. Vortex array with n VG pairs and their mirror images for computing the total superpositioned vortex-induced velocity field $u'_i(y, z)$ in the VG model forcing plane, taken from Törnblom & Johansson (2007).

the Reynolds stresses are, see also Törnblom & Johansson (2007) for details,

$$\Delta \overline{u'_i u'_j}(y) = \frac{1}{D} \int_{-D/2}^{D/2} u'_i(y, z) u'_j(y, z) dz. \quad (4)$$

It is sufficient to integrate and spanwise average the second-order statistics in Eq. (4) over one VG pair distance D since the resulting vortex flow field is periodic. Additional contributions from Eq. (4) for a counter-rotating set of VG pairs are only nonzero for $\Delta \overline{v'v'}$ and $\Delta \overline{w'w'}$. Moreover, a wall damping function, e.g. $(1 - \exp(-20y/h))$, needed to be introduced and applied on Eq. (4) because the vortex velocities in the spanwise direction at the wall boundary $y = 0$ will not cancel out and would result in a finite value in Eq. (4).

After applying the additional stresses, a RST turbulence model was used to properly describe the development of the total Reynolds stresses downstream of the VG plane. Furthermore and unlike simpler turbulence models, a RST turbulence model makes it possible to account for the energy transfer between the different components of the Reynolds stress tensor, thus enabling production of $\overline{u'v'}$ Reynolds stresses.

3. Flat plate ZPG flow with VGs

The corresponding geometry of the modeled VGs was earlier experimentally examined by Lögdberg (2008) and Lögdberg *et al.* (2009), see also Fig. 2 and Table 1. Each VG pair consisted of two rectangular flat plates of height $h = 18$ mm, mounted at angles of incidence $\alpha = \pm 15^\circ$, and a chord length $c/\cos \alpha$ with $c = 54$ mm being the projected chord in the streamwise direction. The mean distance between two VG blades was $d = 37.5$ mm and the distance between two adjacent VG pairs was $D = 150$ mm. The VGs were mounted in an array consisting of $N = 5$ VG pairs on a flat plate in a fully developed turbulent boundary layer at a free stream velocity $U_\infty = 26.5$ m/s in the test section of the MTL wind tunnel at KTH Stockholm.

The VG model computations were solved by means of an in-house boundary layer solver code, see Wallin & Mårtensson (2003), using central differences for spatial derivatives and Euler backward differences for time derivatives. The

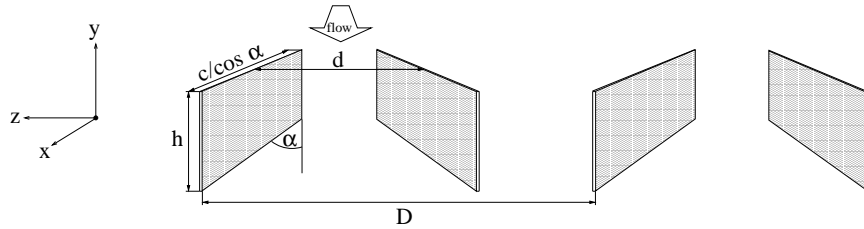


FIGURE 2. Counter-rotating "common flow down" vortex generator pairs in a counter-rotating setting and their notation.

TABLE 1. Vortex generator geometry data from experiments.

h [mm]	d [mm]	D [mm]	c [mm]	α [°]
18	37.5	150	54	± 15

system of equations, written in symbolic form, is processed and discretized using MapleTM procedures. Fortran code and subroutines are generated and compiled automatically to construct the boundary layer code including boundary conditions. The code makes it possible to use very fine resolution at low computational costs.

ZPG clean flat plate boundary layer computations without any VG model applied were carried out in order to determine the correct VG plane position for the VG model computations matching the experimental boundary layer properties. The boundary layer displacement and momentum thicknesses at the VG trailing edge in experiments were $\delta^* = 4.71$ mm and $\theta = 3.38$ mm, respectively. Similar flow conditions in experiments were present further upstream than for the computations, i.e. at $x_{VG,mod} = 1.83$ m compared to $x_{VG,exp} = 2.00$ m downstream of the flat plate leading edge. This difference is a result of wind tunnel flow conditions with forced turbulent tripping of the boundary layer upstream of the VGs. Thus, the VG model had to be applied further downstream in order to match the correct streamwise position within the turbulent boundary layer. This shifting ensured $Re_\theta = 6000$ as suggested by Österlund (1999).

In addition, CFD calculations of the same flow case, yet including fully resolved 3D VGs, were carried out with the Edge CFD code, a general purpose CFD code see Eliasson (2002). These results were used to compare the VG model approach with fully resolved results. The computational domain fully resolved the VGs, see Fig. 3, assuming a no-slip condition on the flat plate as well as on the VG blades. The value for the first grid point at the wall was set to $y = 10^{-5}$ m throughout the domain, giving values of $y^+ = \mathcal{O}(1)$. Furthermore, symmetry conditions were applied so that the computational domain was reduced to only one VG blade. The computational mesh was kept fine in the vicinity of the VGs by means of an O-grid topology.

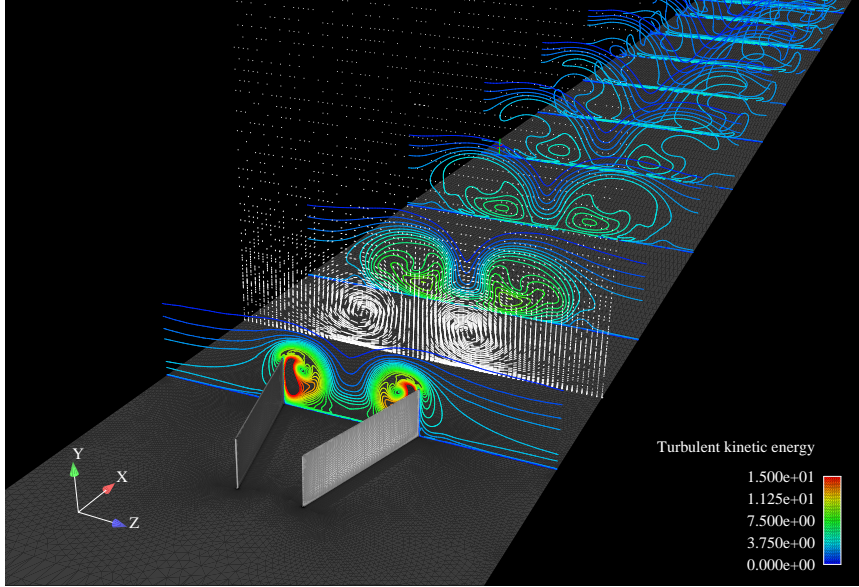


FIGURE 3. CFD plot of one resolved vortex generator pair (symmetry conditions applied) including downstream developing turbulent kinetic energy contours and one yz -velocity plot at one vortex generator height h downstream of the vortex generator trailing edge plane.

3.1. Baseline setting

The baseline investigation included a variation of the independent parameters in the statistical VG modeling approach. Three different parameters were found to be independent and the baseline reference values for the three different independent parameters K , r_0 , and C_ω were set according to Table 2.

TABLE 2. Baseline setting for K , r_0 , and C_ω .

K	r_0/h	C_ω
2π	0.1	1

K and r_0 are the lift slope and the viscous core radius (see Eqs. 1 and 3), respectively, and C_ω a constant to account for the change in the turbulent specific dissipation rate ω due to the imposed vortices at the VG plane. C_ω is defined as $C_\omega = \omega_{out}/\omega_{in}$, it multiplies therefore the result for the computed ω_{in} at the VG plane and uses the multiplied value as a new inflow condition ω_{out} for the calculations with the VG model. For a rough estimate and a first investigation, ω_{in} was assumed to stay constant over the VG plane, i.e. $C_\omega = 1$. The value of the lift slope $K = 2\pi$ is found in many papers in literature and represents the maximum theoretical value of the lift slope for a flat plate in

free flight conditions. A viscous core radius of the vortex model of $r_0/h = 0.1$ was previously investigated by Törnblom (2006) for VGs in diffuser flow.

Figure 4 shows the results of the four Reynolds stress components for the turbulent flat plate boundary layer without VGs and Fig. 5 gives the additional vortex stresses from the VG model at the VG model plane. The superposition of both stress distributions gives the initial inflow boundary conditions for the VG model approach computations when VGs are applied. The vortex structure in the stress distribution is clearly seen in Fig. 5 whereas a comparison of Figs. 4 and 5 shows that the turbulent boundary layer Reynolds stresses are approximately one order smaller than the vortex stresses.

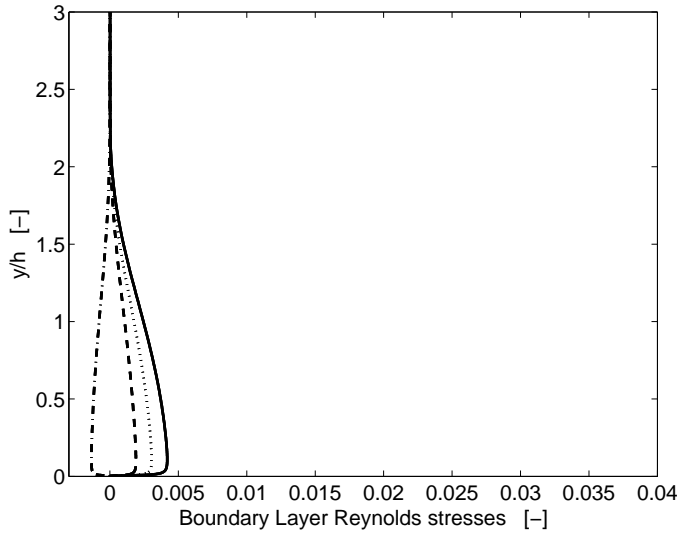


FIGURE 4. Wall-normal $\overline{u'v'}$ (---), $\overline{u'u'}$ (-), $\overline{v'v'}$ (- · -), and $\overline{w'w'}$ (··) boundary layer Reynolds stress distributions without vortex generator at the vortex generator plane, nondimensionalised with U_∞^2 .

Experimental results for a comparison with the VG model computations were available for the farfield planes at $x/h = 3.3, 9.4, 23, 37, 65, 93,$ and 148 downstream of the VG plane. Furthermore, fully resolved results were available for both the nearfield and the farfield. The experimental data and the fully resolved data represent the time averaged data of the 3D flow field and had to be post processed for comparison with the VG model computations in terms of a velocity decomposition and a spanwise averaging of the velocities and the second-order statistics. By doing that, cross correlations between vortices and turbulence were neglected corresponding to the case where the vortex velocities are totally uncorrelated to the turbulent stresses from the boundary layer

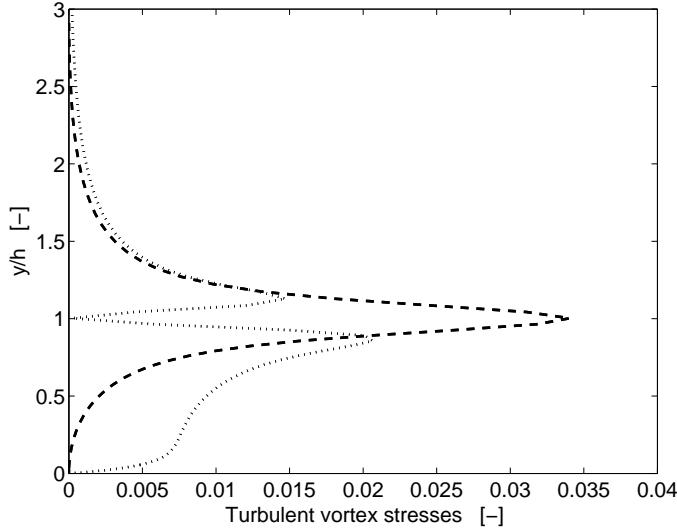


FIGURE 5. Additional wall-normal $\Delta\overline{v'v'}$ (--) and $\Delta\overline{w'w'}$ (··) Reynolds stress distributions from the vortex generator model at the vortex generator plane, nondimensionalised with U_∞^2 .

flow. At this state, it is not possible to determine whether this is a reasonable approximation or not since the experimental cross correlations of vortex velocities and turbulent stresses could neither be post processed quantitatively nor qualitatively from the given data. All fully resolved computations were solved by means of the Wallin & Johansson explicit algebraic Reynolds stress turbulence model (EARSM) (Wallin & Johansson 2000) together with the $k-\omega$ turbulence model by Hellsten (Hellsten 2005). The 2D boundary layer solver calculations are solved with a full differential Reynolds stress turbulence model (DRSM), corresponding to the Wallin & Johansson EARSM turbulence model with curvature correction (Wallin & Johansson 2002) together with the Hellsten $k-\omega$ turbulence model. In general, the DRSM modeling approach adds the additional vortex stresses $\Delta\overline{v'v'}$ and $\Delta\overline{w'w'}$ to the Reynolds stress tensor whereas the EARSM approach accounts for a corresponding kinetic energy that is in turn added to the turbulent kinetic energy k . Therefore, the individual transport terms of the Reynolds stress components are not taken into account for the EARSM modeling. Nevertheless, the two models are compared in this study and differences in results are presented in the following figures.

Figure 6 a) shows the mean velocity profile development $U(y)/U_\infty$ for the nearfield planes at $x/h = 0.0, 0.5, 1.1, 1.7, 2.2,$ and 2.8 downstream of the VG plane. One can see that the fully resolved and the VG model approach velocity profiles collapse well, except for the velocity deficit around $y/h = 1$. This defect evolves from resolving the VG vanes, which in turn introduces a momentum loss in the flow, resulting in a velocity defect in the mean velocity

profile. Since the 2D Lamb-Oseen vortex model does not take any streamwise velocity defect into account, it is also not computed by the boundary layer solver. It is observable that the fully resolved velocity defect is smeared with increasing downstream distance.

The farfield velocity profiles at $x/h = 3.3, 9.4, 23, 37, 65, 93,$ and 148 in Fig. 6 b) show that the velocity profiles from fully resolved computations are very consistent with the experimental profiles, also for the last two positions for which the experiments clearly show an increase in velocity in the vicinity of the wall up to $y/h \approx 4$. Moreover, the experimental and fully resolved plots clearly indicate a momentum transfer from the high energy containing free stream into the boundary layer and vice versa. The velocity defect is very local around $y/h = 1$ for the first plots and is constantly diffused and transported outwards whereas an increase in velocity takes place for lower y/h . This mechanism is directly connected to the vortices in the flow that permanently transport low energy flow to higher y/h and, in turn, feed the near-wall flow with high energy flow. This interaction can also be seen for fully resolved data plots but the increase in velocity seems to occur slower than for the experiments. Still, resolving the VG vanes predicts the real flow quite well up to $x/h = 93$. After that, the velocity profiles do not collapse for $y/h > 1$ and momentum transfer does not seem to be captured anymore, probably due to a too diffused computed vortex.

Even though the VG model forces $\overline{v'v'}$ and $\overline{w'w'}$ Reynolds stresses, and while the boundary layer solver takes all four corresponding Reynolds stress terms into account, the remaining part of this paper concentrates on the $\overline{u'v'}$ Reynolds stresses since these stresses have the largest influence on the mean flow of a thin attached turbulent boundary layer.

The plots in Fig. 6 c) show the nearfield development of the $\overline{u'v'}$ Reynolds stresses at $x/h = 0.0, 0.5, 1.1, 1.7, 2.2,$ and 2.8 . The left plot at the VG position shows the initial stresses that act on the mean flow. The solid data curve still shows the results from the flat plate from the boundary solver computations, since $\overline{u'v'}$ stresses were not forced by the VG model and thus, remain as they initially are, see also Fig. 4. In contrast to that, and significantly different are the $\overline{u'v'}$ stresses from fully resolved calculations, dashed lines in Fig. 6 c). One can observe a distinct absolute minimum around $y/h = 0.5$ and one smaller local minimum at $y/h \approx 1$. Even though the initial $\overline{u'v'}$ profiles are certainly totally different, they tend to approach each other further downstream, almost collapsing for the right plot at $x/h = 2.8$ in Fig. 6 c). In between, two very small peaks develop for the VG model computations, being consistent with the fully resolved results that disappear again further downstream.

It can be observed that the farfield $\overline{u'v'}$ Reynolds stresses in Fig. 6 d) from the experiments are initially very similar to the other two calculated data curves. The slopes and the orders of magnitude of the boundary layer solver data is promising especially by keeping in mind that the $\overline{u'v'}$ component of the additional vortex stresses was not initially forced by the VG model at the VG

plane. The trends for further downstream positions are again consistent even though the boundary layer solver tends to underpredict results from $x/h = 23$ compared to the other curves. The reason for this is that the vortex stresses are now included in the turbulent stresses that decay much faster than the fully resolved vortex structures and the experimental vortices that are naturally preserved longer. It is furthermore generally seen that the stresses are transported to higher y/h for increasing streamwise positions.

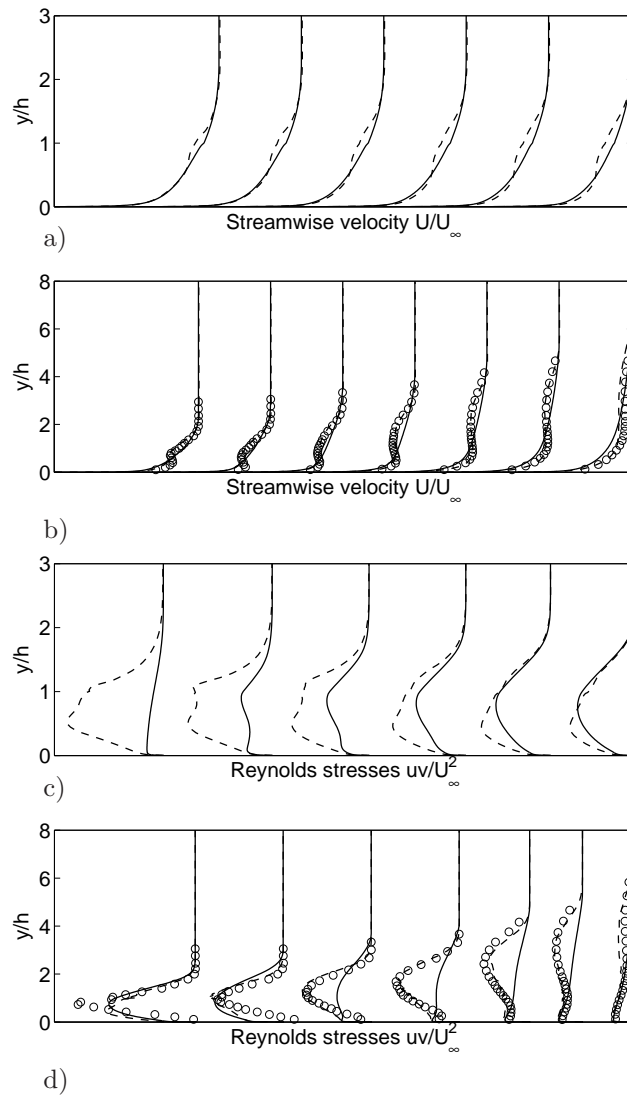


FIGURE 6. Vortex generator model (—), spanwise averaged fully resolved (---), and spanwise averaged experimental (o, only b) and d)) nondimensional wall-normal mean velocity profiles $U(y)/U_\infty$ (left) and nondimensional wall-normal $\overline{u'v'}/U_\infty^2$ Reynolds stress distributions (right) at streamwise positions x/h downstream of the vortex generator plane: a) and c) nearfield $x/h = 0.0, 0.5, 1.1, 1.7, 2.2,$ and 2.8 ; b) and d) farfield $x/h = 3.3, 9.4, 23, 37, 65, 93,$ and 148 (from left to right).

3.2. Parameter variations

A calibration of the VG model through K and r_0 as well as an adjustment of the turbulent specific dissipation rate ω through C_ω over the VG plane, see also Table 2 for the baseline setting, might lead to better results. Therefore, calculations were carried out to investigate the influence of the three independent parameters. Table 3 gives an overview of the different values that were investigated. All remaining constants for each parameter variation were set to the original reference values, see also Table 2. Main focus for the choice of values was to carry out computations for one higher as well as one lower value. The inflow conditions from the turbulent boundary layer without VGs are initially the same for all three parameter variations, just as for the baseline case. Depending on the parameter investigated, the further development of the Reynolds stresses distributions is strongly or weakly influenced.

TABLE 3. Parameter settings for K , r_0 , and C_ω .

K	1	2π	10
r_0/h	0.05	0.1	0.2
C_ω	0.1	1	10

3.2.1. VG model parameters K and r_0

Mean velocity plots of the K -variation are given in Fig. 7 a) - b). It is visible in a) that the nearfield velocities almost collapse with each other. This is expected as the mean flow velocity is not rapidly influenced by the additional vortex stresses that act on the mean flow through turbulent stresses. Fig. 7 b) shows that the mean velocities are very slightly changed, giving a change for the lowest value $K = 1$. There, the vortex is not as strong as for the other K -values and therefore, redistribution of the streamwise velocity component is less. This leads to higher streamwise velocities closer to the wall and lower velocities away from the wall for the higher K -values. A comparison to experimental data in the farfield in Fig. 7 b) shows that the velocity defect and the redistribution of the mean flow is much more distinct for the experiments than for the computations, giving a local minimum around $y/h = 1$ for the first position.

The resulting $\overline{u'v'}$ plots for the K -variation are given in Fig. 7 c) - d) and clearly show that an increase in K increases the Reynolds stresses along the whole range of y/h . In return, a decrease in K leads to the opposite result. Therefore, K influences the $\overline{u'v'}$ stress distribution over the whole y -range within the boundary layer. One can also observe that an increase in K only results in a saturated increase of the stresses, leading to less growth as K is increased. This effect can be explained by the fact that even though the circulation theoretically tends towards infinity when K attains infinitely large values, the counteracting induced downwash from the VG model has a cancelling effect. Mathematically, Eqs. (1) and (2) give the explanation for

this: a higher circulation also entails a higher downwash $w(y)$ which in turn diminishes the circulation distribution $\Gamma(y)$ and thus, Γ_{max} . This again limits the vortex generation and, by that, restrains the creation of infinitely growing vortex stresses. The growing $\overline{u'v'}$ Reynolds stresses in the nearfield can be explained by the corresponding turbulence production for $\overline{u'v'}$. The turbulence decay is visible in the farfield plots, while keeping the relative allocation between the different $\overline{u'v'}$ Reynolds stress curves.

For the viscous core radius investigations, the baseline value was set to $r_0/h = 0.1$ corresponding to the calculations in Ch. 3.1. In the LLT in Eq. (1), r_0 indirectly determines the maximum value Γ_{max} of the circulation $\Gamma(y)$ around one VG vane. This parameter therefore influences the strength of the imposed vortices by the linear dependence of the azimuthal velocity $u_\Phi(r)$ on Γ_{max} , see Eq. (3). Fig. 8 a) - b) shows the nearfield and farfield velocity plots for the vortex core radius r_0 -variation, respectively. The plots are similar to the ones in Fig. 7 a) - b), giving no major changes during a parameter variation. A conclusion from this is that the VG model parameters K and r_0 do not have a large impact on the mean streamwise velocity, being consistent with the fact that the 2D vortex model itself does not account for a velocity defect.

The result plots for $\overline{u'v'}$ can be examined in Fig. 8 c) - d) that shows that r_0 acts initially more locally on the $\overline{u'v'}$ Reynolds stresses around the vortex core. A higher r_0 gives lower stresses and vice versa. Therefore, the parameter r_0 can easily be used for adjusting the initial vortex strength and the very nearfield local distribution around $y/h = 1$. The decay of the Reynolds stresses in the farfield results again from including the vortex stresses in the turbulent stresses and, by that, cannot be largely influenced by changing r_0 . Nevertheless, the chosen value of $r_0/h = 0.1$ seems to be a reasonable assumption for calculations.

3.2.2. Turbulent specific dissipation rate ω

The baseline assumption was to keep the turbulent specific dissipation rate, or inverse time scale of the turbulence $\omega = \tau^{-1}$, constant over the VG model plane. However, the kinetic energy changes over the VG model plane and it is not clear how a time scale or a length scale will change accordingly. For investigating the sensitivity, the ratio $C_\omega = \omega_{out}/\omega_{in}$ thus represents the constant change in ω across the VG plane. Three different values were chosen for this study: $C_\omega = 1$ from the baseline case, $C_\omega = 0.1$, and $C_\omega = 10$.

Velocity plots for the ω -variation are given in Fig. 9 a) - b). The velocity profiles in a) diverge quicker in the vicinity of the wall than for the other parameter variations. The differences grow in b) and here, compared to the other ω -values, major differences occur for the highest turbulent specific dissipation rate $C_{\omega=10}$, describing a lower near-wall velocity and a higher streamwise velocity further away from the wall. This describes a lower mixing of momentum in the boundary layer which is supported by the plots in Fig. 9 c) and d) where the solid line plots show significant differences in magnitude compared with the other $\overline{u'v'}$ turbulent stresses. For the variation of parameters, the curves are

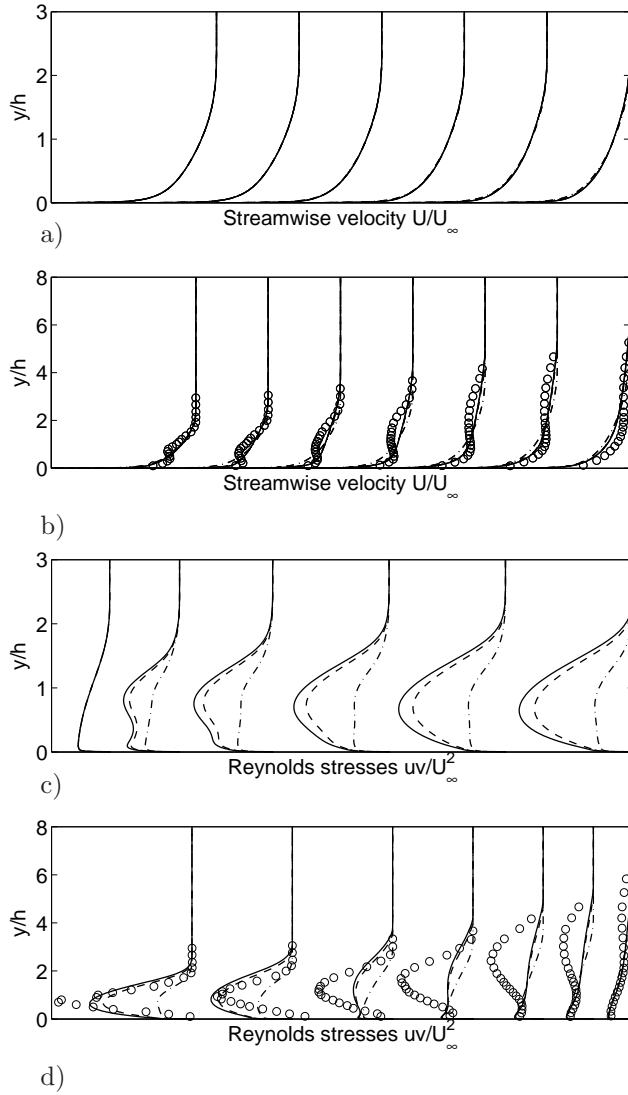


FIGURE 7. Nondimensional wall-normal mean velocity profiles $U(y)/U_\infty$ (left) and nondimensional wall-normal $\overline{u'v'}/U_\infty^2$ Reynolds stress distributions (right) for vortex generator model parameter $K = 10$ (—), 2π (---), 1 (-.-), and experiments (\circ , only b) and d)) at streamwise positions x/h downstream of the vortex generator plane: a) and c) nearfield $x/h = 0.0, 0.5, 1.1, 1.7, 2.2,$ and 2.8 ; b) and d) farfield $x/h = 3.3, 9.4, 23, 37, 65, 93,$ and 148 (from left to right); $C_\omega = 1, r_0/h = 0.1$.

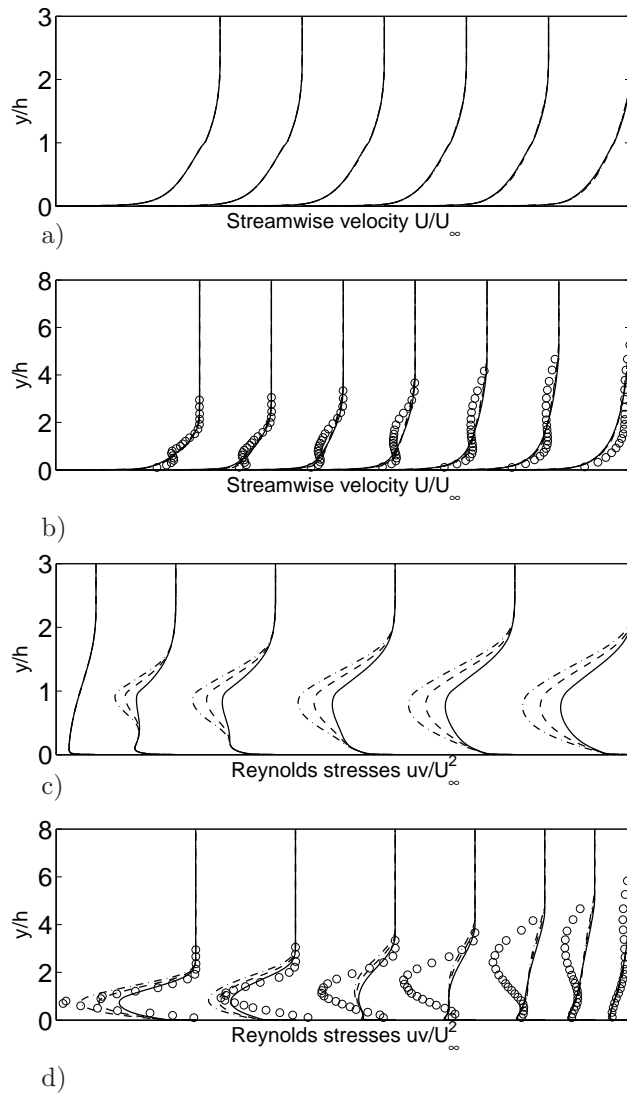


FIGURE 8. Nondimensional wall-normal mean velocity profiles $U(y)/U_\infty$ (left) and nondimensional wall-normal $\overline{u'v'}/U_\infty^2$ Reynolds stress distributions (right) for vortex generator model parameter $r_0/h = 0.2$ (—), 0.1 (---), 0.05 (-.-), and experiments (\circ , only b) and d)) at streamwise positions x/h downstream of the vortex generator plane: a) and c) nearfield $x/h = 0.0, 0.5, 1.1, 1.7, 2.2, \text{ and } 2.8$; b) and d) farfield $x/h = 3.3, 9.4, 23, 37, 65, 93, \text{ and } 148$ (from left to right); $K = 2\pi, C_\omega = 1$.

not simply scaled but even shapes are changed. By setting $C_\omega = 10$, a more damped $\overline{u'v'}$ distribution close to the wall is achieved with a distinctive peak in the nearfield planes close to the vortex core, see Fig. 9 c). On the other hand, $C_\omega = 0.1$ gives higher stresses closer to the wall but information about the vortex stresses that are added by the VG model is lost. In between, the reference case $C_\omega = 1$ describes higher stresses towards the wall but gives simultaneously a distinctive peak at the vortex core position. In the farfield plots in Fig. 9 d), the situation is similar but a closer inspection is provided. The distributions for the two lower C_ω values lie within the same order of magnitude, whereas the $C_\omega = 10$ curve is already significantly smaller. Further downstream, all curves including the experimental curve are damped and the Reynolds stresses are redistributed over y/h , giving local maxima at growing positions $y/h > 1$ for growing x/h positions. Moreover, and as expected, it is visible that $C_\omega = 10$ gives the highest turbulence decay and the distributive effect, especially far downstream, is much less than for the remaining two values. On the other side, $C_\omega = 0.1$ provides the lowest dissipation rate and gives higher Reynolds stresses further away from the wall, even far downstream. In general, one can see that the additional vortex stresses are much quicker damped than the experimental stresses. This is again a direct consequence of the modeling and the naturally longer lasting preservation of vortices in the experiments.

In summary, all parameters influence the development of the Reynolds stresses distributions in both, the nearfield and the farfield. The effects of these variations are visible in the nearfield planes whereas turbulence decay and redistribution has a large impact on the farfield distributions. As can be seen from Figs. 7 - 9, the different parameters act very differently on the development of the Reynolds stresses. The potential to create a more optimal combination of all parameters for better boundary layer solver results is given through these parameters but, unfortunately, no experimental data were available for a closer inspection and a better VG model calibration in the nearfield. Irrespective of the examined parameter variation, the farfield stresses for $x/h > 9.4$ are generally much more diffused by the turbulence than the experimental vortex structures. Therefore, the influence of the parameters and the differences in results in the farfield is not very meaningful for a better choice of a calibration of these parameters. On the other hand, VGs should nevertheless be placed not too far away from the interested region where they should have an effect on the flow and thus, the difference in results is not as significant as it probably seems. In total, the baseline parameter combination seems to represent a reasonable choice for the VG model computations.

3.3. Test case: spanwise averaged fully resolved results as imposed initial boundary conditions for the VG model

In order to investigate the capabilities of the limited VG model approach using the LLT and a vortex model, it was decided to use spanwise averaged results from 3D fully resolved computations as initial input conditions at the VG model

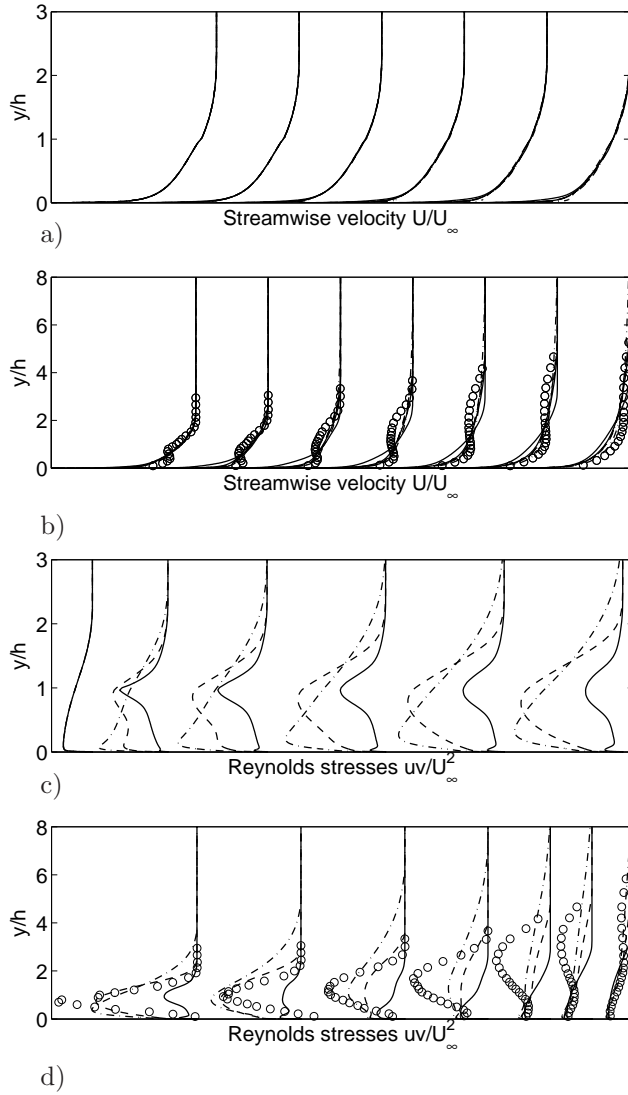


FIGURE 9. Nondimensional wall-normal mean velocity profiles $U(y)/U_\infty$ (left) and nondimensional wall-normal $\overline{u'v'}/U_\infty^2$ Reynolds stress distributions (right) for vortex generator model parameter $C_\omega = 10$ (-), 1 (- -), 0.1 (-·-), and experiments (\circ , only b) and d)) at streamwise positions x/h downstream of the vortex generator plane: a) and c) nearfield $x/h = 0.0, 0.5, 1.1, 1.7, 2.2, 2.8$; b) and d) farfield $x/h = 3.3, 9.4, 23, 37, 65, 93, 148$ (from left to right); $K = 2\pi, r_0/h = 0.1$.

plane. Consequently, no VG modeling by the application of the LLT and the vortex model was needed. Therefore, this procedure replaced the additional VG model input stresses with spanwise averaged Reynolds stresses from fully resolved data. In addition, the velocity distribution was replaced at the VG model forcing plane, now also including a distinct velocity defect that results from the VG vane geometry. The Reynolds stresses at the VG model location are plotted in Fig. 10 and it can be seen that the new initial conditions contain additional $\overline{u'u'}$ and $\overline{u'v'}$ Reynolds stresses that in turn were not modeled by the VG model, compare also with Fig. 5. It can be observed in Fig. 5 that the $\overline{v'v'}$ and $\overline{w'w'}$ Reynolds stresses qualitatively compare very well to the corresponding distributions in Fig. 10, yet including also the (comparably small) boundary layer stresses here. Quantitatively, the distributions are very promising for the VG model, giving stress amounts of approximately the same size as computed for the fully resolved case.

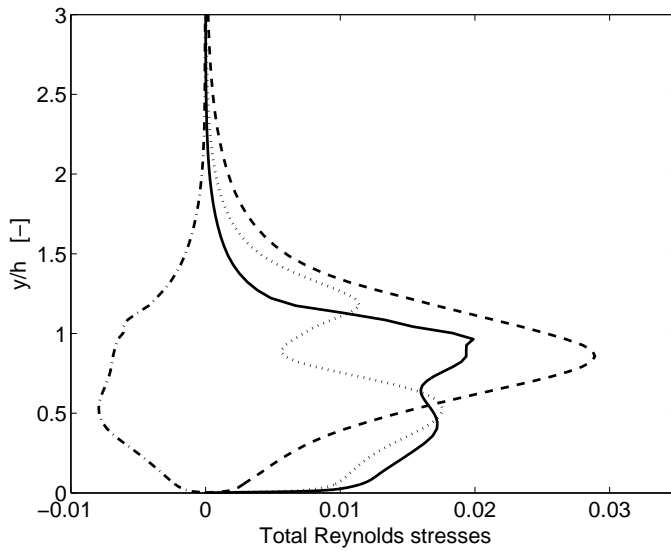


FIGURE 10. Nondimensional wall-normal $\overline{u'v'}/U_\infty^2$ (---), $\overline{u'u'}/U_\infty^2$ (-), $\overline{v'v'}/U_\infty^2$ (- -), and $\overline{w'w'}/U_\infty^2$ (· ·) Reynolds stress distributions from spanwise averaged fully resolved computations at the vortex generator model plane.

Fig. 11 a) - b) present the normalized velocity distributions of the nearfield and the farfield regions, respectively. Here, the first velocity profiles collapse, as expected, and describe very similar evolutions further downstream in the nearfield. The velocity defect in the nearfield is clearly seen, in contrast to the VG model results in Fig. 6 a). Further downstream in the farfield in Fig 11 b), the velocity profiles lose this characteristic, the velocity defect of the statistical

approach diffuses with increasing downstream distance. The fully resolved and the new computations are still similar but results start to deviate for $x/h \geq 9.4$.

$\overline{u'v'}$ Reynolds stresses for the nearfield and the farfield regions are presented in Fig. 11 c) and d), respectively. Also here, the first plots in the nearfield region are congruent with each other. The results using the VG modeling approach with imposed boundary conditions are initially, as expected, much fuller than the original ones from Fig. 6 c). Now resolving for the vortex structures, $\overline{u'v'}$ Reynolds stresses include the effects of the vortices, clearly visible by the peak around $y/h \approx 0.5$. The modeling computations for $\overline{u'v'}$ generally produce very satisfying results up to $x/h \approx 9.4$ from where they get comparable with the plots in Fig. 6 d). The effects leading to this phenomena are the same: turbulence diffusion does not preserve the stresses as if the structures were resolved, giving rise to a longer lifetime of the computed vortex, compare also with Ch. 3.1.

In total, and as a conclusion of this test case, it can be said that the VG modeling has its limitations when compared to real, yet spanwise averaged structures of a vortex. The modification and improvement of the boundary conditions by imposed fully resolved and spanwise averaged results has shown an important impact on the nearfield stress distributions, here given by means of the $\overline{u'v'}$ Reynolds stresses. However, it can be observed that this information is more or less lost further downstream for streamwise positions $x/h \geq 23$. Nevertheless, this investigation has shown that imposed initial conditions, originally from fully resolved computations, do not perform much better or worse than pure VG model results in the region between $x/h \approx 2.2 - 9.4$. In addition, it must be stated that this distance from the forcing region is often the region of interest when it comes to practical applications of flow control with passive vortex generators vanes.

4. Flow around the short-chord flap of the HELIX three-element airfoil

A next step for the evaluation of the statistical VG model was to expand the fundamental research to a high-lift design application. The main objective of this investigation was to examine the capabilities of the statistical VG model in APG flow over a short-chord flap of a three-element airfoil. The clean three-element airfoil at takeoff configuration was investigated at a high angle of attack α . Second, the VG model was introduced at this angle of attack on the suction side of the short-chord flap. This investigation included a parameter variation study of the modeled geometry such as the VG height, chord and shape plus the position of the VG model plane.

In general, VGs have shown to successfully increase the performance of airfoils with and without high lift systems by means of increased lift and decreased drag (Lin *et al.* 1994; Lin 1999; Bragg & Gregorek 1987; Rae *et al.* 2002). Results have shown that counter-rotating and co-rotating set-ups were effective for flow control on a flap and that separation diminishment highly

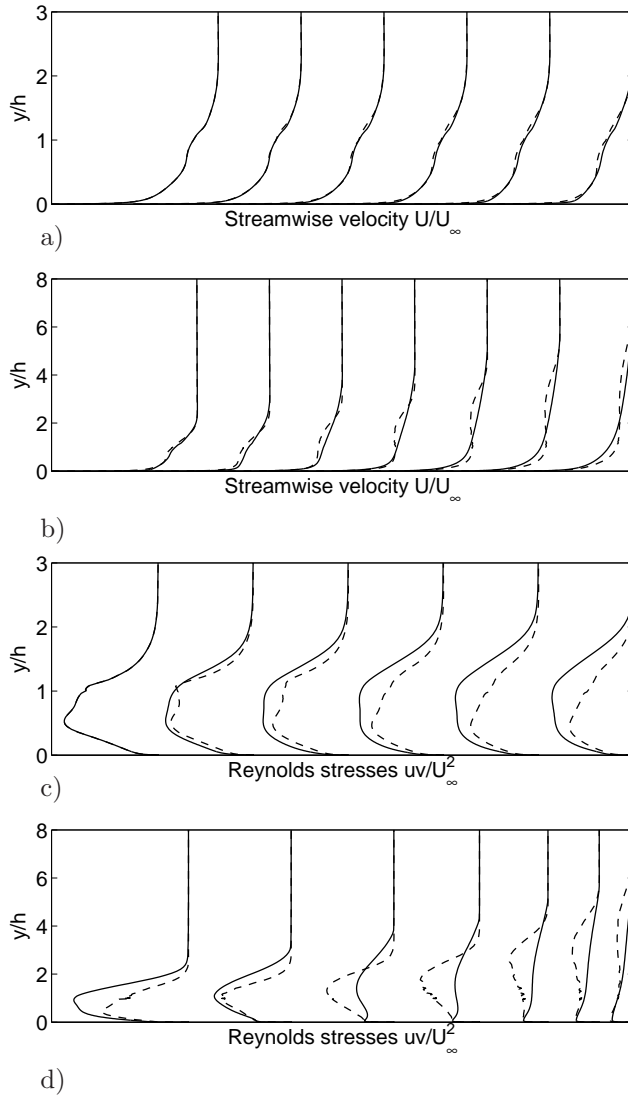


FIGURE 11. Vortex generator model with spanwise averaged fully resolved initial conditions (—), and spanwise averaged fully resolved (---) nondimensional wall-normal mean velocity profiles $U(y)/U_\infty$ (left) and nondimensional wall-normal $\overline{u'v'}/U_\infty^2$ Reynolds stress distributions (right) at streamwise positions x/h downstream of the vortex generator plane: a) and c) nearfield $x/h = 0.0, 0.5, 1.1, 1.7, 2.2,$ and 2.8 ; b) and d) farfield $x/h = 3.3, 9.4, 23, 37, 65, 93,$ and 148 (from left to right).

improved performance at landing and takeoff conditions. Important to note is that additional flow separation devices did not harm the maximum lift or performance enhancement when flow around the flap is attached at very high angles of attack α (Lin *et al.* 1994) when separation is unlikely to occur. Rae *et al.* (2002) found out that an application of SBVGs has an impact on optimal settings of the flap, reducing the sensitivity of the flap performance to gap setting. An optimum chordwise position on the flap should also include the fact that VGs will contribute with drag under cruise conditions if VGs cannot be hidden under the main element. Lift-to-drag polars were moreover unaffected by the presence of SBVGs, having negligible effect during takeoff conditions (Rae *et al.* 2002).

Civil transport aircraft high-lift systems often imply a conventional flap design with 30% chord of the nested wing. Within the HELIX (Innovative aerodynamic high lift concepts) project of the Fifth framework programme by the European Commission (2001-2005), the main goal was to reduce such flap designs to 20% chord and less, therefore providing e.g. the advantage of less cruise drag, smaller actuators and increased fuel capacity. The major challenge for a short-chord flap airfoil to overcome is the higher flap deflection angle during takeoff and landing phases in order to maintain the same amount of lift as for an airfoil with conventional flap size. Flow control devices such as stationary passive VGs that are mounted on such a short-chord flap can alleviate or even totally avoid flow separation at high deflection angles.

4.1. Experimental setup

In a previous study within the HELIX project, various short-chord flap designs with different shroud lengths were investigated. Finally, the short-chord flap design in Figure 12 was chosen for continuative studies. The objective was to experimentally substantiate the performance predictions from previous studies, in particular since the performance enhancement by flow separation control devices was estimated by means of earlier experiences with SBVGs for separation control.



FIGURE 12. The HELIX short-chord three-element airfoil geometry.

Experiments including a conventional three-element airfoil with a standard chord length (baseline) and the new airfoil geometry with a 20% short-chord flap were carried out at VZLU, the Czech Institute of Aviation. An open jet, closed-return, low-speed wind tunnel was used and 2D end-plate models of the baseline and the short-chord geometries were manufactured. These models

allowed a variation in slat and flap deflections as well as a variation of flap lap and flap gap positions relative to the main element. Both, the baseline and the short-chord flap configuration were optimized in terms of the flap lap and gap position.

Generally, the investigations encompassed a full α range and surface pressure measurements were made for 13 baseline and 7 short-chord flap configurations by means of 128 pressure holes. The Reynolds number for all experiments was $Re = 1.65 \cdot 10^6$ based on the undeployed baseline chord c_{base} and the freestream Mach number was $M_\infty = 0.13$.

In particular, the short-chord flap flow control experiments for the takeoff and landing configurations were carried out with delta shape vane-type SBVGs attached at 25% flap chord c_{flap} in a co-rotating configuration with a height $h_{VG,exp}$, a chord $c_{VG,exp}$, positioned with a spanwise spacing $d_{VG,exp}$ at an angle of incidence $\alpha_{VG,exp}$ towards the freestream direction. In experiments, the flap deflection angle δ_{flap} of the short-chord flap was increased by 50% for the takeoff and by 0%, 8% and 23% for the landing configuration compared to the baseline configuration in order to match baseline performance results. The subscripts VG,mod and VG,exp are used in this chapter for clarity reasons.

The experiments have shown that the short-chord flap in takeoff configuration with flow control devices attached could provide the lift performance of the baseline takeoff configuration even though the maximum lift coefficient $C_{L,max}$ could not be achieved. Therefore, the ability of the short-chord flap to replace the baseline configuration in takeoff configuration was only partly shown. The remaining part of this investigation examines only the short-chord flap takeoff configuration in order to evaluate the statistical VG model against the experimental results with flow control devices.

4.2. Computational set-up

A circular computational domain included the HELIX airfoil in its center, surrounded by ca. 70000 nodes. The circular shape made it possible to change the angle of attack α by means of the free stream velocity components without taking additional boundary conditions into account. The mesh around the airfoil was kept fine in regions of high flow curvatures, i.e. especially in the vicinity of the two gaps between the three airfoil elements. The near wall grid points were located at $y^+ = \mathcal{O}(1)$ in order to ensure capturing the viscous effects close to the wall. Yet, there is potential to increase the mesh density in the wall normal direction in order to resolve the near wall effects better. However, it was decided that the mesh was fine enough for examining the trends of such a VG model approach rather than matching experimental results quantitatively 100% correct.

The HELIX airfoil computations were, as the previous flat plate computations, carried out using a DRSM as a constitutive turbulence model with pressure-strain rate model corresponding to the Wallin & Johansson EARSM with curvature correction (Wallin & Johansson 2002). The DRSM was also

linked with the Hellsten $k - \omega$ turbulence model (Hellsten 2005) as a length determining model. The DRSM turbulence model was applied since the VG model was written for use in combination with DRSM models, adding the additional vortex stresses directly to the RANS equations.

Corresponding to experiments, the Reynolds number based on c_{base} and the Mach number were set to $Re = 1.65 \cdot 10^6$ and $M_\infty = 0.13$, respectively.



FIGURE 13. Laminar regions (black) on the airfoil element surfaces.

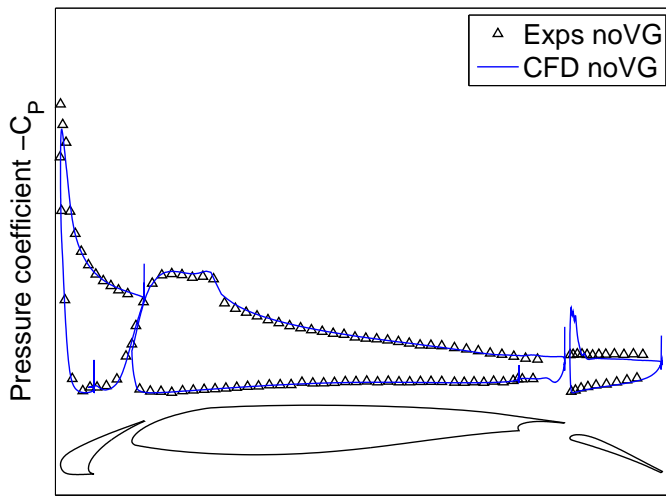


FIGURE 14. C_P distribution plots of experiments and CFD without VGs, transition settings used.

First, test computations without the VG model applied were carried out with fully turbulent flow as well as with pre-defined transition regions on the airfoil element surfaces (see Fig. 13) since Re was rather low and the position of the transition point is an important aspect that neither has been triggered nor measured nor estimated. The purpose of this rather ad-hoc procedure was to match the experimental C_P results without VGs better than with fully turbulent flow. The pressure coefficient is defined as

$$C_P \equiv \frac{P - P_\infty}{P_0 - P_\infty}, \quad (5)$$

where P is the local static pressure, P_∞ the reference static pressure far upstream, and P_0 the total pressure at the reference position. Figure 13 shows the laminar regions colored in black on the three elements for a high angle of attack whereas the transition setting is also based on previous in-house experience on similar cases. The analogous C_P distribution results are given in Figure 14. Here, it can be seen how the grey curve for the computations with transition settings reproduces experimental results with high accuracy. Nevertheless, it is conspicuous that the C_P distribution around the flap shows a peak value close to the flap leading edge. This characteristic is a result of the nonconverged steady RANS computations, indicating the shedding vortices in time whereas the experimental data represent a time-averaged flow regime. Here, nonconverged means that local time-stepping was used which is not time-accurate, giving an indication for a nonstationary solution if computations are not fully converged. The result of introducing the laminar regions was very promising and the laminar/turbulent transition settings were therefore also applied for the flow cases with the VG model.

Second, computations including the statistical VG model were carried out for a range of high α when separation still occurs on the flap. This part of the investigations included a VG model parameter variation of its corresponding modeled VG geometry in terms of shape, chord length $c_{VG,mod}$, height $h_{VG,mod}$, and VG model position $x_{VG,mod}$. These input parameter can be simply set in a preprocessing step, keeping the original mesh without the need of any mesh refinement. In particular, all computations were carried out with the Edge CFD code (Eliasson 2002) and for all runs, the lift slope factor K in Eq. 1 was set to 1.8π , i.e. 10% lower than for the thin airfoil theory.

This chapter presents the experimental data with and without attached flow control devices and the computational results with applied VG model. Test runs have shown that the original experimental set-up including the VG configuration did not lead to separation prevention in computations when the VG model was applied. At this streamwise position, i.e. at 25% c_{flap} , the VG model plane was consequently placed in the mean flow separation region where the model cannot have any effect on the mean flow characteristics. Unlike in computations, such an experimental set-up can lead to separation prevention due to the fact that the flow around the flap device is fluctuating and therefore flow around the VGs is temporarily attached, see also Lin & Pauley (1996) for numerical studies of an airfoil at lower Re . This can be an effective method to generate the needed vortex structures that ensure boundary layer mixing and hence keep the flow attached.

It was chosen to move the VG model further upstream in order to place it in a smaller as well as in a permanently attached boundary layer where the VG model can successfully create the necessary vortex stress forcing terms that act on the mean flow. Moreover, parameter variations of the modeled geometry including the modeled VG height, chord length and shape as well as of the VG

model plane position were carried out. The parameters and their corresponding values related to the experimental set-up are given in Table 4.

TABLE 4. Positions and configuration settings of the VG model on the HELIX short-chord flap; VG model parameters based on corresponding experimental setting.

$x_{VG,mod}$	4%				8%			
$c_{VG,mod}$	50%				100%			
$h_{VG,mod}$	100%		150%		100%		150%	
Shape	▲	■	▲	■	▲	■	▲	■
Configuration	1	2	3	4	5	6	7	8

Figure 15 displays streamline and velocity plots in the vicinity of the main element trailing edge and the flap for the same angle of attack. The comparison clearly shows the differences between the clean and the modified short-chord flap airfoil, here with VG model configuration 8. Furthermore, Figures 16 and 17 show the resulting C_P plots of this investigation that include C_P distributions for all computations from Table 4.

4.3. VG model variation results

4.3.1. Model forcing plane variation

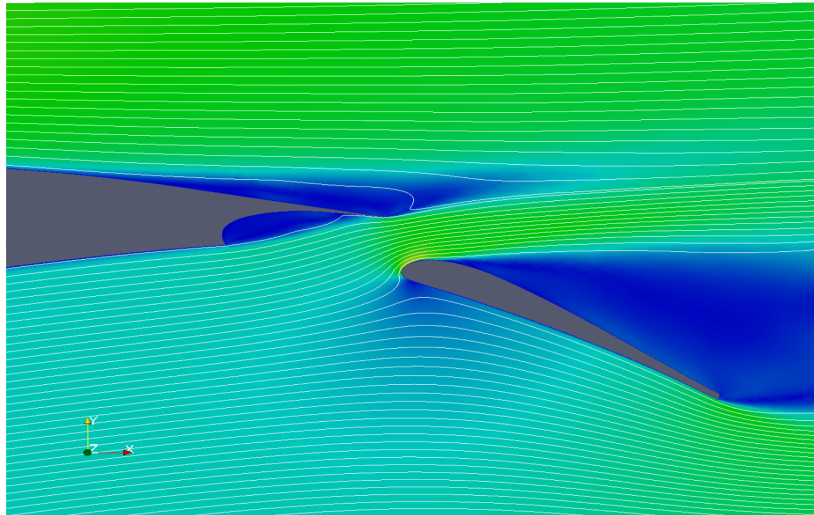
Figure 16 presents the different examined VG models with configuration setting 1-4, located at 4% c_{flap} in addition to the experimental results with VGs attached at 25% c_{flap} . Here, it can be observed that the VG model configurations 1-3 describe almost the same C_P curves on all three elements. Configuration 4 with larger rectangular modeled VGs shows a visible decrease of C_P on the suction side of all airfoil elements leading to a fully attached flow on the flap. It should be mentioned that the VG model is located very close to the laminar/turbulent transition point. Figure 17 shows the corresponding curves at 8% c_{flap} , yet with another value for the modeled VG chord $c_{VG,mod}/c_{VG,exp} = 100\%$ rather than 50% as in the previous case. The reason for the smaller chord was to ensure that the modeled real VG chord would not exceed the leading edge of the flap. The particular effect of different chord lengths will be analyzed separately in upcoming investigations. However, Figure 17 generally shows how the overall peak pressure distribution is decreased on the flap. This might be the consequence of the doubled chord length that leads to a higher Γ_{max} in Equation 1. Moreover, two out of four configurations show almost congruent C_P distributions, compared to only one configuration that fully ensured separation prevention on the flap. This shows that the VG model position plays a role for an optimization of the mixing effects of flow separation prevention devices.

4.3.2. Height variation

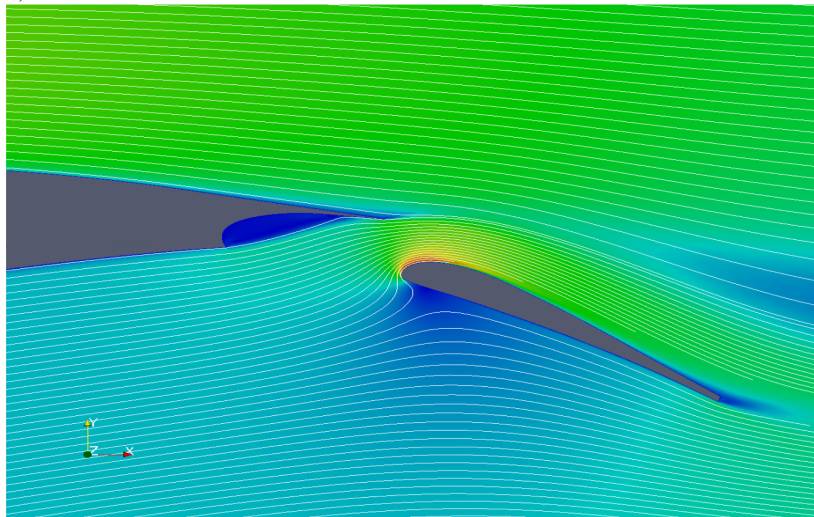
The VG model height $h_{VG,mod}$ has a major influence on the effectiveness of flow separation prevention as can be seen in Figure 17. There, a higher VG model is preventing the mean flow from separation, compare configurations 5 and 7 as well as 6 and 8 with each other. This is a result of the fact that the higher the VG model, the higher are the velocities around the wing tip and the higher gets Γ_{max} in Equation 1, leading to larger additional forcing terms in the RANS equations. Under certain circumstances when this height difference is of relative importance, it can have a nonnegligible impact on the mean flow field, leading to potential flow separation prevention.

4.3.3. Shape variation

Figures 16 and 17 show that the modeled VG shape can lead to differences in the C_P distribution, depending on where the VG model plane is located and how tall the modeled VG is. Figure 16 displays C_P distribution plots for the different VG model configurations for the further upstream located VG model plane location at 4% c_{flap} . There, configurations 3 and 4, representing delta and rectangular modeled VGs, respectively, prove to illustrate that the differences regarding a flow separation prevention are considerable. The configurations 1 and 2 do not show this sensitivity but, for this case, it is presumed that the VG model height has more importance on the results than the modeled shape. Figure 17 does not show any sensitivity in the C_P distributions at all for a shape variation, the small differences for configurations 5 and 6 occur from the nonconverged steady computations, giving different flow states as a result of the fluctuating and separated flow region on the flap.



a)



b)

FIGURE 15. Velocity magnitude (blue: low velocity; red: high velocity) and streamline plots for a) the clean airfoil without VG model; b) the modified airfoil with the VG model configuration 8 applied: $x_{VG,mod}/c_{flap} = 8\%$, $c_{VG,mod}/c_{VG,exp} = 100\%$, $h_{VG,mod}/h_{VG,exp} = 150\%$, rectangular shape.

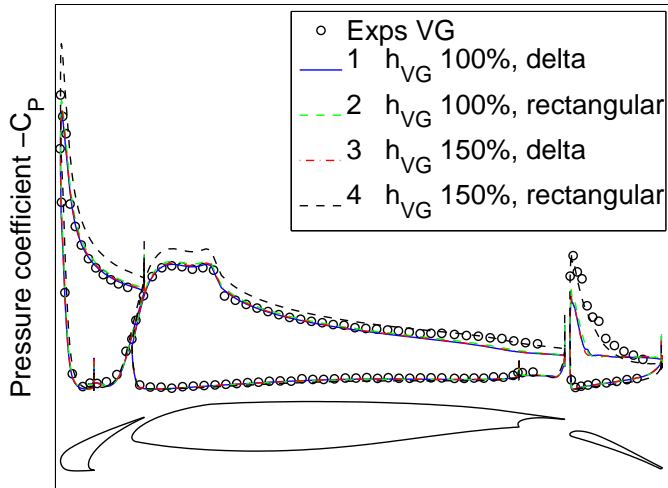


FIGURE 16. C_P distribution plots: experiments with VGs at 25% c_{flap} and computations with different VG model configurations 1-4, see Table 4. The VG model plane is located at $x_{VG,mod}/c_{flap} = 4\%$ with a modeled chord length of $c_{VG,mod}/c_{VG,exp} = 50\%$.

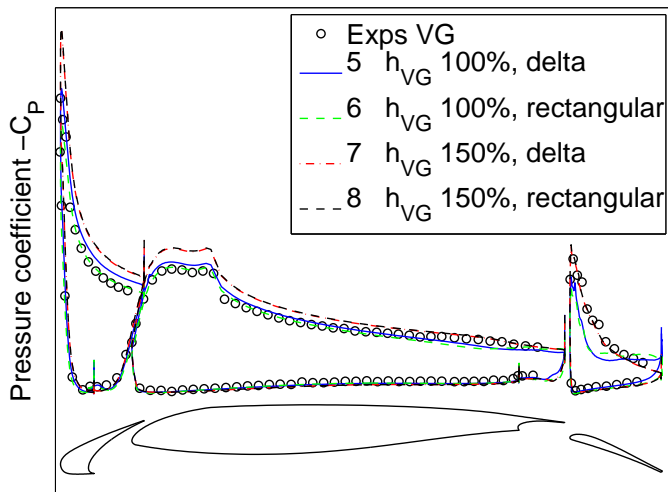


FIGURE 17. C_P distribution plots: experiments with VGs at 25% c_{flap} and computations with different VG model configurations 5-8, see Table 4. The VG model plane is located at $x_{VG,mod}/c_{flap} = 8\%$ with a modeled chord length of $c_{VG,mod}/c_{VG,exp} = 100\%$.

5. KTH plane asymmetric diffuser flow study

In addition to the flat plate ZPG and the external high Re flow around the HELIX airfoil, a brief computational study introducing the internal APG flow in the KTH asymmetric diffuser was carried out. This was done in order to complete the qualitative evaluation studies with parameter variations by means of this highly sensitive flow case.

The 2D flow in a plane asymmetric diffuser with a cross section height $H = 30\text{ mm}$ was computationally and experimentally studied by Törnblom (2006). A sketch of the diffuser is presented in Fig. 18. The experimental inlet channel is $> 100H$ long and the outlet channel is $> 80H$ long in order to avoid boundary condition influences on the separating region. For the 2D computations, the corresponding computational domain has a $\approx 100H$ long inlet channel and a $\approx 75H$ long outlet channel. The diffuser itself has a straight wall on the lower side and a 8.5° inclined wall on the upper side, the corners of the inclined walls are rounded with a radius of $10H$, and the diffuser outlet is $4.7H$ high. Moreover, the plane asymmetric diffuser flow case is often used as an evaluation test case for turbulence modeling, see e.g. Gullman-Strand (2004) and Obi *et al.* (1993). This opening angle gives a weak separation which can be controlled rather easily and is therefore suitable for an evaluation of the VG model. The DRSM turbulence model with Wallin & Johansson EARSIM coefficient settings (Wallin & Johansson 2000) was applied including the Hellsten $k - \omega$ model (Hellsten 2005). The standard Wallin & Johansson EARSIM coefficient settings were initially used, but the obtained separation region was too small and weak. Tuning the ω -production coefficients to $\gamma_1 = 0.688$ and $\gamma_2 = 0.61$ gave a better separation prediction for the baseline setting without VGs and were therefore applied for the VG model cases. In particular, different VG locations $x_{VG,mod}$ and K values were investigated during this study whereas the vortex core radius r_0 and C_ω remained constant, see Table 5.

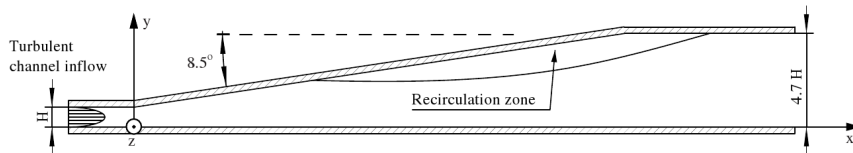


FIGURE 18. KTH diffuser geometry, taken from Törnblom (2006).

In the following paragraphs, the results of this parameter study including turbulent kinetic energy, streamline, velocity, and pressure distribution plots are presented.

Computations without the VG model reveal a rather large separation region in the diffuser, compare Figs. 19 a) and 20. Besides, the results are very similar to experiments. Applying the VG model, the VG1 setting (comparable with experimental VG setup) showed that the influence of the VGs on separation

TABLE 5. Vortex generator model input variables for the KTH diffuser, $h_{VG,mod}/H = 0.6$, $r_0/h = 0.1$, and $C_\omega = 1$.

	$x_{VG,mod}/H$	K
VG1	4.7	1.8π
VG2	4.7	3.0π
VG3	2.0	3.0π
VG4	2.0	1.8π

prevention is too weak, see Fig. 19 b). The streamlines clearly show the separation region in the vicinity of the upper corner of the VG1 setting. Beyond that, the study showed that an increase of K from 1.8π (VG1) to 3.0π (VG2) did only result in a slight rise of the total pressure recovery at the diffuser outlet, giving a slightly smaller separation bubble in the diffuser, see also Fig. 19 c). Because of these marginal differences, it was chosen to omit case VG2 from the following diagrams for clarity reasons.

Due to the persisting separation, it was decided to move the VG model further upstream from $x_{VG,mod}/H = 4.7$ to $x_{VG,mod}/H = 2.0$, compare case VG3 in Table 5. The stronger mean flow at $x_{VG,mod}/H = 2.0$ and therefore the stronger formation of vortices by the VGs has a larger impact on the VG model separation prevention as can be seen in the turbulent kinetic energy and mean velocity profile plots of case VG3 in Fig. 19 d) and Fig. 20 (dashed lines), respectively. The separation region has vanished now and a comparison between the different velocity plots for the different VG model settings in Fig. 20 reveal that also the mean velocity profiles differ significantly between the VG1 and w/o VG settings. Backflow around the upper corner as for the VG1 case is not observable anymore for the VG3 case. The applied VG model establishes a redistribution of the streamwise velocity from the peak velocity region towards the upper wall region, giving rise to higher velocities in its vicinity and, by that, preventing the flow to separate due to the APG.

In order to investigate the effect of the K factor at this position, the VG model was set with the original value $K = 1.8\pi$ at the VG3 position $x_{VG,mod}/H = 2.0$, according to VG4 settings in table 5. Figure 19 e) shows how the strength of the turbulence kinetic energy production is diminished slightly, yet ensuring separation prevention in the diffuser. The velocity plots (dashed dotted lines) in Fig. 20 prove that the lower momentum mixing in the diffuser leads to lower velocities near the upper wall but in turn to higher peak velocities closer to the lower wall when compared to the VG3 case (dotted lines). This proves the sensitivity of the VG model on K .

Figure 21 shows the C_P distribution along the x-direction for computations without VG model, with VG1, VG3, and with VG4 settings as well as for the experimental results without and with VGs (data available here). Here, the pressure coefficient is defined as

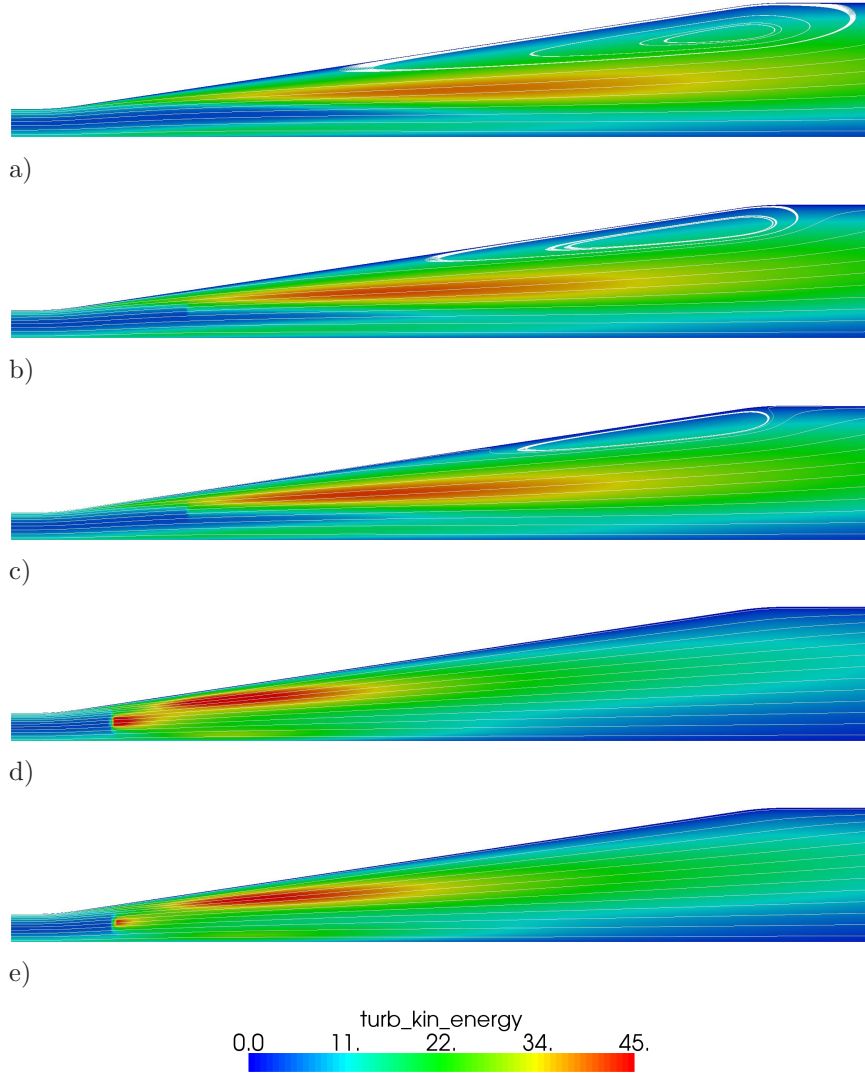


FIGURE 19. Turbulence kinetic energy field and streamlines for VG model computations: a) no VG model, b) VG1, c) VG2, d) VG3, and e) VG4 setting.

$$C_P \equiv \frac{P - P_{ref}}{P_0 - P_{ref}}, \quad (6)$$

where P is the local static pressure, P_{ref} the reference static pressure at the diffuser inlet, and P_0 the total pressure at the diffuser inlet. It can be observed that all pressure plots have qualitatively the same shapes and lie close

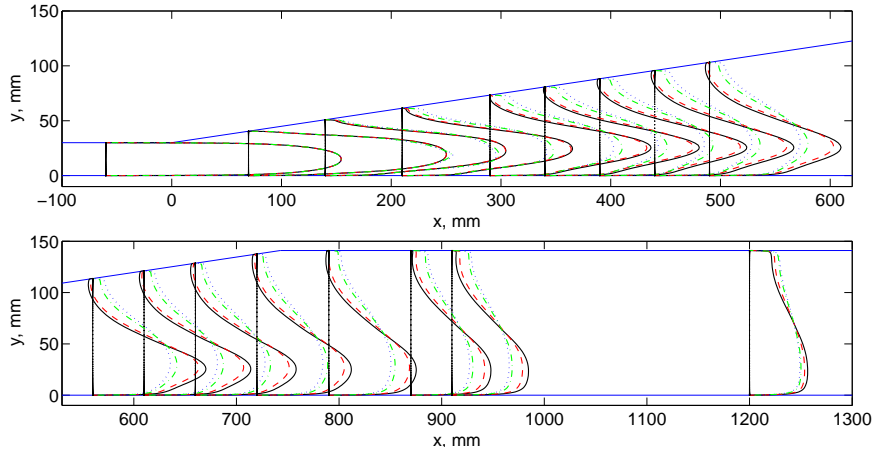


FIGURE 20. Mean streamwise velocity profiles for computations without VG model (—), VG1 (---), VG3 (···), and VG4 (-·-) setting.

to experiments. The computed results without VG model show a similar distribution when compared with experiments without VGs, indicating that the separation bubble is the cause of the poor pressure recovery. The VG1 performs slightly better, reducing the separation region and therefore enhancing the pressure recovery in the diffuser. Nevertheless, the gain in total pressure recovery at the outlet is small. A major step to a much better result is provided by the VG3 settings, being even more efficient than the experimental results with VGs. This can be observed firstly within the diffuser where the pressure recovery is much higher than for VG1 settings and experiments, and secondly at the outlet, indicating a higher total pressure recovery than for VG1 settings and experiments. VG4 computations with a smaller K value than VG3 show a very similar pressure distribution to that in the experiments throughout the diffuser. The total pressure recovery is lower than for VG3 but still higher than in experiments. In total, it can be said that the VG model is capable of describing the separation prevention qualitatively correct by giving the right trends even though the VG1 setting could not perform as well as in the corresponding experiments. As a conclusion of Fig. 21, computations with VG4 setting are representing the best and closest results compared with experiments. On the other hand, it could be shown that the experimental diffuser and its VG configuration could be trimmed in order to achieve higher efficiency.

6. Conclusions

The application of the statistical VG model has shown its capabilities to mimic the effects of VG arrays within turbulent boundary layers by means of introducing additional vortex stresses to the mean governing equations. One constraint of the 2D Lamb-Oseen vortex model used is that the streamwise vortex velocity

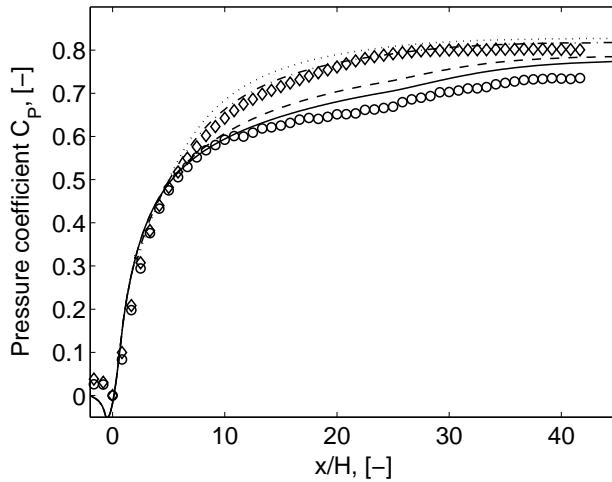


FIGURE 21. Streamwise C_P distributions for experimental results with VGs (\diamond), without VGs (\circ) and for computations without VG model (-), VG1 (- -), VG3 ($\cdot\cdot$), and VG4 (- \cdot -) setting.

is zero, leading to additional vortex stress forcing terms only in the yz -plane, $\Delta\overline{v'v'}$ and $\Delta\overline{w'w'}$, respectively. Thus, the additional vortex stresses $\Delta\overline{u'u'}$ and $\Delta\overline{u'v'}$ are zero, leading to inconsistent stress distributions for $\overline{u'u'}$ and $\overline{u'v'}$ in the VG model plane. However, within the initial nearfield transient up to $x/h = 2.8$ in the ZPG flat plate case, $\overline{u'v'}$ is produced through a transfer of energy from the vortex stresses $\Delta\overline{v'v'}$ and $\Delta\overline{w'w'}$ within the RST model. Further downstream up to $x/h = 9.4$, the VG model $\overline{u'v'}$ vortex stresses are similar to both the experimental and fully resolved CFD results. For even larger streamwise distances, results deviate since the additional vortex stresses are included in the Reynolds stresses which in turn diffuse faster than the stresses from fully resolved structures.

Implementing the VG model in engineering applications has shown that it generally underpredicts the influence on controlling flows, even though total trends and tendencies as seen in the C_P distribution plots are throughout correct. In the HELIX airfoil case, the VG model had to be moved further upstream towards higher VG tip velocities in the VG model plane in order to give attached flow. The investigation of the KTH diffuser showed that the modeled VG did not completely prevent flow separation when corresponding experimental geometries were used. Again, the VG model had to be moved further upstream in order to control the flow. Beyond that, investigating the influence of the lift slope coefficient K showed that its adjustment had a slight

influence on separation prevention in the diffuser. In combination with the results of the K variation in Ch. 3.2.1, a further calibration is not expected to improve results very much.

The lower impact phenomena of the VG model might originate from the limited vortex model that is used. As mentioned previously in Ch. 2, the vortex model lacks an axial velocity component that leads to an incomplete description of the additional modeled vortex stresses in the forcing plane. Even though it was shown that the $\overline{u'v'}$ component is eventually produced in the nearfield transient, it might play an important role when it comes to strong redistributive effects within the boundary layer very close downstream of the VG model forcing plane. Furthermore, stress production might differ essentially when the VG model is exposed to APG flow. Chapter 3.3 has shown how spanwise averaged stresses from fully resolved data develop when used as imposed initial conditions in combination with the VG model approach. It could be shown how the $\overline{u'v'}$ stresses differ in the nearfield whereas the farfield distribution was very similar when compared with the previous standard runs. This might emphasize the need to focus much more on the nearfield development than has been done so far.

In summary, this investigation has proved that the introduced statistical modeling of VGs as turbulent flow separation devices is promising, producing qualitatively correct results when the contemplated underprediction is taken into account. Nevertheless, some research has to be carried out in order to improve the VG model, eliminating the tendency to underpredict its influence. A quantitative evaluation of the VG model is scheduled, not only leading to prediction of its general trends and tendencies but also developing it into a useful and reliable tool for flow control applications. Moreover, the VG model introduces the opportunity to carry out parameter variations fastly and efficiently without the need for rebuilding the computational mesh. It is finally also important to note that this approach has the advantage of not being more computationally expensive than solving RANS equations without modeled devices, leading to much faster results than with conventional methods such as fully or partly resolved VGs.

Acknowledgments

The ZPG flat plate experiments were carried out within a cooperative research program between KTH Stockholm and Scania AB, Sweden. Special thanks to Ola Lögberg and Dr. Jens Fransson for the provision of experimental results. The experimental data for the HELIX airfoil are originated from the EC 5th Framework programme HELIX, GRDI-2000-25205. This project was supervised by Simon Galpin of Airbus. Special thanks also to Ulf Tengzelius of FOI for his help and comments regarding the HELIX project.

References

- ANDERSON, J. D. 1991 *Fundamentals of Aerodynamics*, 2nd edn. New York, USA: McGraw-Hill.
- BATCHELOR, G. K. 1964 Axial flow in trailing line vortices. *Journal of Fluid Mechanics* **20** (4), 645 – 658.
- BENDER, E. E., ANDERSON, B. H. & YAGLE, P. J. 1999 Vortex Generator Modelling for Navier-Stokes Codes. *American Society of Mechanical Engineers FEDSM* **99-6919**.
- BRAGG, M. B. & GREGOREK, G. M. 1987 Experimental Study of Airfoil Performance with Vortex Generators. *Journal of Aircraft* **24** (5), 305 – 309.
- ELIASSON, P. 2002 Edge, a navier-stokes solver for unstructured grids. *Proceedings to Finite Volumes for Complex Applications III* pp. 527 – 534, edited by D. Kroner and R. Herbin, Hemre Penton Science London.
- GLAUERT, H. 1926 *The Elements of Aerofoil and Airscrew Theory*, 1st edn. Cambridge University Press, London, UK.
- GULLMAN-STRAND, J. 2004 Turbulence and Scalar Flux Modelling Applied to Separated Flows. PhD thesis, Department of Mechanics, KTH Stockholm.
- HELLSTEN, A. 2005 New Advanced $k - \omega$ Turbulence Model for High-Lift Aerodynamics. *AIAA Journal* **43** (9), 1857–1869.
- JIRÁSEK, A. 2005 A Vortex Generator Model and its Application to Flow Control. *Journal of Aircraft* **42** (6), 1486–1491.
- LIN, J. C. 1999 Control of Turbulent Boundary-Layer Separation using Micro-Vortex Generators. *30th AIAA Fluid Dynamics Conference, Norfolk, VA, USA AIAA* **1999-3404**.
- LIN, J. C. 2002 Review of research on low-profile vortex generators to control boundary-layer separation. *Progress in Aerospace Sciences* **38**, 389–420.
- LIN, J. C., ROBINSON, S. K. & MCGHEE, R. J. 1994 Separation Control on High-Lift Airfoils via Micro-Vortex Generators. *Journal of Aircraft* **31** (6), 1317 – 1323.
- LIN, J. C. M. & PAULEY, L. L. 1996 Low-Reynolds-Number Separation on an Airfoil. *AIAA Journal* **34** (8), 1570 – 1577.
- LÖGDBERG, O. 2008 Turbulent Boundary Layer and Separation Control. PhD thesis, Department of Mechanics, KTH Stockholm.
- LÖGDBERG, O., FRANSSON, J. H. M. & ALFREDSSON, P. H. 2009 Streamwise Evolution of Longitudinal Vortices in a Turbulent Boundary Layer. *Journal of Fluid Mechanics* **623**, 27–58.
- OBI, S., AOKI, K. & MASUDA, S. 1993 Experimental and Computational Study of Turbulent Separating Flow in an Asymmetric Plane Diffuser. *Ninth Symp. on turbulent shear flows, Kyoto, Japan* p. 305.
- ÖSTERLUND, J. M. 1999 Experimental Studies of a Zero Pressure-Gradient Turbulent Boundary Layer Flow. PhD thesis, Department of Mechanics, KTH Stockholm.
- PAULEY, W. R. & EATON, J. K. 1988 Experimental Study of the Development of Longitudinal Vortex Pairs Embedded in a Turbulent Boundary Layer. *AIAA Journal* **26** (7), 816 – 823.
- RAE, A. J., GALPIN, S. A. & FULKER, J. 2002 Investigation into Scale Effects on the

- Performance of Sub Boundary-Layer Vortex Generators on Civil Aircraft High-Lift Devices. *1st Flow Control Conference, St. Louis, Missouri, June 24-26, 2002* **AIAA 2002-3274**.
- VON STILLFRIED, F., WALLIN, S. & JOHANSSON, A. V. 2009 Statistical Modeling of the Influence of Turbulent Flow Separation Control Devices. *47th AIAA Aerospace Sciences Meeting, Orlando, FL, USA* **AIAA 2009-1501**.
- TÖRNBLOM, O. 2006 Experimental and Computational Studies of Turbulent Separating Internal Flows. PhD thesis, Department of Mechanics, KTH Stockholm.
- TÖRNBLOM, O. & JOHANSSON, A. V. 2007 A Reynolds stress closure description of separation control with vortex generators in a plane asymmetric diffuser. *Physics of Fluids* **19**.
- VELTE, C. M., HANSEN, M. O. L. & OKULOV, V. L. 2009 Helical structure of longitudinal vortices embedded in turbulent wall-bounded flow. *Journal of Fluid Mechanics* **619**, 167 – 177.
- WALLIN, S. & JOHANSSON, A. V. 2000 An explicit algebraic Reynolds stress model for incompressible and compressible turbulent flows. *Journal of Fluid Mechanics* **403**, 89–132.
- WALLIN, S. & JOHANSSON, A. V. 2002 Modelling streamline curvature effects in explicit algebraic Reynolds stress turbulence models. *International Journal of Heat and Fluid Flow* **23** (5), 721–730.
- WALLIN, S. & MÅRTENSSON, G. E. M. 2003 A General 1D-solver for Partial Differential Equations. *Tech. Rep.* Department of Mechanics, KTH Stockholm.
- WENDT, B. J. 2001 Initial circulation and peak vorticity behavior of vortices shed from airfoil vortex generators. *Tech. Rep.* NASA.
- YAO, C.-S., LIN, J. C. & ALLAN, B. G. 2002 Flow-Field Measurement of Device-Induced Embedded Streamwise Vortex on a Flat Plate. *1st AIAA Flow Control Conference, St. Louis, MO, USA* **AIAA 2002-3162**.

Paper 2

Evaluation of a Vortex Generator Model in Adverse Pressure Gradient Boundary Layers

By Florian von Stillfried, Stefan Wallin, and Arne V. Johansson

Royal Institute of Technology Stockholm
Linné Flow Centre
Department of Mechanics
SE - 100 44 Stockholm, Sweden

Submitted to AIAA Journal

A statistical vortex generator (VG) model applied in the adverse pressure gradient (APG) flow on a flat plate is used in order to evaluate the sensitivity of this VG model approach qualitatively. The modeling of such passive VGs has the advantage to heavily reduce the complexity of including such flow separation devices in a computational mesh, giving the opportunity to carry out parameter studies rapidly. Stresses, originating from the VGs, are modeled and added as additional turbulent stresses to the mean governing equations instead of resolving vortex structures in the computational domain. The baseline setting is based on previous experiments at KTH Stockholm, and APG flat plate results without VGs were compared to corresponding computations. In a further step, the VG model was applied as in experiments and a parameter variation of the VG model streamwise position was carried out. Wall pressure and skin friction coefficient distributions were used in order to judge the VG model. It could be shown that the VG model successfully prevents flow separation for the baseline case, leading to attached flow. Moreover, sensitivity on the flow separation prevention strength could be shown for different VG model streamwise positions by means of skin friction plots.

1. Introduction

The use of flow control in modern engineering applications is nowadays very common as the use of flow separation control devices has proven to enhance boundary layer flows, e.g. in inlet ducts, or on aircraft wings. The application of passive vortex generator (VG) vanes typically energizes low-momentum boundary layer flow by means of increased momentum mixing near walls. Because of delayed or even vanished separation, positive effects are very often lower drag generation, decreased loads, lower design weight, and increased efficiency. Negative aspects also occur, mostly in form of e.g. increased drag.

However, such a trade-off situation often favors the use of such devices due to their overall advantages.

Passive VGs have been examined by many researchers until today as the effects on flow separation prevention is already well-known for decades. Yet and depending on the flow case, there are still many uncertainties about the specific configurations for maximizing the efficiency. Taylor (1947) introduced VGs as large as the local boundary layer thickness δ_{99} in order to increase the momentum transfer towards the wall. These "conventional" VGs were attached perpendicularly to the wall in an angle of incidence α_{VG} to the free stream direction. This is generally the common way to equip surfaces with such passive devices.

One of the first comprehensive articles about flow separation control and its design for airfoils and wings was published in the paper by Pearcey (1961). It also includes a large chapter about VGs, different systems as co-rotating, counter-rotating, multiple row, and biplane systems as well as different types of VGs including air-blowing systems.

Experimental studies with a focus on optimal parameters were e.g. carried out by Pauley & Eaton (1988). They investigated vortex structures within a turbulent boundary layer and concluded that there exist optimal settings for momentum mixing regarding the VG blade angle of incidence α_{VG} and spacing d . Also included in the experiments were different VG settings, again co- and counter-rotating but also unequal systems. A result of their studies was e.g. that systems that generated "common flow up" structures between two neighbouring VG blades are commonly less efficient than those that produce "common flow down" structures.

Godard & Stanislas (2006) carried out a study regarding optimal parameters of VGs in a decelerating boundary layer. They investigated several parameters as e.g. the height, the shape, the position, the spanwise spacing, and the blade distance of counter-rotating paired devices. Co-rotating devices were also included in this study, yet not as comprehensive as counter-rotating VGs. For example, counter-rotating devices turned out to perform better than co-rotating devices, leading to twice the skin friction increase when applied. In particular, the VG shape seems to have importance for the efficiency, giving advantages for triangular VG vanes. Also the VG blade angle of incidence α_{VG} is described to be sensitive, leading to a maximum value at $\alpha_{VG} \approx 18^\circ$. On the other hand, other parameters like the VG aspect ratio \mathcal{R} and the VG streamwise position x_{VG} did not show high sensitivity to changes. In total, Godard and Stanislas showed that skin friction measurements are an appropriate and sensitive way for the investigation of flow separation control. Furthermore, they present optimal parameters for co- and counter-rotating VG arrays.

The paper by Godard & Stanislas (2006) and their starting parameters are very close to optimal parameters from Lin (2002). Lin has presented a comprehensive overview on ongoing research within the area of sub-boundary vortex generators (SBVG), stating that it is necessary to diminish the size of such

devices to $h_{VG}/\delta_{99} \leq 0.5$ in order to maximize efficiency and decrease drag production by such devices. Lin (2002) also presents research of numerous different shapes and system settings regarding their effectiveness on flow separation control, coming to the conclusion that SBVGs and larger conventional passive VGs reduce the separation region better than other devices.

In contrast to experiments, the investigation of passive vane VGs leads to different implementation problems in computational fluid dynamics (CFD). Here, it is common to introduce VGs by resolved structures in the generated mesh. This is a very direct and intuitive approach, yet leading to many additional grid points in the VG vicinity. In turn, this implementation needs to be done carefully in order to resolve the vortex structures in the flow, leading to high costs for the mesh generation. Moreover, parameter variations cannot be carried out easily because the mesh has to be changed again according to new settings, giving rise to even higher grid generation costs the more comprehensive a parameter variation gets.

The development of VG modeling is the consequent approach that has become more and more used within the last decade. Bender *et al.* (1999) have introduced a (BAY) VG model that uses forcing source terms, based on the lifting line theory (LLT, see e.g. Glauert 1926), that are in turn added to the momentum equations. Also Jirásek (2005) presented a VG model, improving the existing BAY model by removing some of its drawbacks. The two approaches have in common that their meshes require three dimensions in order to account for the generated lifting force at the modeled VG position. Yet, geometrical structures of the VGs are removed, reducing the complexity of the grid generation to only resolving for the generated vortex structures downstream of the forcing region.

Another step towards a simplification of the application of VGs within CFD is the introduction of statistical methods as done by Törnblom & Johansson (2007). Here, a Reynolds stress approach is used in a statistical sense. Additional stresses that originate from such modeled VGs and their additional vortex velocity field are added to the mean governing equations. The core of this model is a two-dimensional (2D) vortex model in combination with the LLT that also takes some of the VG's geometrical aspects into account. By spanwise averaging the second-order statistics of the additional vortex velocity field in the forcing plane, vortex stress contributions are formed and added to the Reynolds stress tensor. This method can be applied in 2D as well as for three-dimensional (3D) meshes.

Investigations of this statistical VG model in a zero pressure gradient (ZPG) boundary layer flow over a flat plate are presented in von Stillfried *et al.* (2009a) and von Stillfried *et al.* (2009b). There, the VG model could be successfully applied to the flat plate ZPG flow case, a wing profile, and in internal diffuser flow. The investigations have moreover shown that the statistical modeling of VGs was effectively deployed and has the advantage of not being more computational expensive than solving RANS equations.

The main objective of this work is to examine the capabilities of the statistical VG model in adverse pressure gradient (APG) flow over a flat plate, establishing a pressure-induced separation region. This flow case was previously carried out experimentally by Lögdberg *et al.* (2009). First, the clean flat plate with APG was investigated and adjusted in order to match experimental results, i.e. the wall pressure distribution along the streamwise coordinate. Then, the 2D VG model was introduced in the flow at the respective position as in experiments. Second, a parameter variation study was conducted, using different streamwise positions for the VG model forcing region. The results were then compared to experimental results without flow control devices and to 3D computations including fully resolved VGs.

2. Methods for implementation

The methods to implement the VG model approach were presented in depth in Törnblom & Johansson (2007), von Stillfried *et al.* (2009a), and von Stillfried *et al.* (2009b). Yet, the basic ideas are briefly presented in this section.

The VG model approach has its origin in the Prandtl lifting-line theory (LLT, see e.g. Glauert 1926) and the circulation distribution across a wing in free flight is given by

$$\Gamma(y) = \frac{K}{2} U(y) c(y) \left[\alpha(y) - \frac{w(y)}{U(y)} \right], \quad (1)$$

where K is the local section lift slope of the wing ($K_{max} = 2\pi \text{ rad}^{-1}$ according to thin airfoil theory), $U(y)$ is the local incoming free stream velocity, $c(y)$ the local chord length of the wing, $\alpha(y)$ the local angle of attack, and $w(y)$ the local downwash due to the trailing vortex sheets. The ratio $w(y)/U(y)$ is the local induced angle of attack $\alpha_{ind}(y)$ for small angles α , and the local downwash $w(y)$ reads

$$w(y) = \frac{1}{4\pi} \int_{-h}^h \frac{d\Gamma}{dy'} \frac{1}{y' - y} dy'. \quad (2)$$

Due to limitations for the application of the LLT to VGs in wall-bounded viscous flows, the LLT is only used as an approximation for deriving the circulation distribution, and by means of a vortex model, also for the additional vortex velocity field. Using a 2D Lamb-Oseen vortex model, the azimuthal vortex velocity distribution for one VG blade reads

$$u_\Phi(r) = \frac{\Gamma_{max}}{2\pi r} \left[1 - \exp\left(\frac{-r^2}{r_0^2}\right) \right], \quad (3)$$

with Γ_{max} from the LLT circulation distribution, r_0 the vortex core radius and r the radial coordinate from the vortex center. A limitation of this 2D vortex model is that the velocity component in the streamwise direction is constant. Different other approaches appear in literature, as e.g. Velte *et al.* (2009) describes helical vortex structures of longitudinal vortices by a simplified

Batchelor vortex model (Batchelor 1964), taking the streamwise velocity into account, too.

A VG array consists of more than one VG so that all VGs influence the vortex flow field everywhere in the VG model forcing plane. Due to that, a superposition of the vortex induced velocities $u_\Phi(r)$ for each VG and their corresponding blades was needed as shown in Fig. 1. Here, the wall acts approximately as a symmetry condition for the vortices, which is simulated by introducing mirror vortices.

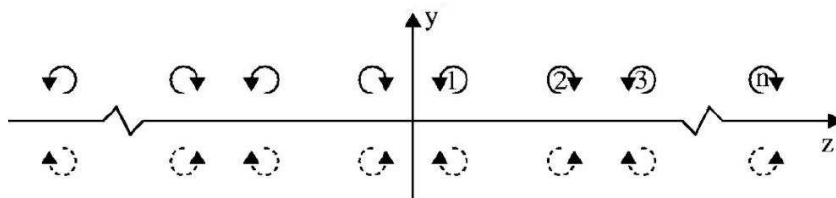


FIGURE 1. Vortex array with n VG pairs and their mirror images for computing the total superpositioned vortex-induced velocity field $u'_i(y, z)$ in the VG model forcing plane, taken from Törnblom & Johansson (2007).

The additional total superpositioned vortex velocity field $u'_i(y, z)$ is then used by means of the corresponding second-order statistics which are assumed to act as additional Reynolds stresses on the flow. Spanwise averaging over one VG pair distance D , see Fig. 2, of these contributions is established in order to derive the VG model stresses, see Eq. 4:

$$\Delta \overline{u'_i u'_j}(y) = \frac{1}{D} \int_{-D/2}^{D/2} u'_i(y, z) u'_j(y, z) dz. \quad (4)$$

The VG model approach is suitable for the use within an RST turbulence model that accounts for each Reynolds stress component. Moreover, the energy transfer between the different components is established by an RST model, enabling $\overline{u'v'}$ Reynolds stress production which is initially not forced by the 2D VG model.

3. Experimental set-up

The corresponding geometry of the modeled VGs was earlier experimentally examined by Lögdberg *et al.* (2009), see also figures 2, 3 and Table 1. Each VG pair consisted of two rectangular flat plates of height $h_{VG} = 18$ mm, mounted at angles of incidence $\alpha_{VG} = \pm 15^\circ$, and a chord length $c/\cos \alpha_{VG}$ with $c = 54$ mm being the projected chord in the streamwise direction. The mean distance between such two blades was $d = 37.5$ mm and the distance between two adjacent VG pairs was $D = 150$ mm. The VGs were mounted in an array consisting of $n = 5$ VG pairs with their trailing edges (TE) located at x_{VGTE}

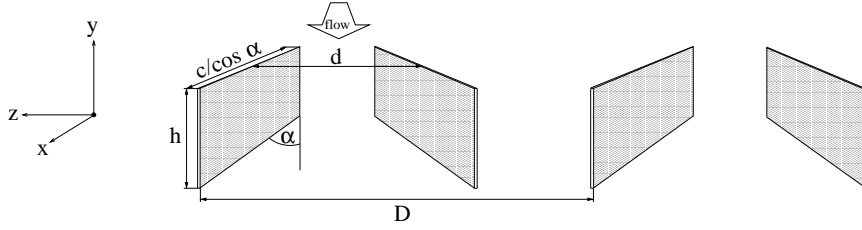


FIGURE 2. Vortex generator geometry from experiments, data given in table 1.

TABLE 1. Vortex generator geometry data from experiments.

h_{VG} [m]	d [m]	D [m]	c [m]	α_{VG} [°]	x_{VGTE} [m]
0.018	0.0375	0.150	0.054	± 15	1.54

= 1.54 m from the leading edge (LE) of the flat plate in the test section of the boundary layer (BL) wind tunnel at KTH Stockholm. The free stream velocity U_∞ was 26.5 ± 0.1 m/s and the temperature had a constant value of $T = 20^\circ\text{C}$. At the streamwise position $x_{VGTE} = 1.54$ m, the boundary layer thickness had a value of $\delta_{99} = 42$ mm and, therefore, the VGs can be characterized as SBVGs, giving a ratio $h_{VG}/\delta_{99} = 0.43$. The BL wind tunnel has a 4.0 m long test section with a cross sectional area of 0.75×0.50 m² and features a temperature control system for keeping a constant temperature within $\pm 0.03^\circ\text{C}$. A flat plate made of acrylic glas splits the wind tunnel's test section and is mounted with a distance of 0.30 m to the test section's upper wall, see Fig. 3. At the wind tunnel inlet, the test section has a width of 0.50 m which is diverged by a back side curved wall at $x = 1.25$ m downstream of the flat plate LE in order to induce the APG. Furthermore, a suction system is installed at the curved wall so that flow separation is prevented there. Another feature of the suction system was the additional capability to change the APG strength through adjusting the suction rate at the curved wall. In total, three different APG cases were performed with suction rates of 6 – 7 %, 12.5 – 13 % and 17 % of the incoming mass flow, see Figs. 3 and 4. All flow field measurements were performed with particle image velocimetry (PIV). The interested reader is referred to Lindgren & Johansson (2004) for further details of the wind tunnel and to Lögdberg *et al.* (2009) as well as to Angele (2003) for further details of the experiments, the set-up and the measurement techniques.

During this investigation, case II with a suction rate of 12.5 – 13 % and its corresponding resulting pressure distribution was used for setting up the computations and for later comparison, see also Fig. 4 where all three different APG cases and their pressure coefficient distributions are shown. The pressure coefficient is defined as

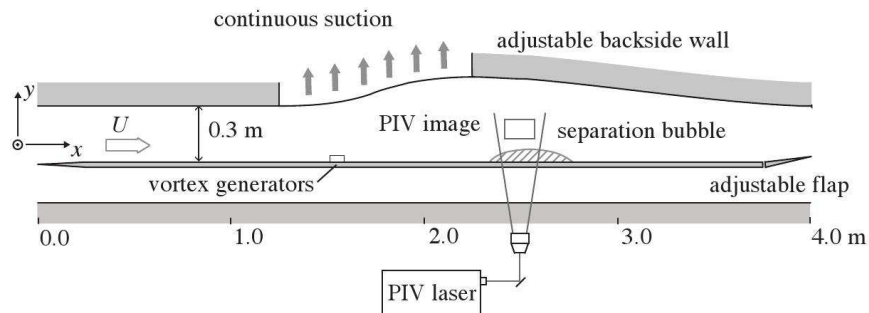


FIGURE 3. Sketch of the boundary layer wind tunnel test section used in experiments, taken from Lögberg et al. (2009).

$$c_P \equiv \frac{P - P_{ref}}{P_0 - P_{ref}}, \quad (5)$$

where P is the local wall static pressure, P_{ref} a reference value, and P_0 the total pressure at the reference position. Case II represented the most comprehensive investigated APG case and was therefore chosen for this investigation. The separation bubble for the experiments was defined as the region where at least 50 % backflow at the wall is developed, i.e. the wall backflow coefficient $\chi_{wall} \geq 0.5$. According to Dengel & Fernholz (2009), χ was extrapolated to the wall from the data points in the region $y \approx 1.5 - 10$ mm in order to estimate χ_{wall} . The resulting geometrical properties such as the separation location x_{sep} , the reattachment location x_{att} , the length l_{sep} as well as the height of the separation bubble h_{sep} are given in the first row of table 2.

4. Computational set-up

This investigation includes three computational cases: a 2D case of a clean flat plate, a 2D case with the VG model applied and a 3D case that fully resolved the VG vanes on the flat plate. The following abbreviations are used in this paper in order to label the different computations:

1. FP2D, for the clean 2D flat plate without VG model,
2. VG2D, for the 2D flat plate with VG model applied,
3. VG3D, for the 3D flat plate with fully resolved VGs.

Furthermore valid throughout this paper, the FP2D and VG2D computations were carried out using a differential Reynolds stress model (DRSM) as a turbulence model with a pressure-strain rate model corresponding to the Wallin & Johansson (WJ) explicit algebraic Reynolds stress model (EARSM) with curvature correction (Wallin & Johansson 2002). This WJ-DRSM was linked with the Hellsten $k - \omega$ turbulence model (Hellsten 2005). The VG3D computations, instead, were carried out by means of the WJ-EARSM turbulence

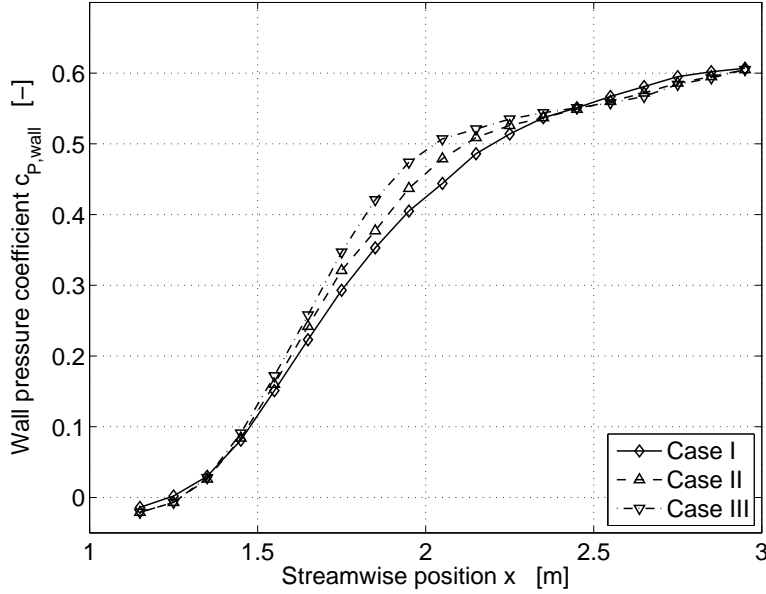


FIGURE 4. Wall pressure coefficient distributions for the three different experimental APG cases.

model without curvature correction (Wallin 2000), again linked with the Hellsten $k-\omega$ turbulence model. This was done since the VG model was formulated for DRSM turbulence models and because the VG3D case solely resolved the vortex structures in the flow itself, not in the turbulence description as for the VG model. All computations were carried out with the Edge CFD code (Eliasson 2002) and the lift slope factor K in Eq. 1 was set to 1.8π for all VG model computations, i.e. 10 % lower than for the thin airfoil theory.

4.1. Boundary conditions for APG flow

For all computational cases, a 0.25 m high and 7.25 m long rectangular computational domain was created, which included a 0.25 m long symmetry plane in front of the flat plate, giving a total length of $l = 7.00$ m for the wall boundary. The height of the domain was therefore 0.05 m smaller than in experiments, compare with Fig. 3. For both domains, the upper boundary was divided into two parts: first, a no-slip wall boundary part from the inflow boundary at $x = -0.25$ m up to $x = 1.25$ m that forced the flow in the x-direction as in the experiments. Second, another boundary from $x = 1.25$ m up to the outflow position at 7.00 m with weak characteristic boundary conditions where an APG and a following favorable pressure gradient (FPG) distribution was set in order to generate the corresponding wall pressure distribution from experiments on the flat plate in computations, compare with Fig. 4. This straight upper boundary established outflow and inflow across its boundary, simulating the APG/FPG

of the experiments. The pressure P and the corresponding velocities u and v were set as initial boundary conditions according to inviscid theory. The APG in the experiments was established, as described previously, through a curved upper wall and a suction system on it. This could not be simulated in computations and therefore the described boundary conditions for the computations are not exactly equivalent to experiments.

For both the 2D and the 3D grid, the value for the first grid point at the wall was set to $y = 10^{-5}$ m throughout the domain, giving values of $y^+ = \mathcal{O}(1)$. As mentioned previously, the computational domain in 3D fully resolved the VGs, assuming a no-slip condition not only on the flat plate but also on the VG blades. In addition and in contrast to experiments, the VG blades were assumed to be rather thin. Furthermore, symmetry conditions were applied on its xy-boundary planes so that the computational domain could be reduced to including only one VG blade, therefore leading to a 3D grid depth of one half VG pair distance $D/2 = 0.075$ m (see table 1 and Fig. 2). The computational mesh was generally kept fine in the vicinity of the VGs by means of an O-grid topology, and consisted in total of more than 1.9 million nodes.

The free stream velocity and the temperature at the inlet were set according to experiments to $U_\infty = 26.46$ m/s and $T = 20^\circ\text{C}$, respectively, giving a Reynolds number based on the plate length $Re_l \approx 1.42 \cdot 10^7$. The pressure distribution on the flat plate from experiments was given between $x = 1.15$ m - 2.95 m, see also Fig. 4, and therefore did not cover the whole x-coordinate range that was needed for the computations. Therefore, the given wall pressure distribution was mirrored at its peak value at $x_{p_{wall,max}} = 2.95$ m and a constant continuous pressure was imposed for $x \geq 4.75$ m down to the domain outlet. Nevertheless, it was chosen to impose the APG in computations downstream of $x = 1.25$ m since the experimental $c_{P,wall}$ crosses the zero-pressure line in Fig. 4.

Since early FP2D test runs did not succeed in producing the desired separation bubble on the flat plate, the APG distribution on the upper boundary was slightly changed in peak strength while keeping the same shape as in Fig. 4. FP2D computations with the WJ-EARSM turbulence model resulted in a separated region, see table 2 but the same boundary conditions did not lead to any separation at all for FP2D WJ-DRSM computations. In order to achieve a separated region with such boundary conditions, it was decided to adjust the α_1 coefficient for the production term in the ω -equation of the turbulence model which led to a change in value for α_1 from 0.518 to 0.61. The velocity profiles at the inflow to the APG section are different, indicating that the change in α_1 changes the flow state, see also Fig. 5. In addition it also lowered the c_f distribution for achieving separated flow in the APG section, see Fig. 6. This rather ad-hoc way can be justified by the fact that the main focus of this investigation was primarily the VG model's streamwise position variation and the differences in results. Nevertheless, the ambition was not to suggest a new turbulence model, but to focus on studying the effects of the VG model

TABLE 2. Separation region length and its location from flat plate experiments for case II given in the first row, taken from Lögberg *et al.* (2009), and computational results for different turbulence model FP2D computations, given in the remaining rows.

Case	x_{sep} [m]	x_{att} [m]	l_{sep} [m]	$h_{sep,max}$ [mm]
Exps II	2.24	2.85	0.61	17
EARSM	1.87	2.62	0.75	26
DRSM	-	-	-	-
DRSM _m	1.91	2.42	0.51	26

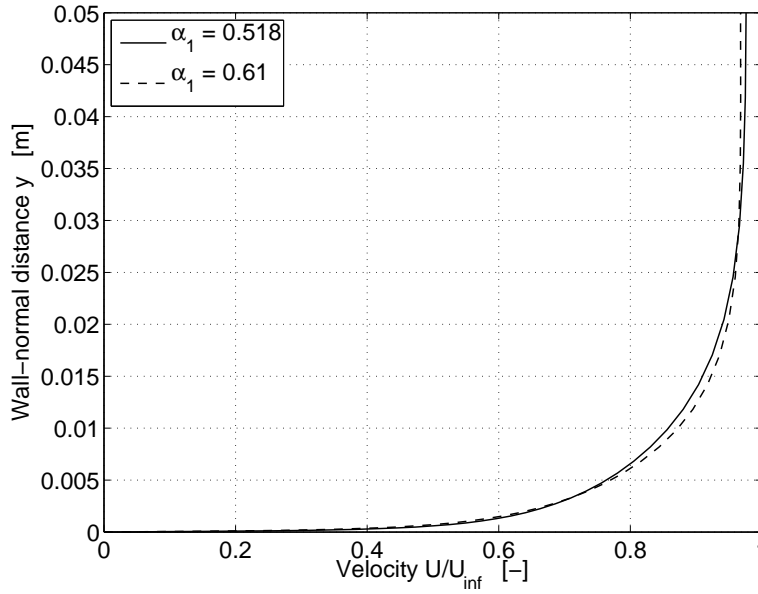


FIGURE 5. Boundary layer velocity profiles at $x = 1.00$ m for the two different α_1 values in the ω -equation.

on separated flow. By adjusting the α_1 value, a similar separation bubble as in experiments could be created even with the DRSM turbulence model, yet positioned ca. 0.30 m further upstream of that in the experiments. Nevertheless, the length of the separated region could be proven to be similar to experiments, see also DRSM_m in Table 2.

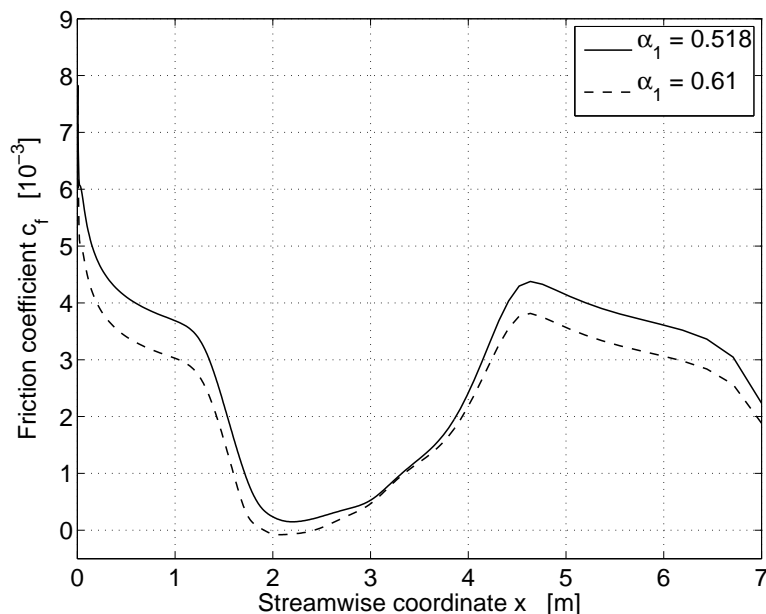


FIGURE 6. Local skin friction coefficient distributions for the two different α_1 values in the ω -equation.

5. Results

This chapter presents the results of the FP2D, the VG2D, and the VG3D computations. A baseline case was set and, in addition, a VG model plane position variation was carried out whereas the VG3D computations were only carried out for the baseline case. Both for the baseline case and for the position variation, skin friction and wall pressure coefficient plots are presented in the subsequent chapters. Furthermore, velocity profiles for a fixed streamwise position are presented. All figures include FP2D, VG2D, and VG3D results. Experimental results without separation control devices, similar to Fig. 4 are also included for the wall pressure coefficient distribution figures.

5.1. Baseline case

The same geometrical parameter set-up as in the experiments was used for the baseline cases with flow control. Thus, the 3D resolved VG geometry and the corresponding VG model input parameters were identical to the data in table 1. The TE of the fully resolved VGs and VG model forcing plane were consequently positioned at $x_{VG_{TE}} = 1.54$ m downstream of the LE of the flat plate.

The APG and the FPG in the experiments (see Fig. 3) were established through the curved upper wind tunnel wall plus the suction system. In the

computations, this was arranged through a prescribed pressure distribution at the upper boundary of the computational domain, as described in Ch. 4.

Figure 7 shows the wall pressure coefficient distribution of both, the uncontrolled cases and the controlled cases. All curves were normalized with corresponding pressures at $x = 1.15$ m. The experimental results show a very steep increase in wall pressure very near the location $x_{APG_{start}} = 1.25$ m. The constant part of dc_p/dx lasts up until ca. $x = 2.00$ m from where on the pressure coefficient flattens and rather quickly develops another constant gradient region from $x = 2.25$ m up to ca. $x_{APG_{end}} = 2.95$ m. This region can be identified as the separated region, compare also with table 2.

The FP2D case gives a rather similar wall pressure distribution, giving a slightly steeper pressure increase and an earlier separation region at $x = 1.91$ m. The peak pressure value is not located in the separation bubble but at ca. $x = 3.10$ m right behind the end of the APG region. The wall skin friction in Fig. 8 shows additional information of the separation bubble location and the general c_f distribution along the ZPG, APG and FPG sections. As expected, c_f decreases quickly close to the LE and starts to fall even quicker when the APG is forced on the flow at $x = 1.25$ m. The skin friction coefficient drops below zero between $x = 1.91$ m - 2.42 m, describing the exact location of the backflow region close to the wall. The increase in skin friction is a direct consequence of the pressure decrease at the wall and reaches a peak where the FPG ends.

The VG2D results instead show how the VG model changes the pressure distribution along the flat plate, see Fig. 7. It can be clearly seen that the pressure gradient is slightly weaker than for FP2D but reaches a higher maximum value. The separation region is not present any more which can be observed in Fig. 8 where the skin friction coefficient does not cross the zero-line anymore. The pressure coefficient at the domain outlet for VG2D is increased by 0.058 compared to the uncontrolled case. This shows the capability of the VG model to prevent separation for this APG flow case, and to decrease the total pressure losses.

Spanwise averaged fully resolved VG3D results are also presented in Figures 7 and 8. It can be seen that the wall pressure distribution is generally slightly lower, yet very similar to the VG2D results as described in the previous paragraph. The pressure loss across the VGs can be detected at around $x = 1.50$ m. The pressure recovery at the outlet is not as high as for the VG2D computations. The skin friction coefficient plot shows an enhanced distribution in the APG section compared to the uncontrolled FP2D results. Later on in the FPG section, the curve collapses with the VG2D curve but diverges as it approaches the downstream constant pressure section. Here the VG3D curve describes a rather different curve than for the VG2D computations. This is possibly the result of the resolved vortex structures that break down as the FPG section ends. The vortex energy could then be transferred into turbulent energy that in turn influences the local skin friction distribution. This difference in skin friction must be investigated in more detail in a future study.

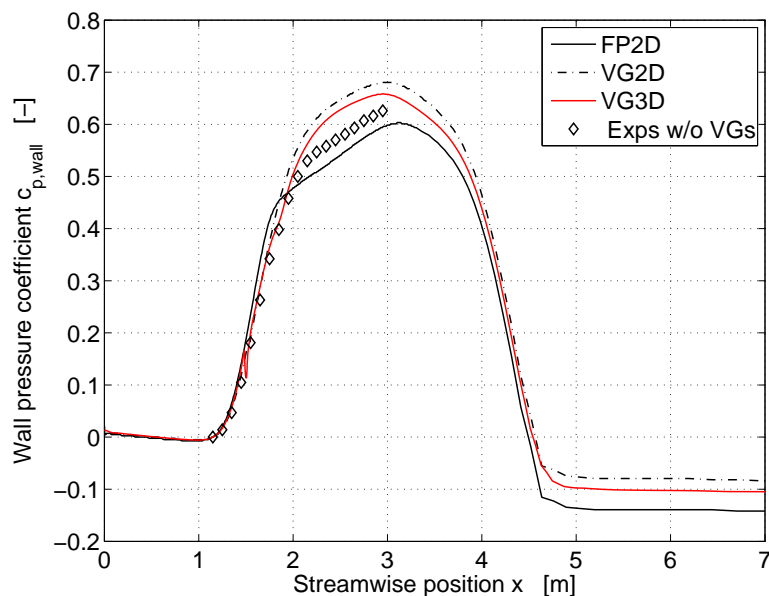


FIGURE 7. Wall pressure coefficient distributions for FP2D, VG2D, VG3D with $x_{VG_{TE}} = 1.54$ m, and experiments without VGs.

5.2. VG position variation

Here, four chosen streamwise positions for the VG model position, corresponding to the VG trailing edges, are presented: $x_{VG_{mod}} = 1.25, 1.40, 1.54,$ and 1.80 m, giving approximately equidistant streamwise distances for the first three positions. The last position is very close to the separation region in order to investigate the influence there. Also included in the figures are spanwise averaged results from VG3D with $x_{VG_{TE}} = 1.54$ m and experimental results without separation control for the wall pressure plots.

Figure 9 presents the wall pressure coefficient distributions along the flat plate. Here, the tendency of a higher pressure increase in the APG region as well as a lower total pressure loss at the outlet are clearly visible the more upstream the VG model is placed, resulting from higher streamwise velocities around the VG model. Therefore, stronger vortices are generated that in turn have a stronger effect on the flow. Further downstream at $x_{VG_{mod}} = 1.80$ m, the wall pressure and the skin friction coefficient distribution in figures 9 and 10 are more similar to the FP2D case, compare with previous Figures 7 and 8. Here, the separation bubble is still present because the boundary layer is already so much decelerated at $x_{VG_{mod}} = 1.80$ m that only very weak vortices evolve from this streamwise position, having no effect on separation prevention or delay. The efficiency of the applied separation control devices changes depending on the actual VG model position, giving lower total pressure losses the

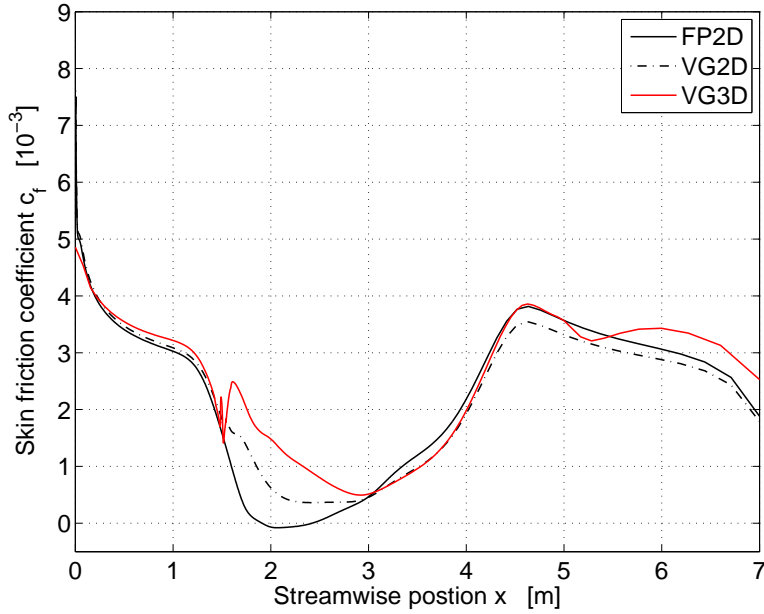


FIGURE 8. Local skin friction coefficient distributions for FP2D, VG2D, and VG3D with $x_{VGTE} = 1.54$ m.

more upstream the VG model is placed, i.e. within a smaller boundary layer thickness. The trend that a large distance of the VG model to a separation region has advantages for separation control is only valid in the range of positions studied here. Further upstream generated vortices encounter sooner breakdown or strong diffusion that weakens the positive influence on the mean flow before they actually reach the separated region. This will be further investigated and presented in Ch. 5.3.

The skin friction coefficient results in Fig. 10 show again how the VG model position affects the flow and the separation region. The effect of the VG model far upstream results in a distinct peak of the skin friction coefficient, similar to the VG3D peak around the resolved VG TE. The local flow is generally enhanced for all VG model locations except for $x_{VGmod} = 1.80$ m, for the same reasons as mentioned above. In the FPG section and the following ZPG region, all favorable VG model computations more or less collapse, describing similar flow fields downstream of the APG region. Again, it is not sure if a further increase of the distance between the VG model plane and the separation region leads to even better results in the region of interest. On the other hand, it is important to recall that higher velocities around the VG model also induce higher parasitic drag to the mean flow. This is a trade-off situation and needs to be considered when this VG model is used within engineering applications.

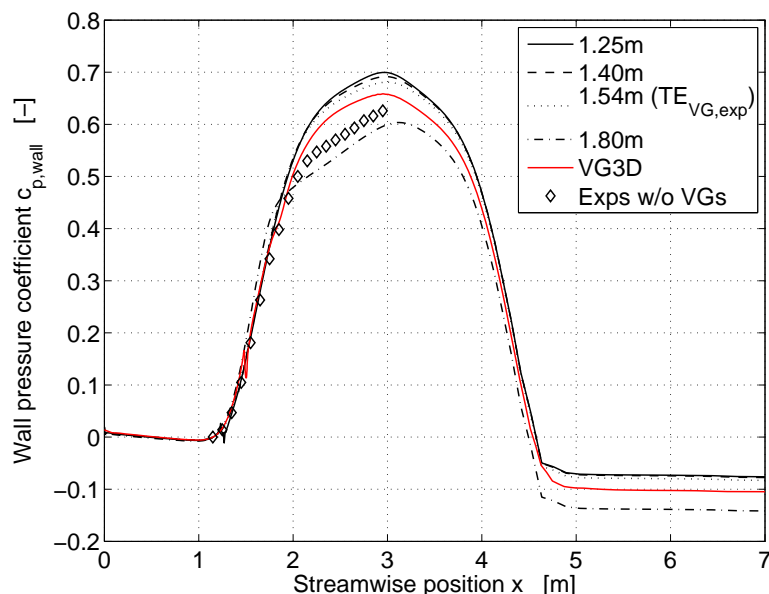


FIGURE 9. Wall pressure coefficient distributions for VG model streamwise position variation, VG3D with $x_{VG,TE} = 1.54$ m, and experiments without VGs.

Another interesting flow feature to evaluate are the velocity profiles for the controlled case at the streamwise position where the separation bubble is thickest for the uncontrolled case. This streamwise position was located to be at $x_{sep,max} = 2.25$ m, giving a separation bubble height of $h_{sep,max} = 26$ mm. Lögdberg *et al.* (2009) results showed to give a separation bubble height of $h_{sep,max} = 17$ mm at $x_{sep,max} = 2.55$ m, see also Table 2. It is mentioned again that this specific flow case was difficult to set up with its fully correct boundary conditions in order to create experimental conditions in detail. The authors are therefore satisfied with these results, being close to experimental data. Figure 11 shows the velocity profiles for the different VG2D, and for the VG3D computations. The latter case provided two additional velocity profiles at an inflow and an outflow position in the spanwise direction. These two positions correspond to the inflow and outflow position as in Lögdberg *et al.* (2009), the inflow position being defined as the mid-position between two VG pair blades in counter-rotating set-ups. Likewise, the outflow position is therefore defined as the mid-position between two VG pairs.

In Fig. 11, it can be observed that the four VG2D cases show conforming trends for all mean velocity profiles. The further downstream the VG model is applied, the smaller are the streamwise velocities close to the wall, indicating less momentum mixing in the boundary layer. The VG model streamwise position at $x_{VG,mod} = 1.80$ m shows reversed flow, being consistent with the c_f

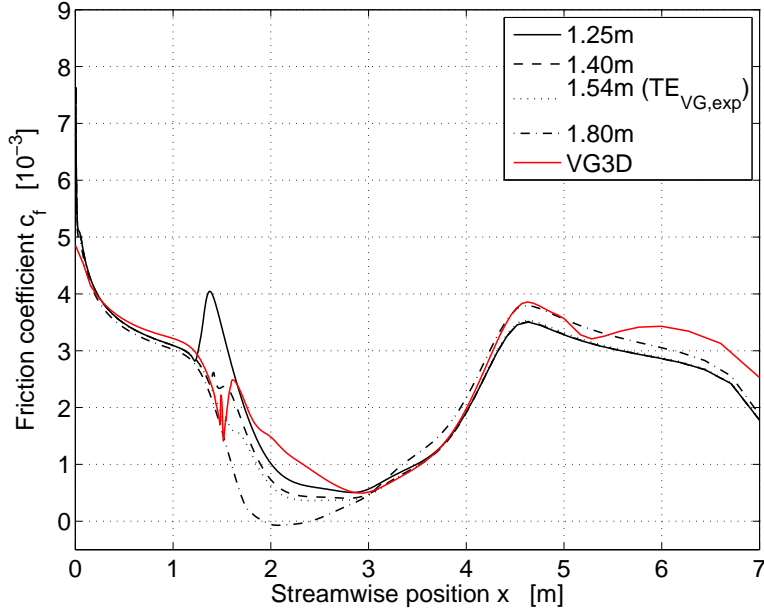


FIGURE 10. Local skin friction coefficient distributions for VG model streamwise position variation, and VG3D with $x_{VGTE} = 1.54$ m.

distribution in Fig. 10. The three plots of the VG3D computations present the results of the inflow, outflow, and the averaged velocity profiles. In general, they show the existing velocity defect from the fully resolved VGs. First, high-momentum containing fluid is pushed down to the wall at the inflow position, increasing the near-wall velocity (gray solid line). Here, it can be well-observed how the flow is accelerated close to the wall. Second, low-momentum fluid is pushed upwards at the outflow position, leading to much lower velocities near the wall (gray dashed line). The corresponding VG model velocity profile for $x_{VGmod} = 1.54$ m fits in between the VG3D velocity profiles at the inflow and outflow positions, yet lacking the velocity defect. However, the VG2D profile is not matching the spanwise averaged VG3D profile (gray dashed-dotted line), giving a lower near-wall velocity distribution and lacking the averaged velocity defect further away from the wall. Nevertheless, it can be stated that the VG2D velocity profiles show consistency with each other, confirming the previous plots of the local skin friction coefficient and the wall pressure distribution in Figs. 9 and 10. Moreover, the results of the VG3D computations show that the resolved vortex structures in the velocity results are extended much further away from the wall compared to $h_{VG} = 18$ mm. This shows what an important role the mixing effects play in the resolved case.

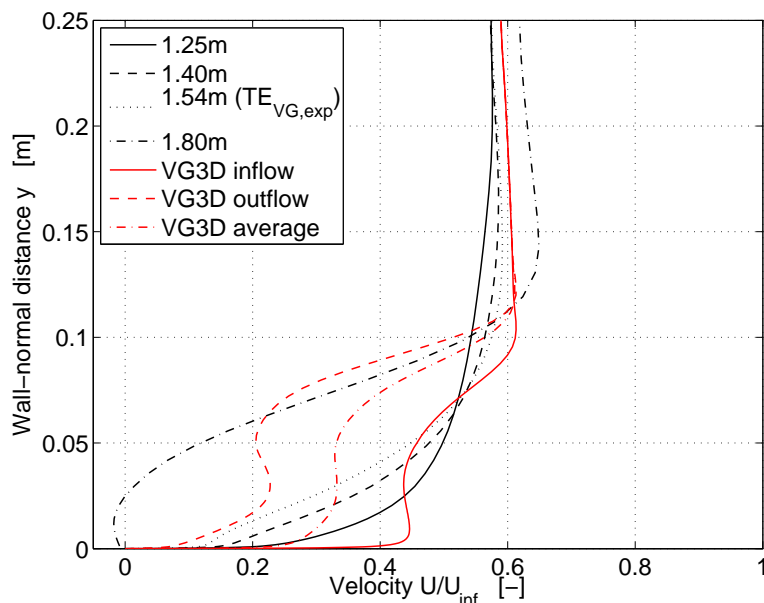


FIGURE 11. Mean velocity profiles at $x = 2.25m$ for the VG model streamwise position variation and for VG3D computations with $x_{VGTE} = 1.54$ m at inflow and outflow positions, and its corresponding averaged velocity profile.

5.3. Other VG model parameter variations

In order to investigate the sensitivity and the influence of the VG model on separation prevention for different VG model positions in the region $x \leq 1.25$ m, additional three streamwise positions upstream of the APG region were chosen: $x_{VGmod} = 0.10$ m, 0.50 m, and 0.80 m; see also Fig. 12. It can be seen that all VG model positions prevent flow separation successfully. Nevertheless, the optimum of these four cases is located at $x_{VGmod} = 1.25$ m at the beginning of the APG region. If one compares this result with Fig. 10, it can be observed that there exists a global optimal position for the VG model in the vicinity of $x = 1.25$ m. It can be stated that further upstream VG model positions lead to higher VG vane tip velocities that in turn create stronger vortices by the LLT and the vortex model. Nevertheless, the further upstream the VG model was applied, the more diffused the second-order statistics become before they reach the separation region. In that respect, the positioning of the VG model shows sensitivity in flow separation prevention efficiency. Moreover, it can be observed that any VG model position, except very close to the separation region, leads to successful flow separation prevention.

Another interesting aspect to check was the difference in efficiency between co- and counter-rotating set-ups, see Fig. 13. Four different set-ups were investigated: two counter-rotating settings, one given by a "common flow up" and another one by a "common flow down" setting. Furthermore, two co-rotating settings were examined: one with a VG pair distance¹ D as for the counter-rotating case with the same total number of VG blades, and another setting with an increased "VG pair" distance of $2D$, bisecting the total VG vane density. The result of this comparison shows that counter-rotating systems are more efficient than co-rotating systems, being consistent with previous experimental results (Godard & Stanislas 2006). The co-rotating devices, on the other hand, do not show much improvement when the VG vane density is doubled (or: VG distance decreases from $2D$ to $1D$), compare with Fig. 13. This is a consequence of the 2D vortex velocity field, resulting from the modeled VG array. Here, the velocities partly weaken/cancel out each other and this effect is higher the closer the VG vanes are located to each other.

Moreover, the VG model does not give any difference between "common flow up" and "common flow down" settings. The reason is that the spanwise averaging of the second-order statistics in the VG model description at the VG model plane position is identical for both set-ups and, thus, the current VG model cannot capture this effect. However, experiments show higher efficiency for "common flow down" set-ups since the vortices remain longer and closer near the wall, having a better and more persistent effect on flow separation prevention (Pauley & Eaton 1988).

Table 3 presents experimental and computational VG settings of case II: the circulation per unit width (Lögberg *et al.* 2009), the VG heights, the streamwise VG locations in experiments and the flow state as well as the corresponding streamwise VG model locations in computations and the flow state. The normalized distance of the flow control devices from the separation bubble $(x_{sep,max} - x_{VG})/h_{VG}$ for both the experiments and the computations was consequently the same. The circulation per unit width was defined as

$$\gamma_e \equiv 2k \frac{h_{VG} U_{VG}}{D}, \quad (6)$$

where k is a coefficient that takes the VG geometry into account, see also Angele & Muhammad-Klingmann (2005), h_{VG} the VG height, U_{VG} the VG tip velocity, and D the VG pair distance in the spanwise direction. Computations regarding the corresponding streamwise distance between the VG model position and $x_{sep,max}$ were carried out and are presented in Fig. 14. Here, it can be observed that the overall trend from table 3 is correctly predicted by the VG model: computations for the first three cases according to the legend show separation prevention, whereas a reduction in $h_{VG,mod}$ from 18 mm to 10 mm predicts separated flow as in experiments, see the last case for $\gamma_e = 1.0$. Again,

¹Co-rotating systems do not necessarily consist of VG pairs, but this term was used for reasons of consistency with Ch. 2

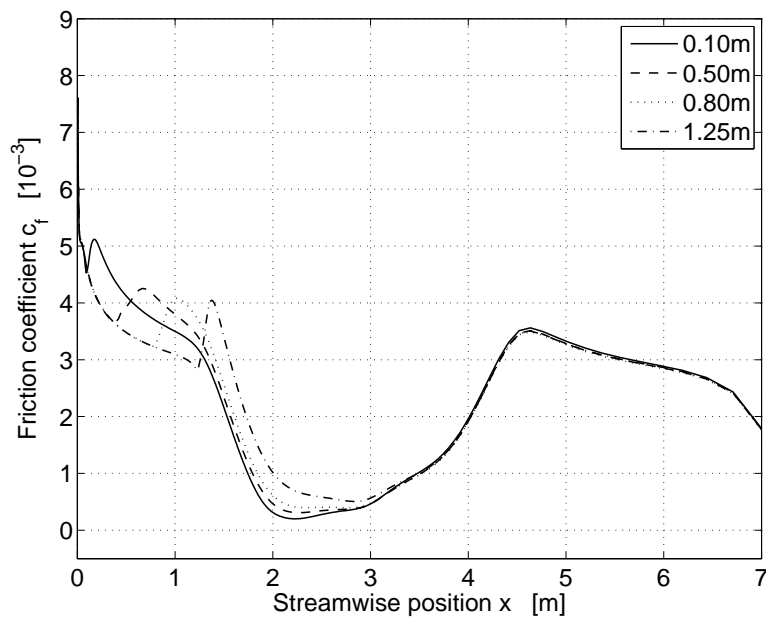


FIGURE 12. Local skin friction coefficient distributions for VG model streamwise position variation upstream of the APG region.

the application of the VG model further upstream at $x_{VG_{mod}} = 0.80$ m shows less efficiency than for $x_{VG_{mod}} = 1.30$ m, confirming the trend of Fig. 12.

TABLE 3. The VG circulation per unit width, VG heights, the VG streamwise locations $x_{VG_{exp}}$ in the APG experiments of Lögdberg *et al.* (2009) for case II, the flow states in experiments, corresponding VG streamwise locations $x_{VG_{mod}}$ for the VG model computations, and the flow states in VG model computations; (exp. $\hat{=}$ experiment, att. $\hat{=}$ attached, sep. $\hat{=}$ separated).

γ_e [m/s]	h_{VG} [mm]	$x_{VG_{exp}}$ [m]	flow, exp.	$x_{VG_{mod}}$ [m]	flow, VG model
3.8	18	1.10	att.	0.80	att.
3.1	18	1.60	att.	1.30	att.
1.4	18	2.00	att.	1.70	att.
1.0	10	2.00	sep.	1.70	sep.

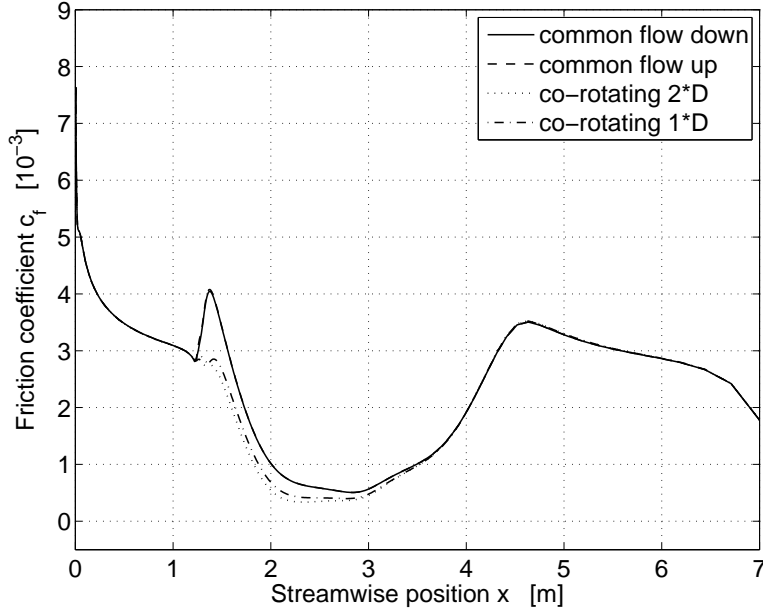


FIGURE 13. Local skin friction coefficient distributions for different VG model settings at $x_{VG_{mod}} = 1.25$ m, $\alpha = \pm 15^\circ$.

6. Conclusions

Wall pressure and skin friction coefficient distribution plots have shown that the VG2D model computations successfully describe the improvement of the flow by means of preventing the initial separation on the clean flat plate. This can be observed by comparing corresponding flat plate computations as well as experimental plots with the VG model computation plots in Figures 7 and 8. The lower total pressure losses at the outlet plane of the controlled cases in the wall pressure plots indicate how the total flow losses are decreased using controlling devices, either the VG model or resolved structures. The actual differences in the VG2D and the fully resolved VG3D computations are expected since the VG model describes the vortex structures from a 2D vortex model in a turbulent statistical way rather than resolving the 3D vortex structures as it is the case for the 3D computations. Therefore, velocity and also skin friction results are likely to be different from experiments and results from fully resolved computations. Nevertheless, it is important to point out that the goal, the overall separation prevention, has been successfully shown for the VG model.

In addition, it is important to note that the computational set-up for all three cases (FP2D, VG2D, VG3D) and, in particular, their APG boundary conditions are not exactly equivalent to experiments. Especially the experimental

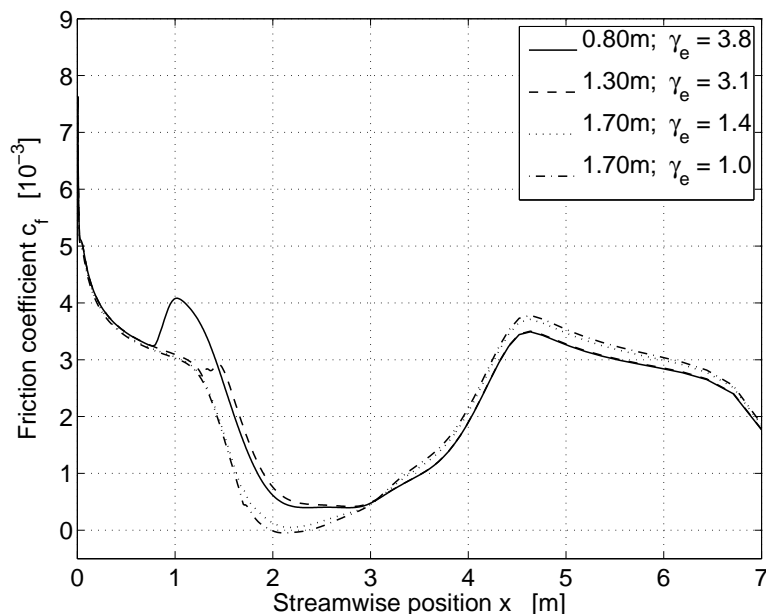


FIGURE 14. Local skin friction coefficient distributions for different VG model settings, corresponding to experimental settings; legend: left column $x_{VG,mod}$, right column γ_e according to Lögdberg's experiments (Lögdberg *et al.* 2009), see also table 3.

suction system turned out not to be practically accomplishable in a computational set-up. Nevertheless, the three computational cases are all comparable with each other since they incorporate the same boundary conditions.

The streamwise position as well as the height of the VG influences the mean flow results. In particular, this investigation focussed on wall pressure and local skin friction coefficient distributions. The differences in results of the position variations can e.g. be observed in terms of the total pressure losses at the domain outlet in Fig. 9, or by the wall skin friction distribution plots as e.g. in Fig. 10. The overall trends and tendencies from the parameter variations show that there exists an optimal streamwise position for the VG model and that it should be placed a certain distance upstream of the flow separation in order to be able to generate the required second-order turbulent statistics that have the desired separation preventative impact on the mean flow. In addition, different VG model position and height combinations as in experiments could successfully simulate the flow states quantitatively, predicting either attached and separated flow correctly. Checking for the sensitivity regarding co- and counter-rotating set-ups shows consistency with established experimental results (Godard & Stanislas 2006). Nevertheless, "common flow

down/up” settings did not show any differences unlike previously described in experiments (Pauley & Eaton 1988), originating from the limitations in the VG model approach.

This investigation has shown that the statistical VG model approach is very promising for an application in APG flow and has the advantage of not being more computationally expensive than solving RANS equations without modeled VGs, leading to much faster results than with conventional methods such as fully or partly resolved VGs.

Acknowledgments

The experiments were defined and carried out within a cooperative research program between KTH Stockholm and Scania AB, Sweden, and Dr. Ola Lögdberg is grateful acknowledged for providing the experimental data.

References

- ANGELE, K. P. 2003 Experimental studies of turbulent boundary layer separation and control. PhD thesis, Department of Mechanics, KTH Stockholm.
- ANGELE, K. P. & MUHAMMAD-KLINGMANN, B. 2005 The effect of streamwise vortices on the turbulence structure of a separating boundary layer. *European Journal of Mechanics B/Fluids* **24**, 539–554.
- BATCHELOR, G. K. 1964 Axial flow in trailing line vortices. *Journal of Fluid Mechanics* **20** (4), 645–658.
- BENDER, E. E., ANDERSON, B. H. & YAGLE, P. J. 1999 Vortex Generator Modelling for Navier-Stokes Codes. *American Society of Mechanical Engineers FEDSM* **99-6919**.
- DENGEL, P. & FERNHOLZ, H. H. 2009 An experimental investigation of an incompressible turbulent boundary layer in the vicinity of separation. *Journal of Fluid Mechanics* **212**, 615–636.
- ELIASSON, P. 2002 Edge, a navier-stokes solver for unstructured grids. *Proceedings to Finite Volumes for Complex Applications III* pp. 527–534, edited by D. Kroner and R. Herbin, Hemre Penton Science London.
- GLAUERT, H. 1926 *The Elements of Aerofoil and Airscrew Theory*, 1st edn. Cambridge University Press, London, UK.
- GODARD, G. & STANISLAS, M. 2006 Control of a decelerating boundary layer. Part 1: Optimization of passive vortex generators. *Aerospace Science and Technology* **10** (3), 181–191.
- HELLSTEN, A. 2005 New Advanced $k - \omega$ Turbulence Model for High-Lift Aerodynamics. *AIAA Journal* **43** (9), 1857–1869.
- JIRÁSEK, A. 2005 A Vortex Generator Model and its Application to Flow Control. *Journal of Aircraft* **42** (6), 1486–1491.
- LIN, J. C. 2002 Review of research on low-profile vortex generators to control boundary-layer separation. *Progress in Aerospace Sciences* **38**, 389–420.
- LINDGREN, B. & JOHANSSON, A. V. 2004 Evaluation of a new wind tunnel with expanding corners. *Experiments in Fluids* **36**, 197–203.
- LÖGDBERG, O., FRANSSON, J. H. M. & ALFREDSSON, P. H. 2009 Streamwise Evolution of Longitudinal Vortices in a Turbulent Boundary Layer. *Journal of Fluid Mechanics* **623**, 27–58.
- PAULEY, W. R. & EATON, J. K. 1988 Experimental Study of the Development of Longitudinal Vortex Pairs Embedded in a Turbulent Boundary Layer. *AIAA Journal* **26** (7), 816–823.
- PEARCEY, H. H. 1961 *Boundary Layer and Flow Control, its Principles and Applications*. Oxford, UK: Pergamon Press.
- VON STILLFRIED, F., WALLIN, S. & JOHANSSON, A. V. 2009a Statistical Modeling of the Influence of Turbulent Flow Separation Control Devices. *47th AIAA Aerospace Sciences Meeting, Orlando, FL, USA AIAA 2009-1501*.
- VON STILLFRIED, F., WALLIN, S. & JOHANSSON, A. V. 2009b A Vortex Generator Model Applied in Zero and Adverse Pressure Gradient Flow. *submitted for publication* .

- TAYLOR, H. D. 1947 The elimination of diffuser separation and its prevention by vortex generators. *United Aircraft Corporation Report R-4012-3*.
- TÖRNBLOM, O. & JOHANSSON, A. V. 2007 A Reynolds stress closure description of separation control with vortex generators in a plane asymmetric diffuser. *Physics of Fluids* **19**.
- VELTE, C. M., HANSEN, M. O. L. & OKULOV, V. L. 2009 Helical structure of longitudinal vortices embedded in turbulent wall-bounded flow. *Journal of Fluid Mechanics* **619**, 167 – 177.
- WALLIN, S. 2000 Engineering Turbulence Modelling for CFD With a Focus on Explicit Algebraic Reynolds Stress Models. PhD thesis, Department of Mechanics, KTH Stockholm.
- WALLIN, S. & JOHANSSON, A. V. 2002 Modelling streamline curvature effects in explicit algebraic Reynolds stress turbulence models. *International Journal of Heat and Fluid Flow* **23** (5), 721–730.